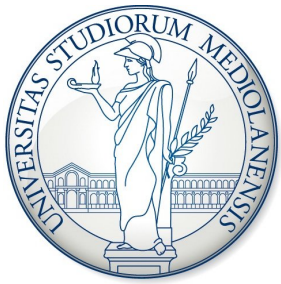

Università degli Studi di Milano
Department of Physics
Physics, Astrophysics and Applied Physics PhD School
Cicle XVIII

Relativistic Coulomb excitation of neutron rich Fe and Ni isotopes

Academic scientific discipline :FIS/04

Author: Riccardo Avigo

Coordinator: Prof. Marco Bersanelli
Supervisors: Prof. Franco Camera
Co-Supervirsor: Dr. Oliver Wieland

Academic year 2015-2016

Commission of the final examination

Prof. Franco Camera
Prof. Zsolt Podolyack
Prof. Nasser Kalantar

Final examination

28/01/2016
Università degli Studi di Milano, Dipartimento di Fisica - Milano - Italy

Università degli Studi di Milano
Dipartimento di Fisica
Corso di Dottorato in Fisica, Astrofisica e Fisica Applicata
Ciclo XXVIII
Coordinator: Prof. Marco Bersanelli

MIUR subject: FIS/04 - FISICA NUCLEARE E SUBNUCLEARE

PACS: 25.70.Hi, 29.30.Kv, 21.10.Re

D/2015/10.705/3
ISBN 978-90-8649-793-5

Dissertation presented in partial
fulfilment of the requirements
for the degree of Doctor in Science.

Alla mia famiglia

To my family

Quando qualcuno ti chiede se sei un dio,

tu devi dire: si!

Ray, Ghostbusters by Ivan Reitman

Contents

Introduction

This work discusses the measurement of E1 strength around one particle separation energy in the exotic neutron rich Iron and Nickel isotopes using the relativistic coulomb excitation.
The AGATA segmented HPGe detector array, DALI2 and HECTOR$^+$ large volume scintillator detectors have been employed for this search.
Relativistic coulomb excitation is a well established experimental technique to investigate the properties of nuclear structure: in particular it is very useful to characterize the electric dipole response in exotic nuclei far from the stability, as it excitates mainly the E1 isovector mode.
The electric dipole response of atomic nuclei, in fact, is presently attracting large attention from the nuclear physics research community. In particular the E1 strength in neutron rich nuclei, located at around one particle separation energy (6-12 MeV energy range) is the object of a large experimental and theoretical effort [9]. In this energy region structures and accumulations of the E1 strength were measured in a variety of nuclei along all the valley of stability. These structures, commonly called Pygmy Dipole Resonance (PDR) as they lie at energies below the Giant Dipole Resonance and have smaller strength, are at the centre of the scientific debate as the strength is connected to the neutron skin thickness and the symmetry energy term of the nuclear equation of state [1], [2]. In addition, it was shown in literature that PDR, and the nuclear structure features connected with it, are relevant for astrophysics, in particular concerning neutron star structure and reactions in extreme condition scenarios [3]. The symmetry energy term of the equation of state is connected with the pressure of infinite nuclear matter, this means

that an evaluation of this parameter could provide informations on the maximum pressure sustainable by neutron stars, and therefore on their maximum dimensions. On the other hand an accumulation of strength at one particle separation energy could change the n-γ reaction ratio in exotic environments, like supernovae, changing the production rate of heavy nuclei.

These connections with many nuclear and astrophysics aspects, made the investigation of the E1 response of nuclei an important aspect of the recent nuclear physics research. In spite of the large amount of data about E1 strength distribution in stable nuclei, very few data are available for neutron rich exotic nuclei far from the stability. Two experimental campaigns to search for the pygmy dipole resonance in ^{64,62}Fe and ^{70}Ni nuclei were recently performed. The Iron isotope investigation was performed in GSI in 2012 and concluded in 2014, during the PreSPEC – AGATA experimental campaing [4], while ^{70}Ni E1 response was measured at the RIKEN/RIBF laboratory during the DALI2 campaign in autumn 2014 [5].

The response of nuclei was investigated through relativistic Coulomb excitation in inverse kinematics. This reaction mechanism coupled with the detection of the gamma rays emitted by the excitated nuclei is a well established experimental technique to investigate nuclear properties in the energy region of PDR in nuclei far from the stability [6]. The advantage of this experimental technique relies on the predominancy of the E1 excitation at this beam velocity. Neutron rich isotopes are expected to be characterized by an enhancement of these PDR structures because of a more unbalanced neutron over proton number ratio. There are more delocalized neutrons that in principle increase the neutron skin thickness. The measurement of this strength is therefore an important test bench for the theories developed to explain these structures.

In this PhD thesis, the first chapter will introduce the Giant and Pygmy Dipole Resonance modes. An overview of coulomb excitation reaction mechanism will be presented in Chapter 2. Chapter 3 will describe the experimental setup used for the measurements discussed in this thesis, while Chapter 4 and 5 will present and discuss the data analysis and the results obtained.

CHAPTER 1

Nuclear response to E1 excitations

In this chapter a brief overview of the nuclear response to E1 excitation above and around the one particle separation energy, will be presented. In the first part nuclear giant resonances, that lie at energies around 15 MeV, will be described, while in the second one we will focus on the response of the nucleus around the one nucleon separation energy. In particular this response, that is the subject of this PhD thesis, can be interpreted as a nuclear resonance, called Pygmy Dipole Resonance (PDR). A lot of aspects of this response need a theoretical interpretation and experimental investigation.

1.1 E1 strength distribution in nuclei

The study of the atomic nucleus has shown in the last decades the complexity of this many body quantum system. A lot of theoretical models have been developed to describe nuclear structure and its changes in a variatey of conditions: the nuclei show both collective and single particle features. Experiments with different probes are needed to investigate the many aspects of nuclear system. Electromagnetic interaction is a well known probe for nuclear features investigation thanks to the analytical description of electromagnetic field. As regarding dipole probes, nuclei show strength accumulations and structures from few keVs to tens of MeV(as represented in Fig. 1.1).

In this chapter we will focus on the E1 strength function; two structures lie clearly at high energy: the Giant Dipole Resonance (around 15 MeV) and the Pygmy Dipole Resonance (around one nucleon separation energy). The first one is characterized by a large amount of E1 strength (almost 100% of the EWSR), while the second one represents just few percentage of the sum rule (that is the reason of its name). Both the structures are

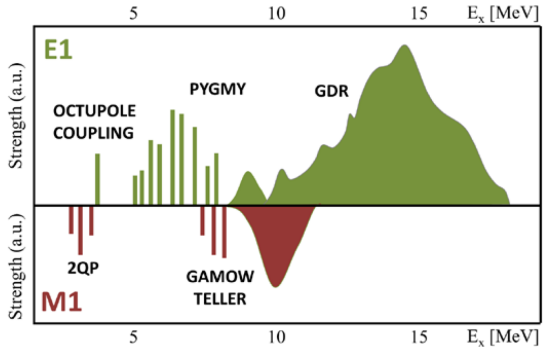

Figure 1.1: Dipole Strength distribution in the atomic nucleus. In the upper part E1 strength is displayed while the M1 diustribution is showed lower [8]

related to significant features of nuclear structure and in the two next sections they will be described in more detail. GDR description will be based on the discussion of Ref. [7], while PDR mainly based on the overview of Ref. [9].

1.2 Isovector Giant Dipole Resonance

Giant Resonances are collective vibrational states above the separation energy, interpreted as an harmonic vibration of the density or the shape around the equilibrium of the nuclear system. The oscillation is defined by a small amplitude (few per cent of nuclear radius), high frequency (around 10^{21} Hz) and a strong damping (reflected in the large width of the Lorentzian associated to this vibration mode). Eq. 1.1 represnts the formula for the GDR Lorentian:

$$\sigma(E) = \frac{\sigma_m \Gamma_m^2 E^2}{(E^2 - E_m^2)^2 + \Gamma_m^2 E^2} \tag{1.1}$$

where σ_m is the peak cross section, E_m the resonance enrgy and Γ_m the width that is tipically in the range of 2.5 - 5 MeV. Giant resonances are classified according to the multipolarity: in the case of E1 excitation we are interested in an Isovector Giant Dipole Resonance (IVGDR), characterized by $\Delta L = 1$, $\Delta T = 1$ and $\Delta S = 0$. This vibration is pictorially described in a hydrodynamical picture as an oscillation of protons in opposition of phase respect to the neutrons. The excitation can be induced by fusion reactions, charge exchange reactions, real or virtual photons. The electric field perturbates the system interacting essentially with protons, while the nuclear interaction between neutrons and protons represents the restoring force: the combined action of these two forces induces the vibration. The different Giant Resonances were investigated with different

probes: this allowed to study separately each resonance. The typical Lorentzian shape in energy spectra is characterized by wide distribution (fig. 1.2) and as a consequence the Lorentians of different Giant Resonances overlap: considerations on reaction mechanism and decay are needed to avoid contributions in the same spectrum from different types of Resonance.
IVGDR was extensively studied since 1937: its features and beahviour in different initial conditions were investigated. Typical experimental tools were photo-absorption reactions or measurement of Compound Nucleus decay. Also heavy ion fusion reaction with Q value sufficiently large have been used. The former allowed to scan all the lorentian distribution, thanks to the possibility to use specific target and produce γ ray beams at different energies via Bremsstrahlung technique, the latter allowed to populate GDRs built on excited states and investigate their decay.

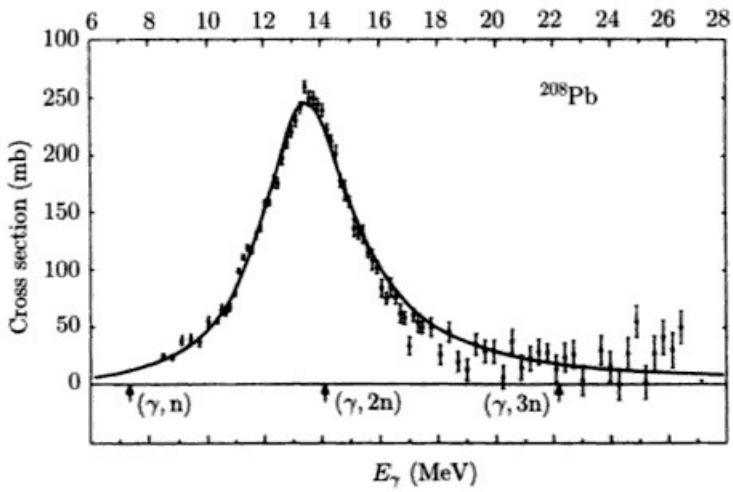

Figure 1.2: Photoneutron cross section as a function of the energy of the excitating γs for ^{208}Pb [26]

1.2.1 Microscopic Overview

Giant Dipole Resonances, as the other Giant Resonances of nuclei, can be described as a coherent superposition of particle-hole excitations induced by a one-body operator acting on the ground state (eq. 1.2) or on an excitated state.

$$|\Psi_{GR}^{\lambda,\sigma,\tau}>= O^{\lambda,\sigma,\tau}|\Psi_{g.s.}> \tag{1.2}$$

where λ,σ,τ represent the multipolarity, the spin and isospin of the resonance.
In shell model picture of the Giant Resonances, the residual particle-hole interaction gen-

erates a collective state formed by the coherent superposition of all particle-hole states with a certain multipolarity. Thanks to the fact that the residual particle-hole interaction is attractive in case of isoscalar excitation and repulsive for isovector, the isoscalar resonances lie at lower energies than the isovector ones. Giant Dipole Resonances were observed in both light and heavy nuclei: in light nuclei some fragmentations occur in the lorentzian shape, while in heavy nuclei the shape is more smooth. In case of deformed nuclei the strength is splitted and this phenomenon is interpreted as the different energy in the oscillation along the long axis (lower energy) and along short axis (higher energy). The excitation energy of GDR can be reproduced by the expression:

$$E_{exc} = 31.2A^{-1/3} + 20.6A^{-1/6}MeV \tag{1.3}$$

while the strength, expressed in terms of Thomas-Reiche-Kuhn (TRK) sum rule, can be obtained by:

$$\int_{E_{min}}^{E_{max}} \sigma_{\gamma}^{abs} dE = \frac{60NZ}{A}(1+k)MeVmb \tag{1.4}$$

where k is a factor related to meson- exchange contribution and is a characteristic of isovector resonances. In cases of nuclei with $A > 100$, in the energy range from the neutron separation energy till 25 MeV, the values of k vary from 0.1 to 0.2. Nevertheless this correction factor can change significantly and it is dependant from nuclear interaction parametyrization used for the calculations.

1.2.2 Decay Mechanism

As mentioned before, Giant Dipole Resonances are strongly damped; this is reflected in the large resonance width (with FWHM in the range of 2.5 - 8 MeV). Giant Resonance damping and decay is explained by different mechanisms, each of them conributes, to the width.

Giant Dipole Resonance can be represented as a coherent superposition of 1p-1h excitation. A small contribution to the damping is due to a spreading of the strength of this coherent 1p-1h combination on non-collective 1p-1h states. This damping does not affect intensively the decay of GDRs in heavy ions but in light nuclei it can cause a substantial splitting. The most important contribution to damping is the coupling of this 1p-1h excitation to more complex configurations (2h -2p excitations ...): the energy is spread over all the degrees of freedom of the system and a compound nucleus is formed. This damping way is usually denoted with $\Gamma^{\downarrow}$ (spreading width) and its contribution is the most relevant to the total width.

In addition, as explained in [7], a phenomenological presciption was found for this damping:

$$\Gamma^{\downarrow} = (0.026 \pm 0.005)E^{1.9\pm0.1}MeV \tag{1.5}$$

Another damping mechanism is related to the fact that the 1p-1h coherent state is well above the particle thresold. Therefore a significant contribution to the decay might be due to a particle emission (depicted by $\Gamma^{\uparrow}$ and referred to as escape width). Also gamma decay plays a role in the damping even if it has a little influence because the particle emission is favoured ($\frac{\Gamma^{\gamma}}{\Gamma} \approx 10^{-4}$). It is important to underline that also the compound nucleus produced by the combination of 1p-1h state with more complex states, can decay by particle emission. The contribution to the GDR width of the combination of these two processes is usually represented with $\Gamma^{\uparrow\downarrow}$.
The described damping and the fact that GDRs usually lie upper than the one particle separation energy, show that the main decay process consists in particle emission, in particular neutron emission. For this reason, E1 strength distribution in this energy region is studied via photoabsorption and neutron emission reaction. The relation

$$\sigma(\gamma) = \sum_{x} \sigma(\gamma, xn) \tag{1.6}$$

exhausts all the photoabsorption cross section with good approximation.

1.3 Pygmy Dipole Resonance

The E1 strength distribution of atomic nuclei is almost completely exhausted by Giant Dipole Resonance (as shown in Fig. 1.1). A small fraction of this strength is locate around one particle separation energy and it is called Pygmy Dipole Resonance. These states have shown a double nature. Experimental investigation (as in [31]) pointed out that they can be excitated with both isoscalar and isovector probes.
In the last decades the strength accumulation, here discussed, attracted the interest of the scientific community, not only for the implications in nuclear structure, but also for the important correlations in other fields. In neutron rich nuclei it was shown that this amount of strength is proportional to the "neutron skin thickness" [22], [2]. Nuclei with N>>Z show a core with an equal number of neutrons and protons while the neutrons in excess form an external shell (called neutron skin). It was proved that a correlation between the strength of the PDR and the depth of this netron crust [3]. This thickness was estimated as the difference between the radius of neutron density function and the radius of the proton one. As shown in (Fig. 1.3) the Pygmy Dipole Resonance is described as an

oscillation of this neutron skin against the core. This interpretation is still under debate, also Toroidal modes are considered in literature to explain the lower energy states [32]. In addition the level of collectivity of this state is not fixed yet, for this reason many articles refer to this state as Pygmy Dipole Strength. On the other hand it was uderlined that these states are also connected with the simmetry energy term in nuclear Equation Of State (EOS) [2]. The strength is proprtional to the slope of simmetry energy term evaluated at saturation density. This parameter is strictly connected with the thickness of the neutron skin, the compressibility of the nuclear matter and the pressure of pure neutron matter. Dependances from these nuclear features were shown also in the dipole polarizability [25]

$$\alpha_D = \frac{\hbar c}{2\pi^2 e^2} \int \frac{\sigma_\gamma}{\omega^2} d\omega \tag{1.7}$$

where σ_γ is the photo-absorption cross section.
The estimation of this quantity is based on the measurement of E1 strength distribution of the nucleus. Even if the relation with the nuclear structure properties is not as strict as in PDR case, this method does not require a disentanglement of PDR strength from GDR tail.
The nuclear structure aspects, here discussed, are also relevant in neutron star models; they influence the dimension extimations and, as a consequence, the radius of neutron stars. In particular the pressure of pure neutron matter plays a key role in this extimation because it supports neutron stars against gravitational collapse [3]. Another astrophysical aspect connected with this strength at one particle separation energy is the isotope aboundance in stars. In fact it was shown that the aboundances of heavy nuclei in the stars is higher than expected [23]. One of the aspects that could explain this disagreement is related to the fact that the presence of this strength in nuclei could change the n-γ, γ-n reaction rate in extreme astrophysics environments like supernovae. This phenomenon could have the consequence to change the rate of the photon break down of heavy nuclei and the effect would be an enhancement of heavy isotopes [24].

1.3.1 Theoretical description

In spite of the fact that the first experimental evidences of an enhanchement of gamma ray strength around 5-7 MeV were obtained in early 60s [10], the first theoretical model was proposed in 1971 by R. Mohan, M. Danos and L.C. Biedernhan [11]. It consisted in a qualitative three-fluid hydrodinamical description of the interaction between neutrons and protons in neutron rich nuclei, showing two dipole modes: the Giant Dipole Reso-

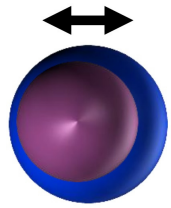

Figure 1.3: Pictorial description of the PDR macroscopic interpratation. In neutron rich nuclei, neutron in excess form a skin around a core with N=Z. PDR is interpreted as the oscillation of this skin (the blue shadow) against the core (purple sphere).

nance and another one at lower energy and two orders of magnitude weaker.
This delay in theoretical description shows how the microscopic model calculations for low-lying E1 strength are still a challenging task. While IVGDR, the gross feature of the E1 response, is described consistently in many models, the low energy structure differs more drastically between different calculations, showing a dependence on the properties of the nuclear force not fully fixed yet.
In recent years different approaches were explored: Hartree–Fock and Hartree–Fock–Bogoliubov plus (quasi-particle) Random Phase Approximations (Q)RPA based on a variety of interactions [2], second RPA calculations [12], the quasi-particle phonon model (QPM) including complex configuration [13], the extended theory of finite Fermi systems (ETFFS) [14], the Landau–Vlasov equations [15], the relativistic RPA or QRPA [16], the relativistic quasi-particle time-blocking approximation [30], and the algebraic Interacting Boson Model [18]. In almost all these calculations the low lying E1 strength was observed but the degree of collectivity is still under debate. Moreover even if different modes were discussed, many of these models show that this strength is a signature of a neutron-skin oscillation. Also the theoretical dependence of the magnitude of the strength by the asymmetry parameter α=(N-Z)/A was reproduced by both experimental data [1] and theoretical calculations (as shown in Fig. 1.4).
Approaches based on covariant energy density functionals were proved to be succesful tools for investigating low-lying E1 strength, in particular the fully self-consistent relativistic quasiparticle random-phase approximation (RQRPA) [19] (as shown in Fig. 1.5). This approach was supplemented with the coupling to low lying vibrations within the relativistic quasiparticle time blocking approximation (RQTBA) in a fully consistent way that enables to reproduce the fragmentation of the giant dipole resonance as well as of the PDR and to describe the dipole strength of the low-energy part of the spectrum. The

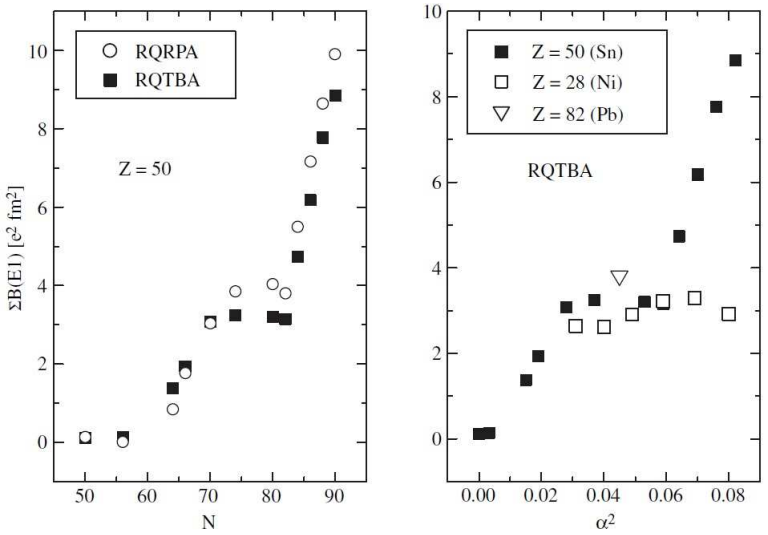

Figure 1.4: Left panel: PDR strength in the Sn isotopic chain as a function of the neutrons number. The two data set are obtained with RQRPA and RQTBA approaches. Right panel: PDR strength in the Sn,Ni and Pb isotopes as a function of the squared asymmetry parameter α [20].

main improvement of this last approach is the reproduction of the fragmentation of the strength of the few low-lying states in the RQRPA. The fact that this higher density was obtained with the coupling to complex configurations, seems to be a step towards a more realistic description of the E1 response of the nuclei in this energy region.

1.3.2 Experimental investigation

The interest of scientific community in this subject and the double nature (isoscalar and isovector) of these states has motivated the experimental investigation with different probes and experimental techniques. Indeed after forty years of experiments an exahustive description of the pygmy dipole states is not avaible yet. A brief resume of the effort to measure the features of these states is presented here.

The first method applied to investigate PDR in stable nuclei was Nuclear Resonance Fluorescence (NRF). In particular (γ,γ') reactions provided a lot of data on stable nuclei in the energy region below the binding energy. The high selectivity to dipole-states, the well known excitation mechanism and the possibility to use HPGe detector in measuring de-excitation gamma rays allow to obtain high precise measurements of both energy and strength for dipole states below one particle separation energy.

As introduced in previous section, the interesting energy region for PDR extends also

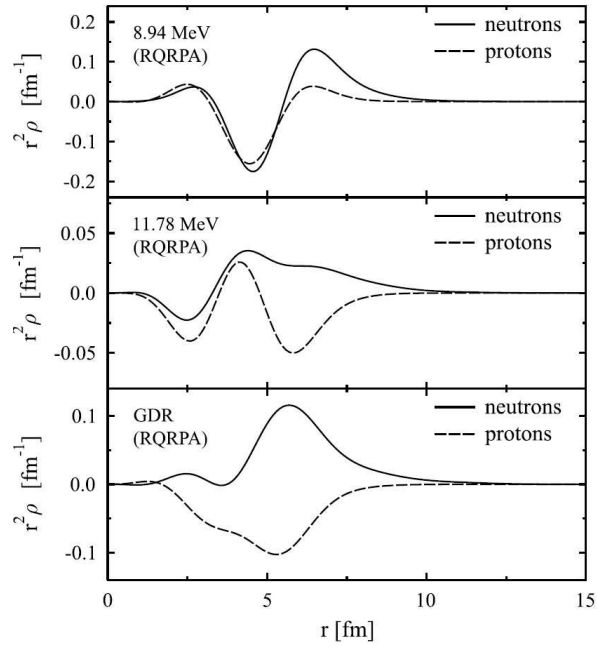

Figure 1.5: Proton and neutron transition densities for two pronounced peaks at low excitation energy (8.94 MeV and 11.78 MeV) for ^{116}Sn. In the last panel GDR transition densities as comparison. All the transition densities plotted were obtained with RQRPA approach [20], [21].

above the binding energy. In order to investigate also this energy range, photo-dissociation experiments were performed. The critical point was the fact that neutrons emitted in (γ,n) reactions do not have all the energy of the state because daughter nuclei have often low energy excited states. The introduction of Bremsstrahlung technique for gamma ray production allowed to investigate PDR in a large excitation energy region thanks to the continuous spectrum of gamma rays colliding on target. These two technique provided a lot of informations about nuclei along all the valley of stability. Also other techniques with real photons were applied, as tagged photons and laser Compton backscattering.

The limit of these approaches is represented by the fact that only PDR in stable nuclei can be investigated; in addition just the isovector character is observed while they cannot provide any information on isoscalar aspects accessible only with nuclear probes.

Coulomb excitation provided a technique to have the access also to exotic nuclei. The possibility to excitate heavy-medium nuclei by virtual photon is connected with high resolution ion tracking: it is essential to recontruct ion tracks to select pure coulomb interaction events. In addition even if at relativistic energies dipole excitation dominates

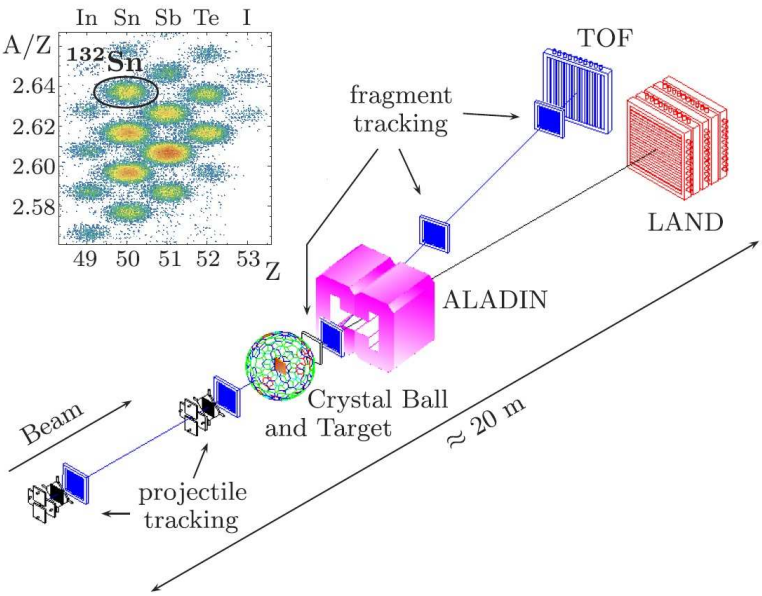

Figure 1.6: Schematic view of LAND setup. Sn radioactive isotope beam is investigate via virtual photon break-up. Crystal Ball array allow γ detection; ALADIN magnet separates reaction products, charge particles and neutrons; LAND array counts decay neutrons emitted [27].

on other multipolarities, for highly precise measurements these contributions has to be considered. For this reason highly precise particle detectors are needed to measure energy and momentum of reaction products. It is necessary to use gamma ray detector systems that cover an angular range sufficiently wide to fix the multipolarity of gamma rays emitted in the de-excitation. The key point of this technique is that it can be applied also in inverse kinematics: this implies that exotic nuclei with short lifetime can be investigated, thanks to the accessibility of radioactictive ion beams. Similar method is used in investigating exotic nuclei with virtual photon break-up technique (Fig.1.6). A radioactive beam is brought to collide with a high Z value target to induce the break up via coulomb excitation. Then all the γ rays, emitted neutrons and fragments are detected to reconstruct the excitation energy of the incident exotic ions. The investigation of PDR is based on the measurement of neutrons emitted. Due to scarce neutron detection efficiency of neutron counters and threshold effects at one particle separation energy, this measurements requires accurate simulation of the experimental setup.

The double nature of PDR (isoscalar and isovector) requires an investigation not only with electromagnetic probes, that are sensitive to isovector character, but also hadronic interactions [31]. Typical experimenthal techniques consist in inelastic scattering with α

particles at some tens MeV/u. An awkward aspect of isoscalar interaction is the low selectivity in multipolarity. For this reason it is important to measure not only α scattered particles but also the γ decay. An experimental setup able to provide both these measurements allows to select dipole excitation, reducing the contamination from higher multipolarities.

1.4 Low Energy E1 response in Iron and Nickel isotopes

As explained in the previous section, the low energy E1 response of nuclei is actually object of experimental and theoretical investigations. Pygmy states, as GDR states, show splitting in tiny substructers around one particle separation energy. In this thesis these substructures will be investigated in ^{62,64}Fe and ^{70}Ni. It is important to underline that this investigation has not yet been performed in nuclei far from the stability with high energy resolution. Indeed the B(E1) values of the states next to one particle separation energy were already measured for stable neutron rich isotopes as shown in fig.1.7. The

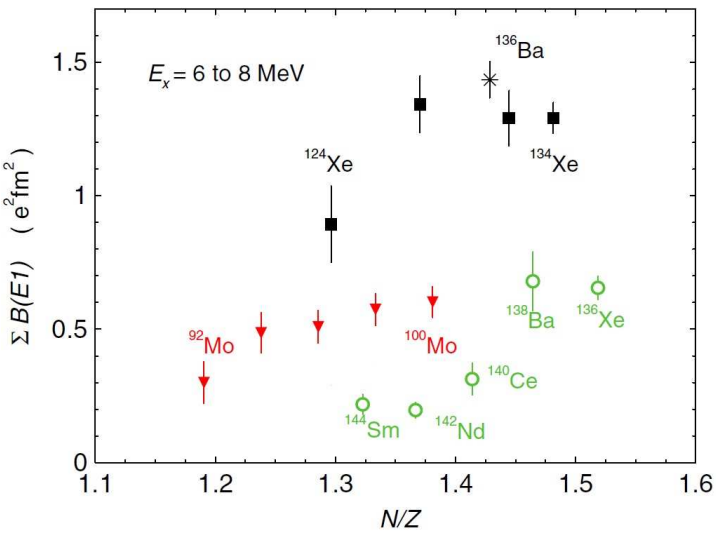

Figure 1.7: Summed B(E1) values versus neutron to proton ratio [28].

mass region considered in the measurements discussed in this thesis was chosen to be around ^{68}Ni: this nucleus was already studied both on the theoretical and experimental point of view. In particular the Pygmy Strength was measured by Milano group with the relativistic coulomb excitation [6], and also by LAND group with the photon break up technique [29]. The measurements here discussed will provide information on the

evolution of the low energy tail of this dipole strength at varying of proton and neutron numbers in an exotic mass region, going from an even-even spherical nucleus to a more deformed (^{62,64}Fe) nuclei and, in the case of ^{70}Ni, adding two neutrons. Theoretical calculations performed with Relativistic Quasiparticle Random Phase Approximation (RQRPA), Relativistic Quasiparticle Time Blocking Approximation (RQTBA) and a Relativistic Quasiparticle Time Blocking Approximation version with 2q⊗phonon (RQTBA-2) are shown in fig. 1.8 . It is possible to see how the distribution of these states change

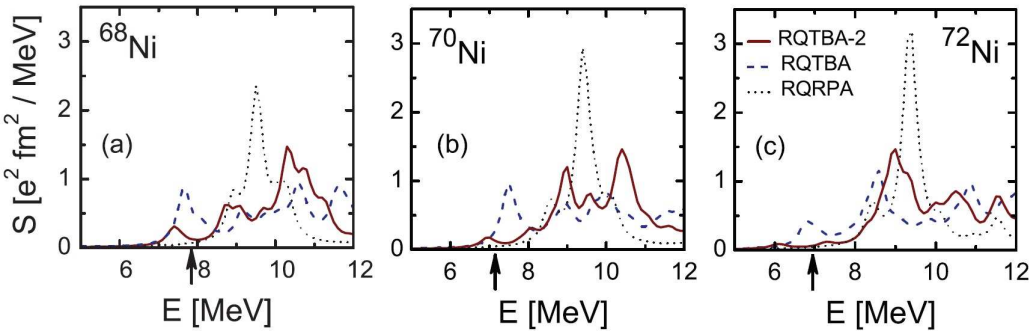

Figure 1.8: Low energy dipole spectrum of ^{68,70,72}Ni calculated with the RQRPA (black dotted lines), RQTBA (blue dashed lines), and RQTBA-2 (red solid lines) with a smearing parameter of 200 keV. The arrows indicate the neutron thresholds [30].

with the neutron number. Calculations using RPA approach were performed also for the Iron isotopes (fig.1.9). In this case it is possible to see clearly the increase of pygmy strength as the neutron number increases.

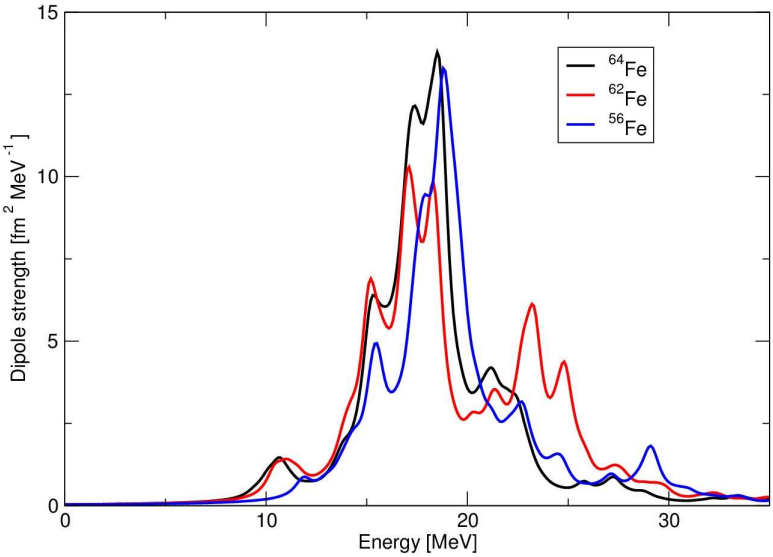

Figure 1.9: Energy dipole spectrum of ^{56,62,64}Fe calculated with the RPA approach (for courtesy of prof. Roca Maza).

CHAPTER 2

Relativistic Coulomb excitation

The pygmy dipole strength investigation, described in this thesis, was performed with the well established relativistic coulomb excitation technique. Coulomb excitation is a reaction of inelastic scattering between two nuclei in which part of the kinetik energy is transferred from one to the other through their electromagnetic field. The good knowledge of the electromagnetic interaction, the possibility to obtain the reduced probabilities and the multipolarity for the nuclear transitions makes this reaction mechanism one of the most used to investigate the nuclear structure. In this chapter a brief theoretical review (based on the review by Bertulani [33]) of this experimental technique will be presented, focusing on the particular conditions in which the experiments here discussed took place.

2.1 Coulomb excitation

In Coulomb excitation reactions the nuclei are excitated through the exchange of virtual photons between the projectile and target. The electrostatic potential of a system of point-like charges can be written as:

$$V(\mathbf{r}) = \sum_i \frac{e_i}{|\mathbf{r} - \mathbf{r}_i|} \tag{2.1}$$

This potential can be rewritten using the multipole expansion:

$$V(\mathbf{r}) = \sum_{LM} \frac{4\pi}{2L+1} \frac{1}{r^{L+1}} Y^*_{LM}(\mathbf{n}) \boldsymbol{M}(EL, M) \tag{2.2}$$

where $\mathbf{n}$ is the direction of vector $\mathbf{r}$ and $\boldsymbol{M}(EL, M)$ is the electric multipole moment. If we consider a charge distribution instead of a system of point-like charges, the electric

multipole moment can be expressed using the charge density operator:

$$\boldsymbol{M}(EL,M) = \int d^3r\rho(\mathbf{r})r^L Y_{LM}(\mathbf{n}) \text{ with } \mathbf{n} = \frac{\mathbf{r}}{r} \tag{2.3}$$

For a radiative transition in a nucleus $i \to f$, where i indicates the initial and f the final state, it is possible to define the reduced transition probability as:

$$B(EL; i \to f) = \sum_{MM_f} \left| \left(\boldsymbol{M}(EL,M)\right)_{fi} \right|^2 \tag{2.4}$$

or, using the reduced matrix element:

$$B(EL; i \to f) = \frac{1}{2J_i+1} \left| \langle f \left\| \boldsymbol{M}(EL,M) \right\| i \rangle \right|^2 \tag{2.5}$$

This relation has the advantage of being independent by the projections on M_i. The same quantity can be easily obtained for the inverse transition:

$$B(EL; f \to i) = \frac{2J_i+1}{2J_f+1} B(EL; i \to f) \tag{2.6}$$

For example in the case represented in fig. 2.1, the equation 2.6 becomes:

$$B(E2; f \to i) = \frac{2\cdot 0+1}{2\cdot 2+1} B(E2; i \to f) \tag{2.7}$$

As a consequence the B(E2) value for the excitation:

$$B(E2; i \to f) = 5B(E2; f \to i) \tag{2.8}$$

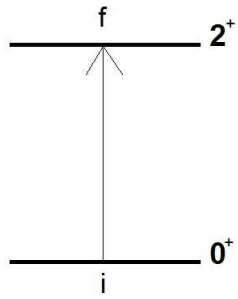

Figure 2.1: The figure represents an example of an excitation from an initial 0^+ level to a final 2^+

Rutherford scattering (Fig 2.2) provides a classical description of Coulomb interaction between a target with a charge Z_2 and a projectile with a charge Z_1 moving with respect to the target. On the basis of this description, a semi-classical treatment is avaible

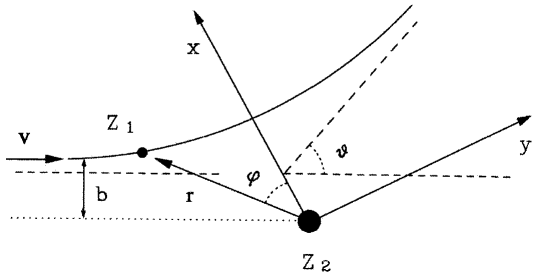

Figure 2.2: The figure represents the classical situation of Rutherford scattering. A projectile with charge Z_1, and velocity **v** is moving respect to a target with charge Z_2. The scattering is characterized by an impact parameter b and an angle of scattering θ, while ϕ is the angular position of the projectile respect the target during the interaction.

and it is valid for almost all the cases of low beam energy [34] (E_{beam}¡50MeV/u). In the not relativistic case the interaction hamiltonian for the excitation can be written as:

$$H' = \int d^3r_1 d^3r_2 \frac{\rho_1^{ch}(\mathbf{r}_1 - \mathbf{R}_1)\rho_2^{ch}(\mathbf{r}_2 - \mathbf{R}_2)}{|\mathbf{r}_1 - \mathbf{r}_2|} - \frac{Z_1 Z_2 e^2}{R(t)} \tag{2.9}$$

The interaction between the two nuclei as the point like particle is subtracted because it determines the trajectory and not the excitation. In order to semplify the expressions we require that only the target nucles is excitated and we consider the projectile like a point-like charge $\rho_2^{ch}(\mathbf{r}_2 - \mathbf{R}_2) \approx Z_2 e\delta(\mathbf{r}_2 - \mathbf{R}_2)$. In the center of mass frame the multipole expansion allows to write:

$$H' = Z_2 e \sum_{L>0,M} \frac{4\pi}{2L+1} \frac{1}{R^{L+1}(t)} Y_{LM}^*(\mathbf{R}(t))\boldsymbol{M}(EL, M) \tag{2.10}$$

It is possible to demonstrate [36] that the transition amplitude for excitation $i \to f$ is

$$a_{fi} = -\frac{i}{\hbar} \int_{-\infty}^{\infty} dt H'_{fi}(t) e^{i\omega t} \tag{2.11}$$

The reaction rate will be obtained summing this amplitude over all the projections.

$$w_{fi} = \frac{1}{2J_i + 1} \sum_{M_f M_i} |a_{fi}|^2 \tag{2.12}$$

The trajectory influences the interaction via the integral:

$$I_{LM}(\omega) = \int_{-\infty}^{\infty} dt \frac{1}{R^{L+1}(t)} Y_{LM}^*(\mathbf{R}(t)) e^{i\omega t} \tag{2.13}$$

this contribution appears in the cross section as a function of the multipolarity:

$$\frac{d\sigma_{fi}(\mathbf{L})}{d\Omega} = \left(\frac{\pi Z_2 e a}{\hbar sin^2(\theta/2)}\right)^2 \frac{B(EL; i \to f)}{(2L+1)^3} \sum_M |I_{LM}(\omega_{fi})|^2 \tag{2.14}$$

where a is the closest distance reached by the projectile.
If also magnetic interactions are cosidered, the scalar and vector potentials, generated by the projectile with charge Z_p, have to be used in the hamiltonian.

$$\phi(\omega, \mathbf{r}) = Z_p e \int_{-\infty}^{\infty} e^{i\omega t} \frac{1}{|\mathbf{r} - \mathbf{r}'(t)|} dt \tag{2.15}$$

$$\mathbf{A}(\omega, \mathbf{r}) = \frac{Z_p e}{c} \int_{-\infty}^{\infty} \mathbf{v}'(t) e^{i\omega t} \frac{1}{|\mathbf{r} - \mathbf{r}'(t)|} dt \tag{2.16}$$

This allows to obtain a more complete evaluation of the cross-section distribution:

$$\frac{d\sigma_{i\to f}}{d\Omega} = \frac{4\pi^2 {Z_P}^2 e^2}{\hbar^2} {a_0}^2 \epsilon^4 \sum_{\pi L M} \frac{B(\pi L, I_i \to I_f)}{(2L+1)^3} |S(\pi L, M)|^2 \tag{2.17}$$

where

$$\epsilon = \sqrt{1 + \frac{b^2}{a_0^2}} \tag{2.18}$$

considering that $\pi = E$ or M and

$$S(EL, M) = \int_{-\infty}^{\infty} r'^{-L-1}(t) Y_{LM} \theta'(t), \phi'(t) e^{i\omega t} dt \tag{2.19}$$

$$S(ML, M) = -\frac{1}{L m_0 c} \mathbf{L}_0 \cdot \int_{-\infty}^{\infty} \bigtriangledown' \{ r'^{-L-1}(t) \times Y_{LM}[\theta'(t), \phi'(t)] \} e^{i\omega t} dt \tag{2.20}$$

It is possible to evaluate the Coulomb cross section per solid angle as:

$$\frac{d\sigma_C}{d\Omega} = \sum_f \int \frac{d\sigma_{i\to f}}{d\Omega} \rho_f(E_\gamma) dE_\gamma \tag{2.21}$$

Where $\rho_f(E_\gamma)$ is the density final states in the target nucleus. Using 2.17 we obtain:

$$\frac{d\sigma_C}{d\Omega} = \sum_{\pi L} \int \frac{dE_\gamma}{E_\gamma} \frac{dn_{\pi L}}{d\Omega}(E_\gamma) \sigma_\gamma^{\pi L}(E_\gamma) \tag{2.22}$$

where $\sigma_\gamma^{\pi L}$ is the photoabsorption cross section of the nucleus at a fixed multipolarity. The two quantities used for this evaluation, the photoabsorption cross section and the number of virtual photons $\frac{dn_{\pi L}}{\Omega}$ exchanged between the target and the projectile, can be obtained using the following relations:

$$\sigma_\gamma^{\pi L}(E_\gamma) = \frac{(2\pi)^3 (L+1)}{L[(2L+1)!!]^2} \sum_f \rho_f(E_\gamma) \left(\frac{E_\gamma}{\hbar c} \right)^{2(L-1)} B(\pi L, I_i \to I_f) \tag{2.23}$$

$$\frac{dn_{\pi L}}{d\Omega} = \frac{Z_p^2 \alpha}{2\pi} \frac{L[(2L+1)!!]^2}{(L+1)(2L+1)^3} \frac{c^2 a_0^2 \epsilon^4}{\left(\frac{E_\gamma}{\hbar c}\right)^{2(L-1)}} \sum_M |S(\pi L, M)| \tag{2.24}$$

The angular dependence can be rewritten in terms of dependence from impact parameter because it is related to the scattering angle. For this reason the Coulomb cross section can be expressed as:

$$\frac{d\sigma_C}{2\pi b db} = \sum_{\pi L} \int \frac{dE_\gamma}{E_\gamma} n_{\pi L}(E_\gamma, b) \sigma_\gamma^{\pi L}(E_\gamma) \tag{2.25}$$

In order to obtain total Coulomb cross section, we need to integrate from a minimum impact parameter. The same result can be obtained integrating till a maximum scattering angle θ_{max}. This is essential at high beam energy (E_{beam}¿50MeV/u) where also nuclear excitation can have a strong role. As a consequence the number of virtual photons becomes:

$$N_{\pi L}(E_\gamma) = 2\pi \int_0^{\theta_{max}} d\theta sin\theta \frac{dn_{\pi L}}{d\Omega} \tag{2.26}$$

When kinetic energy of projectile increases, the number of virtual photons at high energy increase and in this way it is possible to access to high energy excitation state of the target (as in Fig 2.3).

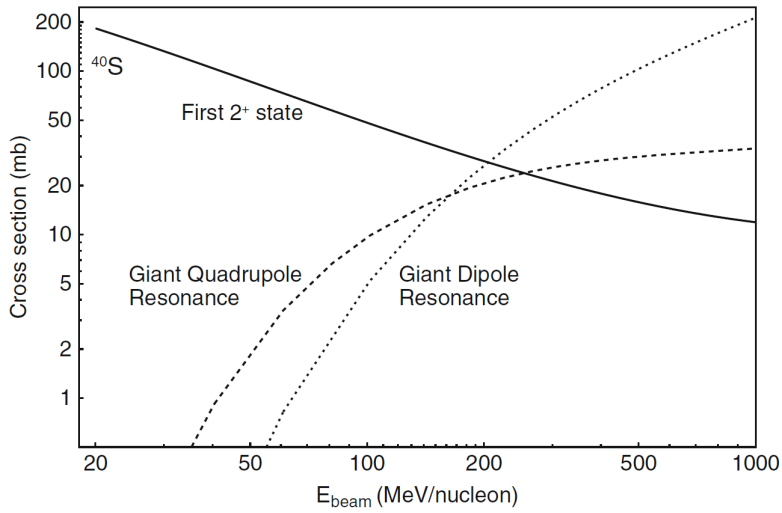

Figure 2.3: Calculated cross sections for intermediate-energy Coulomb excitation at different beam energies for a ^{40}S projectile impinging on a gold target [35]

2.2 Relativistic energy regime

If we consider a relativistic beam, the electromagnetic field in the target nucleus center of mass frame (considering that the projectile moves along z-axis) has to be expressed

as:

$$\phi(\mathbf{r},t) = \frac{\gamma Ze}{\sqrt{(x-b)^2 + y^2 + \gamma^2 (z-vt)^2}} \tag{2.27}$$

where b is the x-coordinate of the projectile trajectory, and

$$\mathbf{A}(\mathbf{r},t) = \frac{\mathbf{v}}{c}\phi(\mathbf{r},t) \tag{2.28}$$

Using a procedure similar to the one used for the general sitaution, and through some long calculations but straightforward [37] we obtain the Coulomb cross section as:

$$\sigma_C = \sum_{\pi L} \sigma_{\pi L} = \sum_{\pi L} \int \frac{dE_\gamma}{E_\gamma} N_{\pi L}(E_\gamma) \sigma_\gamma^{\pi L}(E_\gamma) \tag{2.29}$$

In the case of E1 excitation we have:

$$N_{E1}(E_\gamma) = \frac{2Z^2\alpha}{\pi}\left(\frac{c}{v}\right)^2 \left[\xi K_0 K_1 - \frac{v^2\xi^2}{2c^2}(K_1^2 - K_0^2)\right] \tag{2.30}$$

where the modified Bessel functions K_M are functions of $\xi(R) = \frac{\omega R}{\gamma v}$ with R as the distance of closest approach.
The spectrum of the virtual photons exchanged in a collision, shows a kind of cutoff at an energy that depends on the impact parameter. In particular (as in Fig 2.4) the number of virtual photons exchanged is considered to fall down approximately at:

$$E_\gamma^{max} \simeq \frac{\gamma\hbar v}{b} \tag{2.31}$$

which is called adiabatic cutoff energy. This value it is obtained via an interpolation of the virtual photon spectrum. This means that the spectrum does not stop at the cutoff, but the contribution at higher energies are considered small.

Scattering at relativistic beam enery requires a more complex quantum approach due to the fact that both coulomb and nuclear fields have a not-negligible role in the interaction. Thanks to the fact that scattering at these energies satisfies the hypotesis of eikonal approach, calculations are achieved in a simple manner.

2.2.1 Eikonal approach

The *Eikonal(straigth line) approximation* requires that a projectile with a kinetic energy in the laboratory frame E lose in the target a small energy ΔE to satisfy the relation $\Delta E/E_{lab} \ll 1$; as a consequence the scattering angle θ is very small ($\theta \ll 1$). Under these

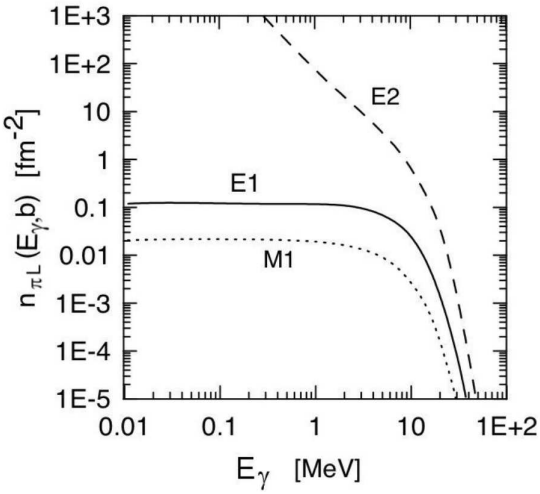

Figure 2.4: Energy spectrum of virtual photons, per unit of area, exchanged in a collision between 208Pb and 16O at 100 MeV/nucleon and with impact parameter b=15 fm [33]

conditions we can write the free-particle wave function, for a projectile colliding on a target as:

$$\psi(\mathbf{r}) = e^{ikz}\phi(z, \mathbf{b}) \tag{2.32}$$

assuming that $\mathbf{r} = (z, \mathbf{b})$, where the z axis represents the beam direction. According to the Distorted Wave approximation, the scattering due to a potential $V(\mathbf{r})$ induces a distortion in the free-particle wave function. The outcoming waves can be computed (after a partial wave-expansion) solving the Schrodinger Equation:

$$\left[\frac{d^2}{dr^2} + k_l^2(r)\right]\chi_l(r) = 0 \tag{2.33}$$

with

$$k_l(r) = \left\{\frac{2\mu}{\hbar^2}\left[E - V(r) - \frac{l(l+1)\hbar^2}{2\mu r^2}\right]\right\}^{1/2} \tag{2.34}$$

If we assume that the function ϕ varies slowly with respect to z and **b** we obtain:

$$\left|\nabla^2\phi\right| \ll k\left|\nabla\phi\right| \tag{2.35}$$

Neglecting 2nd and 3rd order terms, equation 2.33 in cylindrical coordinates becomes:

$$\frac{\partial\phi}{\partial z} = -\frac{i}{\hbar v}V(\mathbf{r})\phi \tag{2.36}$$

The solutions of this equation are:

$$\psi(\mathbf{r}) = e^{ikz + i\chi(\mathbf{b},z)} \tag{2.37}$$

where

$$\chi(\mathbf{b}, z) = -\frac{1}{\hbar v}\int_{-\infty}^{z} V(\mathbf{b}, z')dz' \tag{2.38}$$

is called the "eikonal phase".
Depicting $\Phi_{\mathbf{k'}}^{(-)}(\mathbf{r})$ and $\Phi_{\mathbf{k}}^{(+)}(\mathbf{r})$ the incoming and outcoming distorted waves, in the center of mass frame, (2.37) allows to write this as:

$$\Phi_{\mathbf{k'}}^{(-)}(\mathbf{r})\Phi_{\mathbf{k}}^{(+)}(\mathbf{r}) = e^{i\mathbf{q}\mathbf{r}+i\chi(\mathbf{b},z)} \tag{2.39}$$

with $\mathbf{q} = \mathbf{k'} - \mathbf{k}$. The eikonal phase can be expressed as a sum of two contributions:

$$\chi(b) = -\frac{1}{\hbar v}\int_{-\infty}^{\infty} U_N^{opt}(z', b)dz' + i\chi_C(b) \tag{2.40}$$

where U_N^{opt} is the nuclear optical potential and

$$\chi_C(b) = \frac{2Z_pZ_te^2}{\hbar v} ln(kb) \tag{2.41}$$

is called "Coulomb eikonal phase" and Z_p and Z_t are the charges of respectively the projectile and the target.
This result can be used to write the inelastic scattering amplitude in a easier way. In particular if we assume that the interaction potential is purely Coulombian, after the multipole expansion we obtain:

$$f_C(\theta) = i\frac{Zek}{\gamma\hbar v}\sum_{\pi LM} i^M \left(\frac{w}{c}\right)^L \sqrt{2L+1}e^{-iM\phi}\Omega_M(q)G_{\pi LM}\left(\frac{c}{v}\right)\langle I_f M_f|\,\boldsymbol{M}(\pi L, -M)\,|I_i M_i\rangle \tag{2.42}$$

$G_{\pi LM}$ are analytical functions for electric and magnetic field multipolarities, and $\Omega_M(q)$ is:

$$\Omega_M(q) = \int_0^{\infty} dbbJ_M(qb)K_M\left(\frac{wb}{\gamma v}\right)e^{i\chi(b)} \tag{2.43}$$

where q is the momentum transfer ($q = 2ksin(\theta/2)$), while scattering angles are represented by θ and ϕ.
On the basis of these results and using the same procedure discussed in the previous section, it is possible to obtain:

$$\frac{d^2\sigma_C}{d\Omega dE_\gamma}(E_\gamma) = \frac{1}{E_\gamma}\sum_{\pi L}\frac{dn_{\pi L}}{d\Omega}\sigma_\gamma^{\pi L}(E_\gamma) \tag{2.44}$$

where $\frac{dn_{\pi L}}{d\Omega}$ is the virtual photon number per solid angle

$$\frac{dn_{\pi L}}{d\Omega} = Z^2\alpha\left(\frac{\omega k}{\gamma v}\right)^2\frac{L[(2L+1)!!]^2}{(2\pi)^3(L+1)}\sum_M |G_{\pi LM}|^2\,|\Omega_M(q)|^2 \tag{2.45}$$

On the basis of the Eikonal approximation hypotesis we can consider $d\Omega \simeq 2\pi q dq/k^2$; in addition the closure relation for Bessel functions allows to obtain the following expression of Coulomb cross section:

$$\frac{d\sigma_C}{dE_\gamma}(E_\gamma) = \frac{1}{E_\gamma}\sum_{\pi L} N_{\pi L}(E_\gamma)\sigma_\gamma^{\pi L}(E_\gamma) \tag{2.46}$$

where $N_{\pi L}(E_\gamma)$ is the total number of virtual photons. This contribution can be evaluated as:

$$N_{\pi L}(\omega) = Z^2\alpha\left(\frac{\omega k}{\gamma v}\right)^2 \frac{L[(2L+1)!!]^2}{(2\pi)^3(L+1)}\sum_m |G_{\pi LM}|^2 g_M(\omega) \tag{2.47}$$

with

$$g_M(\omega) = 2\pi\left(\frac{w}{\gamma v}\right)^2 \int dbbK_M^2\left(\frac{\omega b}{\gamma v}\right) e^{-2\chi_I(b)} \tag{2.48}$$

In this relation $\chi_I(b)$ is the imaginary part of $\chi(b)$ (Eq. 2.40).

The theory of Coulomb excitation described in this chapter has shown the dependences of the Coulomb cross section by the states under invetigation: in particular through the nuclear structure B(Eλ) value. In experiments here discussed, these dependences will be exploited to collect informations on the pygmy states, subject of this PhD thesis. Fig. 2.5 shows the spectrum of virtual photons calculated for the experiments here discussed and the trend expected for the cross section of the first 2^+ level excitation and GDR excitation.

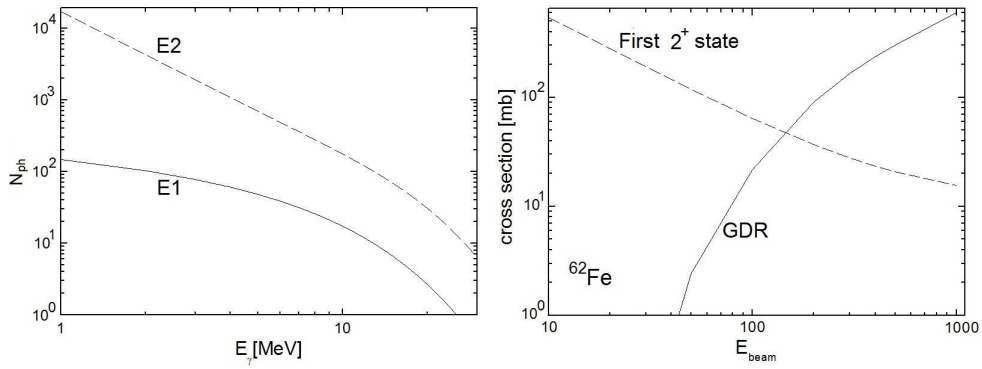

Figure 2.5: Left panel: energy spectrum of total number of virtual photons calculated for the experiments discussed in this thesis. Right panel: evaluation of the cross section of the first 2^+ level and GDR excitation for one of the measurements introduced in the next chapters.

Radiative γ decay after Coulomb excitation was measured. The number of the γs detected during the experiment can be obtained by the simple formula:

$$N_\gamma = \sigma_c N_T N_B \epsilon \tag{2.49}$$

where N_T is the number of scattering centres (target atoms),N_B is the number of projectiles and ϵ is the detection efficiency of the system. The statistics collected allowes to access to the Coulomb cross section and through this quantity, to the B(E1) value associated to the pygmy states.

CHAPTER 3

Experimental Setup

The investigation described in this work is about an experimental campaign on ^{62,64}Fe performed at GSI during PreSPEC-AGATA campaign (2012-2014) and on ^{70}Ni performed at Riken laboratories during the DALI2-HECTOR+ campaign (autumn 2014).
The dipole E1 response of neutron rich ^{62,64}Fe nuclei in an energy range from 6 to 10 MeV has been measured, while in ^{70}Ni case the acquired statistics allows to extends the energy range to 16 MeV. The exotic nuclei were produced and separated in flight at relativistic energies. Iron isotopes were produced at GSI FRS facility by the fragmentation of a 700 AMeV primary ^{86}Kr beam on a ^{9}Be target (2.5 g/cm^2). ^{70}Ni was obtained by fission of ^{238}U at RIKEN RIBF facility.
The beam cocktail of the products from the primary beam reaction was filtered and identified with a magnetic separator and brought to collide on a secondary target to measure the gamma decay of the projectile excitation. In case of Iron isotopes FRS magnetic separator provided the selection of the nuclei of interest. In ^{64}Fe measurement the exotic beam was made to collide at $\sim$400 AMeV on a thick lead target (1g/cm^2), while ^{62}Fe was made to collide over a thick gold target (2g/cm^2). In Riken the selection of ^{70}Ni was obtained with Big-Rips separator and the beam collided on the same gold target (2g/cm^2) as for the ^{62}Fe at 260 AMev.
At GSI the gamma ray detector system used was the AGATA array coupled with HECTOR+. AGATA [64] is an array of HPGe detectors electronically segmented while HECTOR+ is an array of large volume $LaBr_3$:Ce and BaF_2 scintillator detectors [58]. In Riken the DALI2 [5] array was coupled with eight $LaBr_3$:Ce detectors from HECTOR+ array. DALI2 is an array made by 180 NaI scintillator detectors organized in a particular configuration to maximize the efficiency and minimize the doppler broadening [5].

The selection and determination of the products of reaction on secondary target is needed to select coulomb excitation events. At GSI this selection was provided by the LYCCA array [59]. It consists in a system of silicon striped detectors (DSSSD) for ion tracking, plastic scintillators for time of flight estimation and a wall of E-ΔE telescopes made by thin silicon detectors coupled with thick CsI scintillators. In Riken ZDS magnetic separator provides the identification and selection after the secondary target. In this chapter the two experimental setups and their performances will be described. An overview of the two data acquisition systems, NARVAL coupled with MBS for GSI and RIBFDAQ for Riken, will be presented and in addition the trigger conditions will be explained.

3.1 PreSPEC-AGATA setup in GSI

The GSI facility was able to provide radioactive ion beams for the nuclear structure investigation. The improvement of detector systems for γ spectroscopy and for ion detection allowed to measure fine structures also in exotic nuclei. The experimental setup PreSPEC was prepared to couple the availability of rare isotope beams with the most accurate detector systems, concerning the γ detection it is actually the AGATA array.

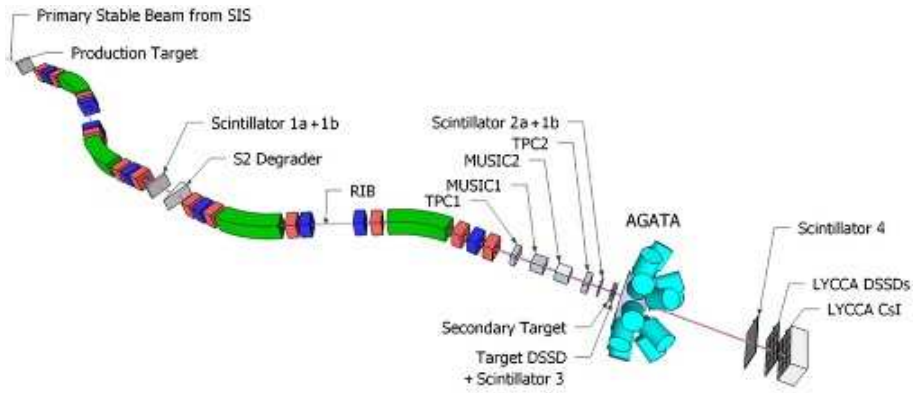

Figure 3.1: PreSPEC - AGATA setup (HECTOR$^+$) [4]

The radioactive ion beams are produced from a stable primary beam through its interaction with a Beryllium target: the products of the induced reactions form a cocktail beam. The magnetic separator FRS (FRagment Separator) allows the identification and selection of the rare ion beam of interest. This secondary beam is brought to impinge on a secondary target where reactions of interest take place. The reaction products

identification and the measurement of the trajectory of the incoming and outcoming beam from the target are performed with the calorimeter LYCCA(Lund-York-Cologne CAlorimeter). The γ detection was provided by the HPGe detector array AGATA (Advance GAmma Tracking Array) which was coupled with the HECTOR+, array of $LaBr_3$:Ce and BaF_2 scintillator detectors. In the next sections every apparatus will be described in detail.

3.1.1 The magnetic FRagment Separator

FRS is an in-flight magnetic spectrometer used to select radioactive isotope beams from a stable primary beam. The synchrotron SIS can accelerate stable beams from Hydrogen to Uranium up to 1-4.5 AGeV [60]. The beam is iniected in FRS beam line and impings on a production target where fragmentation or fission reactions occur and produce a cocktail beam with the reaction products. The technique exploited to identify and separate the ions in the cocktail beam is the $B\rho - \Delta E - B\rho$ method. The spectrometer consists of four stages referred to as S1, S2, S3 and S4. Each stage is made up of five quadrupoles, a $\pm 30^o$ dipole magnet and a pair of sextupoles. The dipole magnets are used to separate and identify the ions while the quadrupole magnets are used for both illuminate the field volume of the bending magnets and also focusing the beam on the focal planes (denoted as F1, F2, F3, F4). Higher order aberrations are corrected by sextupoles. This magnet system allows to have an high resolution spectrometer. The incoming beam is analyzed evaluating the magnetic rigidity and the time of flight; these two quantities allow to define the A/Q ratio of the ions. A profiled degrader is used on one hand to reduce the emittance of the beam and on the other hand to improve the separation of the ions. In fact the energy loss of an ion in matter scales as: $\sim \frac{Z^2}{Mv^2}$ and therefore the ΔE loss in the degrader depends on proton and mass number of the ion. The degrader can be shaped according two operational modes : achromatic and monoenergetic mode. The highest resolving power is obtained with achromatic mode. The term achromatic means that the horizontal position and angle of a particle at the last focal plane (F4) does not depend on its momentum. The achromatic mode has the advantage that the final spot size is kept small even when the momentum acceptance is large. In monoenergetic mode the energy loss of the fragments at F4 is independent from their horizontal position at F2. This mode is employed when a well defined energy bunch is needed at the final focal plane. For instance, when one is interested in stopping the selected fragments in a thin layer of matter at the exit of the FRS for β decay measurements. In order to complete

the identification, a system of ionization chambers is used to evaluate the Z value of the ions.

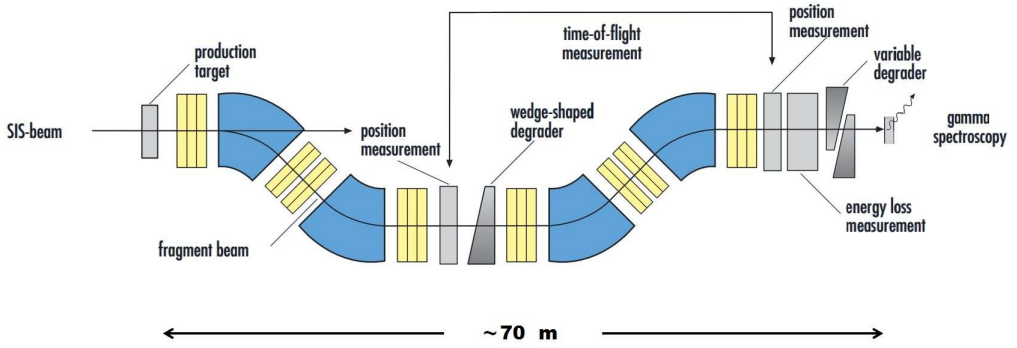

Figure 3.2: FRS setup [62]

The A/Q ratio is obtained by:

$$\frac{A}{Q} = \frac{eB\rho}{m_0 c\beta\gamma} \tag{3.1}$$

Magnetic rigidity and time of flight have to be evaluated for each ion on an event by event basis for the identification. The first quantity is extrapolated by measuring the position of the ions at the dispersive focal plane (F2) and at the final focal plane (F4). As regarding Time of Flight, all the beam line in FRS is 70 m long, but in order to have a precise evaluation of beta value of ions, the Time Of Flight is measured between S2 and S4 stage. The magnetic rigidity of an ion can be determined from the horizontal dispersion at the dispersive focal plane (D_2), the horizontal dispersion at the last focal plane (D_4) and the horizontal magnification value between these two focal planes (M_4). The two relations [65]:

$$B\rho_2 = (B\rho_0)_2\Big(1 + \frac{x_2}{D_2}\Big) \tag{3.2}$$

$$B\rho_4 = (B\rho_0)_4\Big(1 + \frac{x_4 - M_4 \cdot x_2}{D_4}\Big) \tag{3.3}$$

show the dependences of the magnetic rigidities in the two stage, S2 and S4. The $(B\rho_0)_2$ and $(B\rho_0)_4$ values are associated to ions that cross the focal plane in the central position, the measurement of the position of every single ion from the centre of the focal plane allows to determine the magnetic rigidity.

Timing detectors

The Time of Flight measurement is performed between S2 and S4 stage with plastic scintillator detectors.Two plastic scintillators are placed in S2: standard scintillator (labeled SC21) and a segmented scintillator, called "FINGER" detector [61]. In S4 stage just one standard scintillator is used. In order to have the best timing performance and limit the data throughput just to events where the scintillator signal from both the stage are present, the SCI41 signal is used as start while SC21 is delayed and used as stop. The dimensions of the scintillator SCI21 are 210x80 mm^2, whereas those of the scintillator SCI41 are 200x80 mm^2. The plastic material BC-4200 (Bicron corp.) provides a high light output and a fast rise time ($\sim$500 ps). The intrinsic ToF resolution with this system is in the range of 250 ps.The read-out is obtained with two PMT placed on the left and the right side coupled with fast single hit and multi-hit CFDs. The signal of the two PMTs is dependant from the position of the ion interaction, in fact it is affected by the time that light needs to cross the plastic material and reach the PMT surface. The ToF evaluation is therefore obtained considering the quantity [62]:

$$T = \frac{1}{2}\left[(SCI21_{left} - SCI41_{left}) + (SCI21_{right} - SCI41_{right})\right] \tag{3.4}$$

The ToF value is obtained by summing a proper offset. The β value is obtained dividing the distance between the two scintillators with the ToF and scaling this ratio with the speed of light. Finger detector is a plastic segmented scintillator, it can be used for ToF evaluation, as SCI21. Thanks to the segmentation this detector can be used also as tracking detector.

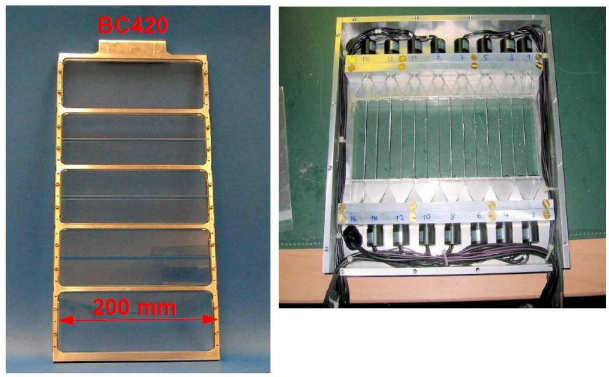

Figure 3.3: SCI21 standard scintillator, on the left, and Finger detector (15 strips), on the right [66]

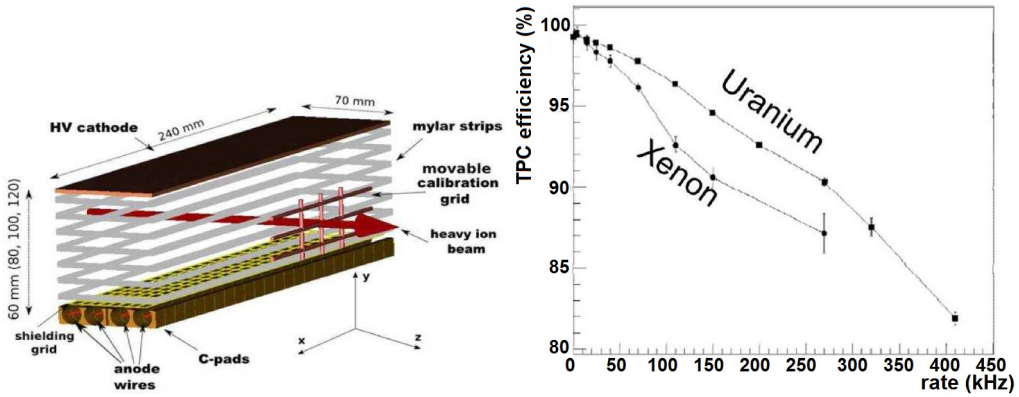

Figure 3.4: On left panel scheme of TPC components [66]. On right panel TPC efficiency at different rates [67]

Tracking detectors

Ion tracks can be measured using Time Projection ion Chamber or plastic scintillator commonly used for Time of Flight. The first type of detector is a drift chamber with a highly uniform electric field. The detector consists of a cathode, where the high voltage is applied, four anodes and two delay lines. The y-position is deduced from measuring the drift time of the electrons. As regarding x-position, the signals of the anodes are splitted and the time difference between left and right side's signal is compared. This setup of the detector provides two indipendent x-position measurements and four y-position measurements. The presence of precise delay lines allows to get an accurate position determination (0.18 mm of spatial resolution on x axes and 0.08 mm on y axes). The limit of these detectors is the loss in efficiency as the rate increases (Fig. 3.4). As discussed in previous paragraph, plastic scintillator detectors are used in S2 and S4 for Time of Flight measuerements but they can be used also for position determination. Standard scintillator read-out is obtained with two PMT placed on left and right side coupled with CFDs. As a consequence the difference between the two PMT time signals can be used to evaluate the relative position of the interaction points of the ions inside the detector. The FINGER detector is a plastic segmented scintillator (15 strips in 2012 setup, 70 strips in 2014 setup). Every strip has one own read out with PMT. This is used for the timing determination but also for measuring the height of the pulse. Knowing the position of every strip, it is possible to deduce the position of the ion interaction according to which strip has the most intense signal.

Z value evaluation detector

Nuclear charge Z value is estimated with ionization chamber detectors. Two detectors are operating at S4 stage called MUSICs (Multi Sampling Ionization Chamber). They are fast multiple sampling detector, with eight independent anode strips, a Frisch grid and a cathode. CF_4 is used as counting gas at atmospheric pressure (1013 mbar). Z value estimation is obtained exploiting the relation:

$$-\frac{dE}{dx} = Z^2 f(\beta) \tag{3.5}$$

In this way, after a proper calibration of MUSIC signals according to the β value, it is possible to extrapolate the Z value. The indipendent strips allow to obtain a multiple evaluation of the ΔE and therefore a precise measurment of the nuclei charge.

$$\Delta E = \left(\prod \delta E_i\right)^{1/8} \sim Z^2 \tag{3.6}$$

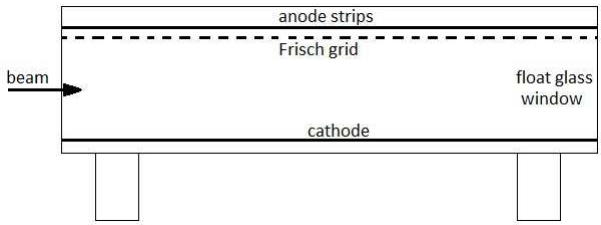

Figure 3.5: MUSIC detector scheme

3.1.2 The calorimeter (ToF and E-ΔE) LYCCA

Typical gamma spectroscopy experiments with relativistic exotic ion beams require an high precise detection of the outcoming projectiles from the secondary target. The best solution is an analysis magnet; if an high resolution magnetic device is not available, an array of E-ΔE telescopes is a good solution for selection of events related to reactions of interest. The LYCCA calorimeter [59] is a complex system of many particle detectors designed and realized to fit this aim. It is a flexible array of detector modules for tracking and characterizing products of reactions on secondary target. It is placed at the exit of FRS beam line, just some meters after the S4 stage of measurement. It is composed by an array of E-ΔE telescopes, a system of Double Sided Silicon Strip Detector (DSSSD) for tracking ions and a system of large area plastic scintillation detectors for high precise ToF measurements. In Fig. 3.6 the schematic layout of the array is represented.

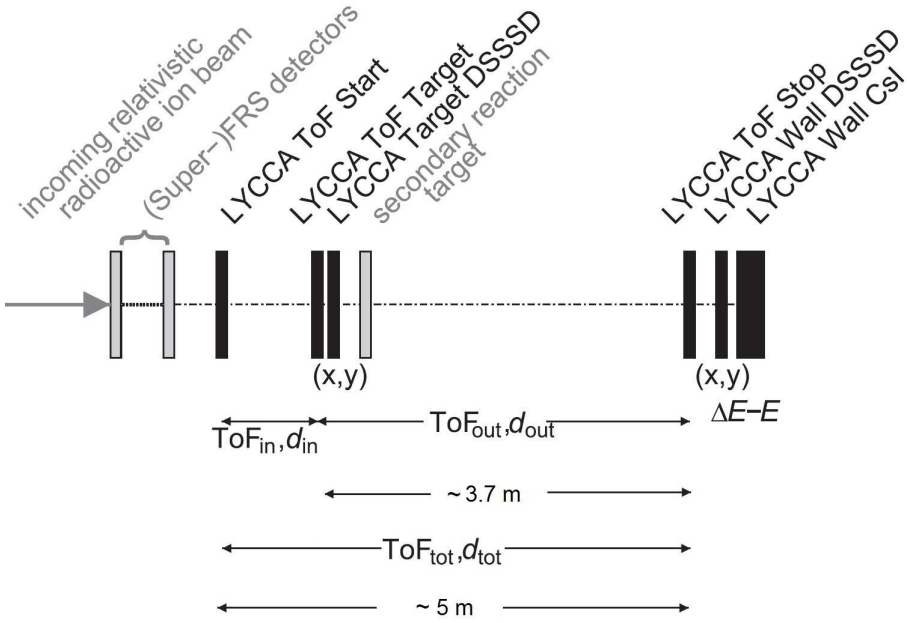

Figure 3.6: Lycca array schematic setup [59]

DSSSD detectors for ion tracking

Double Sided Silicon Strip Detectors(DSSSD)are used to track the beam ions before and after the secondary target. As shown in Fig. 3.6 a DSSSD panel is placed in front of the target, while a system of twelve panels are placed far behind the target(at a distance of $\sim$ 3.5 m): these panels form the DSSSD wall that coupled with CsI wall provide E-ΔE wall identification, as shown in Fig. 3.7.
Each tracking module is an ion implanted silicon wafer, silicondioxide(SiO_2) passivated, and operated totally depleted with floating guard rings. The thickness of these detectors is nominally 300 - 320 μm and they are squared shaped (60.1 x 60.1 mm^2) with an active area of 58.5 x 58.5 mm^2. This area is divided in 32 strips on both front (junction)p-side and rear (ohmic) n-side in orthogonal directions to provide the position of interaction in the two dimension. Interstrip distance is 30 μm on p-side while it is 200 μm on n-side. As regards energy resolution it is 1-2% at 5 MeV (tested with alpha particles) [62].

E-ΔE Wall for nuclei identification

The beam line ends in the LYCCA E-ΔE telescope array where the residual energy is measured with a thick CsI scintillator crystal while the ΔE is measured by a DSSSD

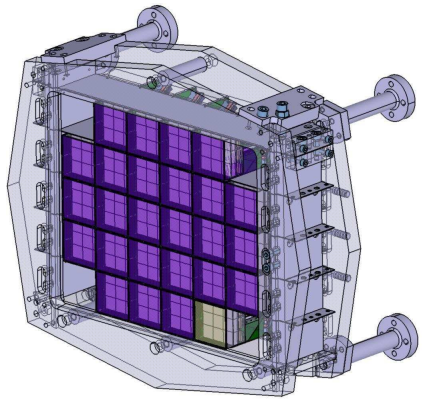

Figure 3.7: Technical drawing of Lycca-Wall [62]

Figure 3.8: DSSSD panel [59]

panel. This array is composed by twelve modules made by a DSSSD panel coupled with nine CsI detectors (as shown in Fig. 3.9 left panel). The CsI(Tl) crystals originate from Kharkov, Ukraine [62]. The scintillators front face is 19.0(5) x 19.0(5) mm^2 and the thickness is 33 mm (Fig. 3.9 right panel). This array allows to obtain E-ΔE matrices for identification of reaction products (as shown in Fig.3.10). The ΔE energy resolution allows to have a charge resolution of: $\Delta Z = 0.55$ [59].

Large area platic scintillators for ToF measurements

Large area plastic scintillators are used as start and stop detectors for high precision Time of Flight measurements. Every scintillator consists of a 2mm thick plastic membrane (type BC-420) with a diameter of 27 cm in a plastic frame, which contains 32 photo multiplier tubes (PMTs). The large number of PMTs allows to improve time resolution because, in principle, every PMT provides an indipendent measurement of the time when the ion interaction occurs (the reduction factor is $\sim \frac{1}{\sqrt{32}}$). Every PMT signal is dependent from the interaction position on the scintillator membrane. Tracking detectors can

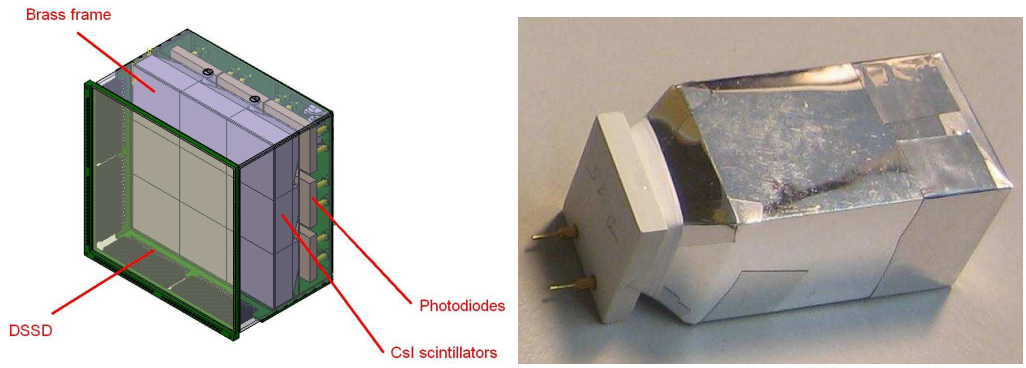

Figure 3.9: On the left panel E-ΔE telescopes module [62]. On the right panel the CsI crystal [62]

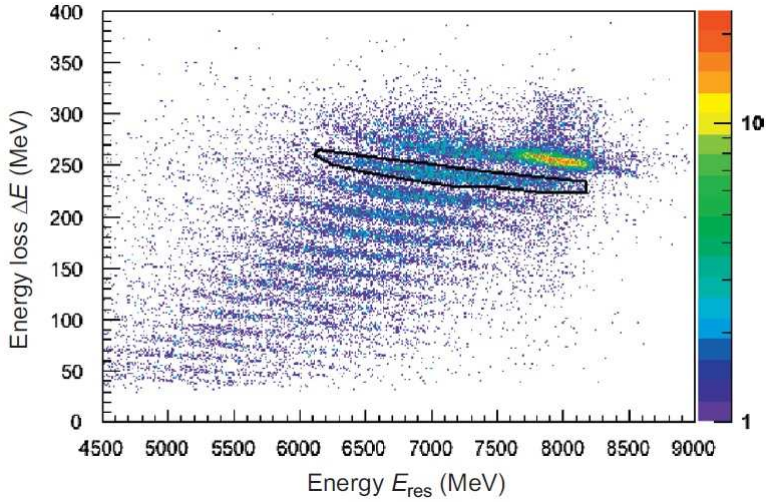

Figure 3.10: E-ΔE matrix from a ^{63}Co beam run, with a selection on Iron isotopes [59]

be used to recover the interaction position with an error of the order of 1 mm per dimension. This allows to correct this position dependent effect improving the time resolution of the system (expected to be less than 50 ps in the best experimental conditions [62]). One of these large area scintillators was placed at the exit of FRS (as start) and the other one was placed in front of the E-ΔE Wall (as a stop): in this way it was possible to get an accurate estimation of the projectile ToF and β values on the secondary target. In addition another scintillator detector was placed in front of the secondary target to have a an additional ToF evaluation. The operation way of this detector is the same of the large area ones but in this case the dimensions are smaller: it has a diameter of 7.3 cm and just nine PMTs on the border.

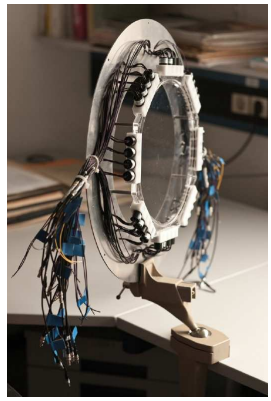

Figure 3.11: picure of 32 Hamamatsu R7400U PMTs mounted on an octagona acrylic glass frame around a 1 mm thick, 27 cm in diameter BC-420 sheet [68]

Using the measurement of ToF it is possible to identify the masses of reaction products with a resolution of $\Delta A = 0.55$ as shown in Fig.3.12

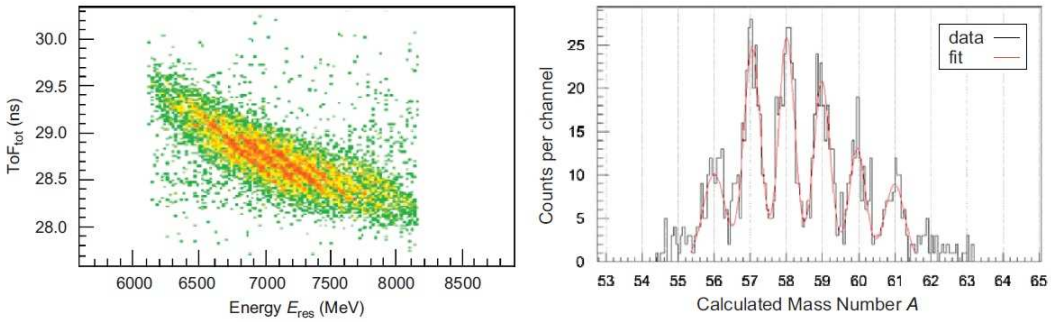

Figure 3.12: On the left an exemplum of energy vs ToF plot obtained with Lycca. On the right spectrum of masses obtained with energy and ToF measurement [59]during the first in-beam commissioning experiment in 2010.

3.1.3 AGATA

AGATA is the acronym (Advanced GAmma Tracking Array) for the European project aimed to construct and develop a new HPGe detector array to investigate nuclear structure by high precision gamma ray spectroscopy. The basic idea consists in exploiting the good energy resolution, the linearity of HPGe detectors and the possibility of an electronic segmention of the crystals to build an array able to track the gamma rays incoming on the detectors. The great goal of such apparatus is the possibility to reject

background radiation not coming from the target without losing efficiency due to the volume occupied by the anticompton shields and the possibility to have an accurate doppler correction for gammas emitted in-flight. Even if the geometry is a 4π array, some intermediate phases are planned. In 2009 a campaign started in LNL to test the performances of a demostrator composed by five triple clusters; the promising results brought to a physical campaign from February 2010 till spring 2012 in LNL. In 2012 the array was moved to GSI and from autumn 2012 till summer 2014 it was coupled with PreSPEC setup in GSI. In this phase the array was composed by five triple clusters and five double clusters. Actually the array is operating in GANIL coupled with VAMOS spectrometer. At the moment of the experiments here discussed, the number of operating crystals was varying between fifteen and twentytwo due to instabilities registered after mounting the last produced crystals.

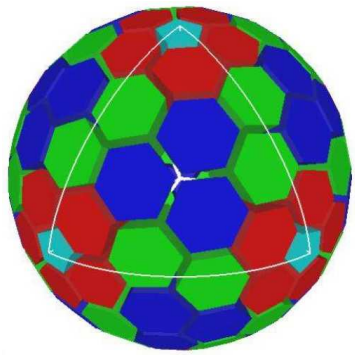

Figure 3.13: Planned AGATA final geometry [39]

AGATA geometry and design

The geometry of the array was planned taking in account two different objectives: the first was to maximize the efficiency and angular coverage, the second one was an inner space sufficiently large to host ancillary instrumentation. The best performing geometry was obtained after GEANT4 simulations [38]. The adopted solution consisted in a sphere composed by 180 hexagons and 12 regular pentagons. Due to the symmetries required for this buckyball structure, the hexagons are grouped in three classes characterized by slightly different shapes (as represented in Fig.3.14). The detectors are grouped in clusters: 60 triple clusters for the hexagons, each of them contains one crystal per type, while pentagons are canned individually. The detectors of the same cluster are in one cryostat with a liquid nitrogen system to keep the temperature at 90 ^{o}K. Also preampli-

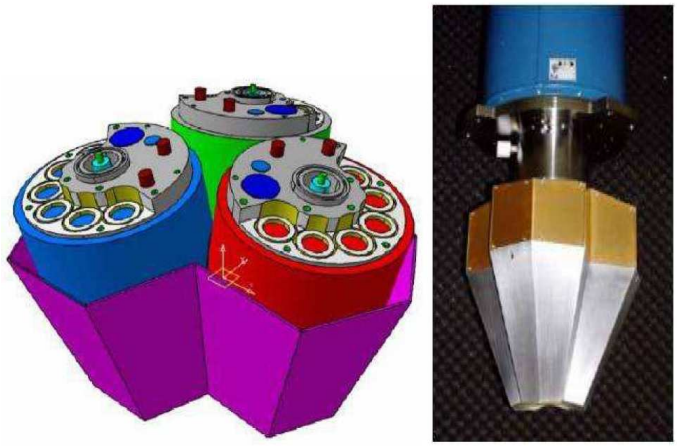

Figure 3.14: AGATA triple cluster: the three different hexagonal shapes are labeled with different colours

fiers require a cooling system to keep them at 130 ^{o}K. The inner radius of the array is fixed at 23.5 cm and the photopeak efficiency is expected to be around 50% for 1 MeV $\gamma-$rays [39]. The AGATA Demostrator was characterized by a very compact geometry, as shown in Fig.3.15. The AGATA geometry was changed to suite the GSI setup. In fact the hole planned in the AGATA array to host the beamline was too narrow for the beampipe of the GSI laboratory. The solution adopted consisted in a ring composed by triple clusters coupled to a ring of five double clusters [40] as shown in Fig.3.16.

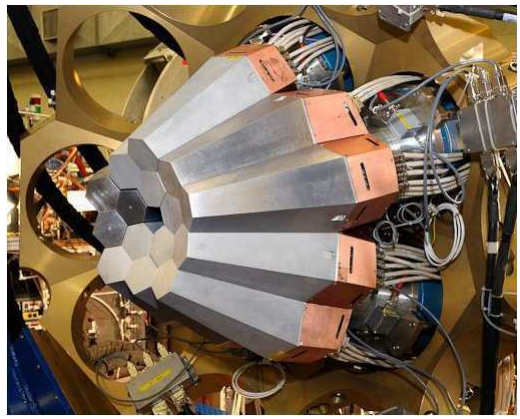

Figure 3.15: Picture of AGATA Demonstrator in LNL [39]

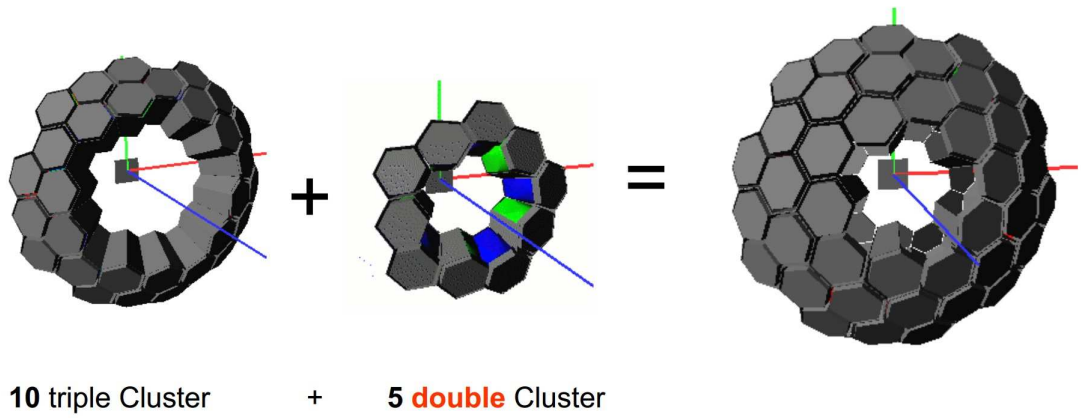

Figure 3.16: Schematic representation of solution for AGATA geometry in GSI [40]

AGATA electronics and Pulse Shape Analysis

The tracking of gamma rays requires high resolution in the determination of the interaction positions: approximately 5 mm of accuracy. This precision cannot be reached using only electronic segmentation because this would imply a granularity of 30000 voxels per crystal. This segmentation is too high to be handled, the critical point was solved using a lower segmentation (36 segments per crystal) and applying a pulse-shape analysis technique (PSA). AGATA detectors are n-type Germanium crystals produced by CANBERRA. They are characterized by semi-coaxial geometry (Fig.3.17) and a segmentation of the outer detector contact in 36 parts. The length is 90 mm, the diameter is 80 mm at rear with a tapering to an irregular hexagonal shape with an angle of 10^o at the front. The sector-wide segmentation crosses the middle of each hexagonal side, while the longitudinal segmentation forms rings with varying thickness: in particular the frontal segments are thinner than the backside ones. This choice has the aim to have a uniform number of interaction points per segments. AGATA was developed for γ spectroscopy in an energy range below 4 MeV: the number of interaction points in the first centimeters is very high. In order to reduce the interactions number per segment, the thickness of the frontal segments is shorter than 1 cm. The packing of these detectors was realized using the same technology developed for the clusters of EUROBALL array.

The Pulse Shape Analysis requires a digitalization of the signal before the processing of the data. For this reason all the 37 signals coming from a crystal (36 from the segments and 1 from the central core electrode) are digitised at 100 MHz after the preamplifier by high-resolution (14 bits) fast ADCs. Energy, position and time for every γ-ray interaction

Figure 3.17: Schematic representation of AGATA crystal segmentation

can be extracted using the PSA. These data are associated with both a unique time-stamp and a unique positional label, that are used by the acquisition system to associate signals from the same event. One of the advantages of digitalization consists in the possibility of using algorithms like, for example, the Moving Window Deconvolution algorithm to filter the signal and reconstruct the original charge collected, removing the effect of the preamplifier. A good energy resolution was achieved using short shaping time: this allows to sustain higher count rates compared to standard HPGe detectors (50 kHz per detector instead of 10 kHz). The determination of the position of interactions inside a segment with a precision of 5 mm has to face the problem that more than one interaction can occur inside the segment. Important information can be extracted not only by segments with a net charge deposition but also by the neighbour segments where just a transient signal is registered. The position of the interaction is deduced by comparing the signals with a reference basis of signals, where each signal corresponds to a well localised single interaction. Thanks to the fact that the detector response is linear, we can consider the signal from a segment as the superposition, weigthened on the energy, of the signals of every single interaction that took place in the voxel:

$$S(E,t) = \sum_{i=1}^{N} E_i S(x_i, y_i, z_i, t) \tag{3.7}$$

where N is the number of interaction inside the segment. Many approaches have been proposed to solve this equation: the solution in fact provides the information required for γ-ray tracking. Adaptive grid search [41], neural networks, matrix inversion [42], genetic algorithms [43], recursive subtraction [44] are some of these approaches: actually grid search algorithm is the solution applied, thanks to the small processing time that allows to use it also in on-line acquisition. At the moment the algorithm works on the assumption that the size of the segments is small enough to neglect a multiple interaction

in the segment (this means N=1 in Eq. 3.7). In principle this is not a realistic assumption but it was shown that this does not affect significantly the real performaces of the apparatus: especially in case of coulomb excitation and fusion reaction experiments. The key point for PSA is the choice of the signal basis. Experimental signal basis are not available yet, because they require long time to have sufficient statitistics. At the moment the basis are obtained with accurate calculations of the charge transported in the detector [45].

Gamma tracking algorithm

The information about the γ-ray interaction points is used in tracking algorithms to disentangle different γ-rays entering in the array and to discriminate and suppress the background. Algorithms avaible for γ-ray tracking can be divided in two classes: algorithms based on back tracking [46] and the ones based on clustering and forward tracking [47]. The back tracking algorithm exploits the fact that the photoelectric energy deposition is peaked around 100-250 keV and it is almost indipendent from the energy of the incident γ -ray. The algorithm assumes that the points of interaction where the energy released is in the range of photoelectric absorption, are the last interaction of fully absorbed γ rays. From these points the algorithm back tracks the gammas, computing scattering angles on the basis of the energy released in the interaction. In this way the algorithm can reconstruct the previous intercation and in the end it is able to reconstruct all the γ-ray tracks. This algorithm showed less efficiency and a worse Peak to Total ratio than the algorithms of the other class [48]; for this reason it is not actually implemented in the analysis code used for the experiments discussed here. The forward tracking algorithms start from the identification of clusters of interaction that could belong to a single γ-ray. In this case the Compton cross-section abundance in forward direction is exploited. The clusters are composed by interaction points with an angular distance between each other (link algorithm) or respect to a given point (leader algorithm) lower than a threshold value. The next step of this type of algorithms is the investigation of every cluster to determine if it is composed by interaction points belonging to one single γ-ray. The criteria used for this evaluation are listed below.

- The tracking algorithm uses the angle-energy relation in Compton scattering to evaluate the most likely sequence of interactions. This is applied evaluating the following figure of merit function:

$$FoM = \sum_{j=1}^{N-1} W_j \left(\frac{E_{\gamma'} - E_{\gamma'}^{pos}}{E_\gamma} \right)^2 \tag{3.8}$$

where E_γ is the sum energy of the N-1 interactions, $E_{\gamma'}^{pos}$ is the energy of scattered photons according to Compton scattering relation. For a cluster of N interactions, all the N! combinations are tested and the cluster is accepted if for at least one combination the FoM value is smaller than a predetermined value.

- When a cluster is composed by a single interaction, the algorithm evaluates the consistency between the energy of the hypothetical γ-ray and the depth reached in the crystal. If this two quantities are consistent, the algorithm decides if considering it as a photoelectric event or discarding it as spurious Compton scattering event, using a Monte Carlo approach. If two gammas with 511 keV energy are identified and an energy release is identified in the middle, the code consider this event a pair production and sums the energies.
- The algorithm tries to recover intially descarded clusters, combining them and evaluating the FoM value again. If the obtained value is acceptable, the cluster is recognised as a good event. If this is not the case, the cluster is definitively descarded as an incomplete scattering of the incident gammas. In this way it is possible to obtain a Compton backround suppression, without loosing angular covarage or efficiency due to compton shields. This means an higher photopeak efficiency and a better Peak to Total (P/T) ratio. Fig. 3.18 shows an example of clusterization of interaction points in an ideal 4π HPGe shell.

At the moment two forward tracking algorithm are avaible in Narval DAQ system (see subsection 3.1.5) for experimental data analysis: Orsay ForwardTracking (OFT) [48] and Mars Gamma-ray Tracking (MGT) [49]. The last one version is the most used in analysis codes, and also in the analysis here presented, because it has shown, till now, the best performances.

AGATA performances

The experimental campaign of the AGATA demonstrator at LNL has provided important information on the performances of the AGATA array. Here a brief summarize of the performances at high energies will be presented. The aim of the experiments discussed in this thesis is indeed measuring high energy gamma rays. At LNL precise calibration measurements provided informations on the energy resolution in the range of 2 - 9 MeV. Am-Be-Ni and Am -Be-Fe sources were used to cover this wide energy range. This type of sources exploits the α decay of ^{241}Am to induce the reaction ^{9}Be(α,n)^{12}C. The neutrons emitted are thermalized by a paraffin shield and are used to induce (n,γ) capture

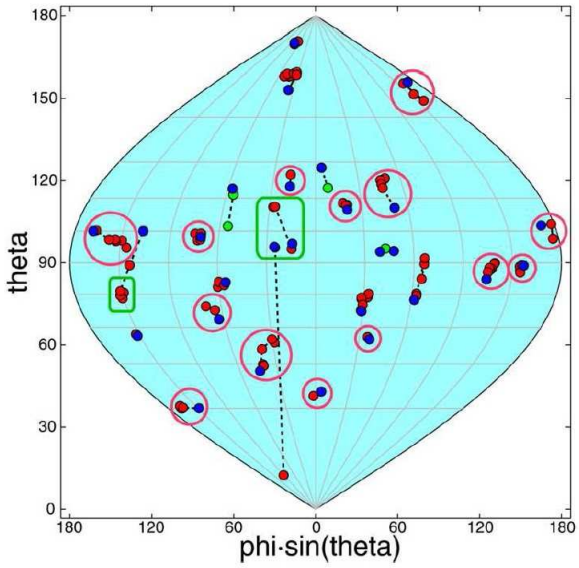

Figure 3.18: Schematic representation of interactions of 30 γ-rays detected in an ideal HPGe 4π shell, the interaction circled with red line are cluster of interaction correctly tracked, while the ones circled with green line represent clusters badly tracked [39]

reactions on Fe and Ni (for more details see [50], [51]). In the left panel of Fig.3.19 the energy resolution is plotted as a function of the energy. Both data for single crystals and all the demonstrator are plotted. It is possible to notice that the data follow the expected $\frac{1}{\sqrt{E}}$ trend. Performances at high γ-ray energies were investigated with the measurement of 15.1 MeV γ-rays emitted in the reaction d(^{11}B,nγ)^{12}C at E_{beam}=19.1 MeV (for more details see [50], [51]). In the right panel of Fig.3.19 the deviation of the centroid of peaks measured from the tabulated energies is reported: the data from sources and from the reaction described above allow to show that the array is characterized by a very high linearity also at high energies. Another important aspect is the efficiency: in particular the efficiency of tracking algorithms compared to a simple add-back of the energies of interactions identified by PSA. This estimation is strongly dependent from the background and multiplicity of the γ-rays. An overall indication ([50], [51]) is that tracking algorithms (MGT libraries in particular) have very high efficiency at low energies (below 4 MeV), while at very high energies (above 10 MeV) the performances of these algorithms decrease: if the background level is sufficiently low the add-back technique can gain 25% of statistics compared to tracking algorithms. This estimation, as already explained, is strongly dependent on environmental conditions, for this reason an evaluation valid for

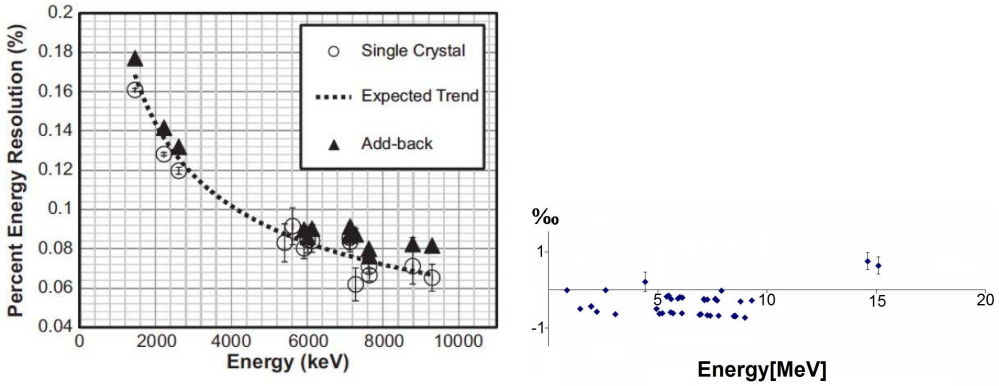

Figure 3.19: Left panel: Energy resolution plotted as a function of γ-ray energy. Data are collected with Am-Be-Fe and Am-Be-Ni calibration sources. Empty circles represent data of single crystals, empty triangles data of add-back of all AGATA [50]. Right panel: Deviation from the tabulated values of centroid of measured photopeaks, the deviations are expressed as fractions of the energy measured [51].

all the laboratories in which AGATA array will be uesd, is at the moment not yet fixed.

3.1.4 HECTOR$^+$

HECTOR$^+$ is an array of $LaBr_3$:Ce and BaF_2 scintillator detectors of large volume. The size of a crystal is 3.5″x8″ for $LaBr_3$:Ce detectors and 7″ x 7″ for BaF_2 detectors.
$LaBr_3$:Ce detectors have optimal performances compared to other scintillators. They are in particular characterized by an excellent energy resolution ($<3\%$ at 662 keV), good time resolution ($<$1 ns) and good efficiency.
BaF_2 scintillators are carachterized by good efficiency, excellent time resolution ($<$200 ps) but poor energy resolution($\sim 10\%$ at 1 MeV). The fast decay time 16 ns for $LaBr_3$:Ce and 0.7 ns for the fast component and 0.7 μs for the slow component of BaF_2 allow these detectors to stand very high rates.
One aspect to take into accont using LaBr detectors is the internal radiation. These crystals contain ^{138}La that have a mean life of 10^{11}y and a contamination of ^{227}Ac [71]. The decay of these radioactive nuclei and the one of their daughter nuclei produce the well known spectrum of internal radioactivity shown in Fig. 3.20. This scintillators array is characterized by large volume detectors to increase efficiency in order to detect high energy γ rays. In the 2012 setup ten $LaBr_3$:Ce detectors were used coupled with eigth BaF_2 detector, while in the 2014 only two $LaBr_3$:Ce detectors were missing as installed in

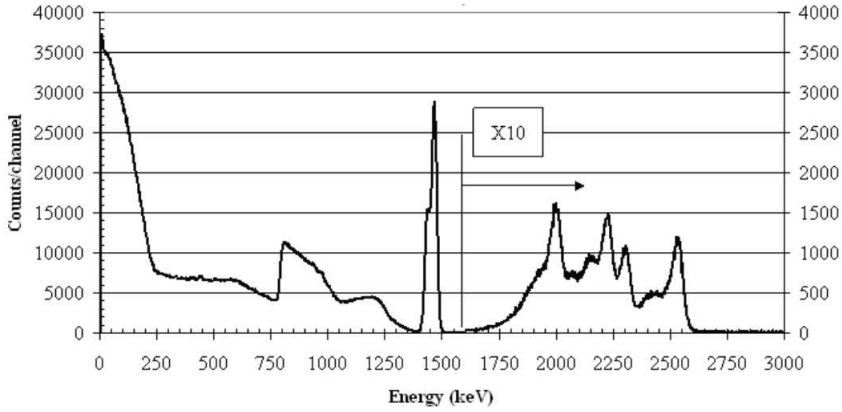

Figure 3.20: Energy spectrum of the internal radioactivity of a LaBr detector [71].

	LaBr		**BaF**	
	2012	**2014**	**2012**	**2014**
142^o	2	0	4	4
98^o	4	2	4	4
68^o	4	4	0	0
22^o	0	2	0	0

Table 3.1: number of scintillator detectors at different angular positions in 2012 and 2014 setup.

Riken laboratory. These detectors were placed at different angles as shown in Fig. 3.21.

$LaBr_3$:Ce scintillators were placed at forward angles. Their performances at high energy were tested and simulated [58] showing high efficiency and a good energy resolution, as shown in Fig. 3.22.

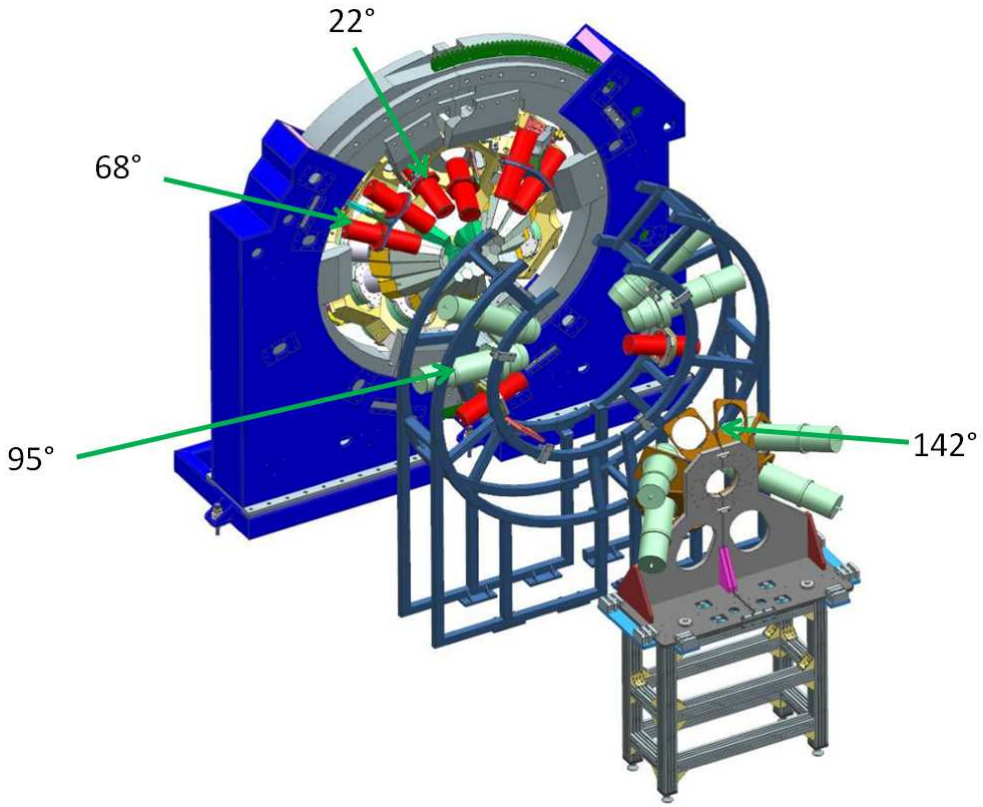

Figure 3.21: HECTOR$^+$ setup in 2014, red detectors are $LaBr_3$:Ce scintillators while the light green ones are BaF_2 scintillators, in grey the AGATA clusters

3.1.5 The Data AcQuisition system at GSI

The main features of the complex data acquistion system used in GSI for the experiments discussed in this PhD thesis, are here described. These informations are based on [57] where more details can be found.

GSI DAQ for PreSPEC AGATA setup was built using two main actors: GSI DAQ system MBS [69] and GTS-NARVAL [70] DAQ system. The former was reposnible for the triggering logic and data collection from FRS, LYCCA and HECTOR+ systems while the latter was dedicated to AGATA. The complexity of the acquisition is mainly connnected with the different nature of the systems: analogue system for MBS side and completely digital for GTS(Global Trigger and Synchronization system)-NARVAL side.

The MBS DAQ is organized in eleven branches, each branch is equipped with: a VME crate controlled by a RIO3 or RIO4 processor, a TRIVA trigger module. The TRIVA modules are linked together to guarantee that the system operates synchronously. This DAQ

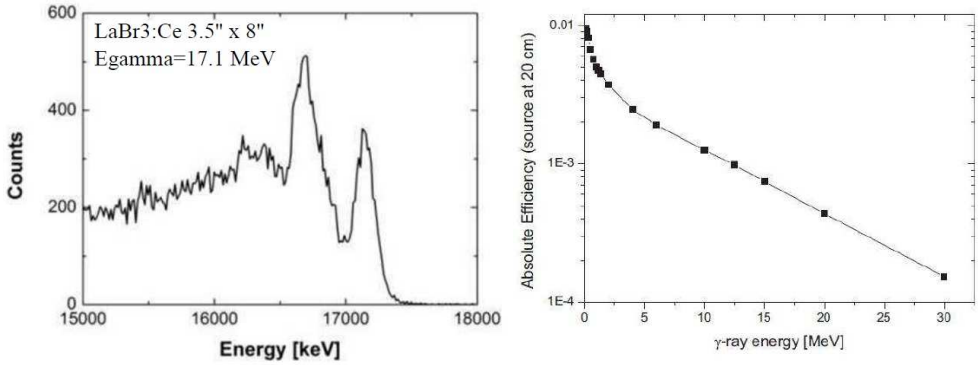

Figure 3.22: On left panel: gamma spectrum of the reaction $11^B(p,\gamma)12^C$ at 17.6 MeV acquired with $LaBr_3$:Ce scintillators. It is possible to see a clear separation of full energy peak and single escape [58]. On right panel $LaBr_3$:Ce scintillator efficiency obtained with GEANT3 simulations [58].

system is divided in three subsystems: one for FRS, one for LYCCA and one for HECTOR+. Each subsistem has a proper MH-TDC: this module allows to record the time of all hits. In this way it is possible to monitor and check the hits time distribution. It is possible therefore to monitor the presence of a "good" hit, using an external time reference coming from the scintillator of the last focal plane in FRS.
In this setup the Master crate was labelled TRLO (TRigger LOgic). It assured the synchronous read out of all crates for every Master trigger generated by a TRLO firmware. TRLO crate included also an AGata VME Adaptateur (AGAVA) that allows to couple VME-based system to AGATA system and GTS timestamp for any MBS event.
As previously explained, the signals from AGATA detectors are processed by digitizers. They run with a common clock provided by GTS. The GTS also gurantees the timestamping. Data are stored till trigger processor decides for validation or rejection. In case of rejection the event is descarded, in case of validation it is sent to computer farm.
The GTS, the AGATA triggering system, is organized as a tree where the leaf are the crystals, as shown in Fig. 3.23. When a core crosses the threshold a request is sent to trigger processor. The decision of the processor is sent back to the requesting module through the tree. The configuration of this system foresees two partitions: one for AGATA detectors, one for particle and ancillary detectors. When a partition asks for a trigger, it is "up" for 1 μs. A coincidence is set if both of them are up for 6μs, with a coincidence window $\pm$3 μs around the ancillary request. Each GTS leaf that has a request in coincidence window is validated. The full system is validated by VME based electronics. The trigger

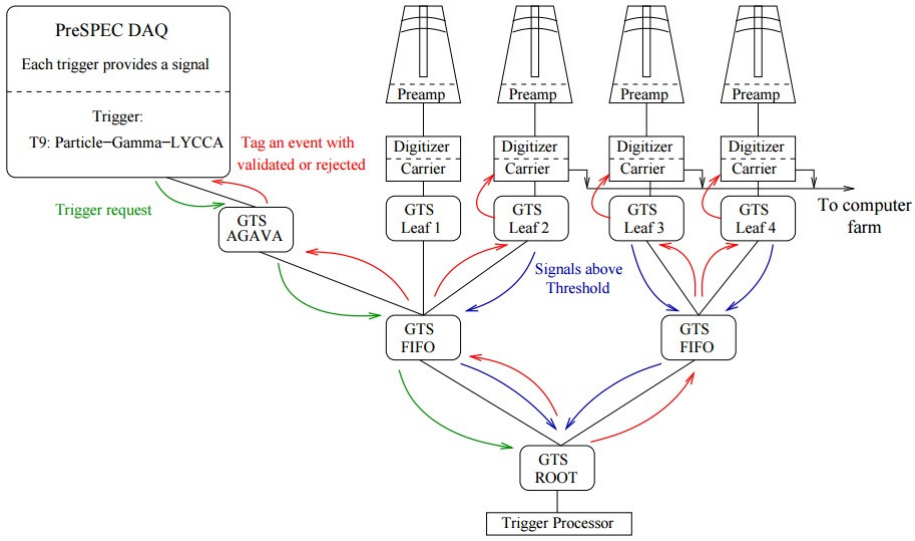

Figure 3.23: GTS organization scheme. Every detector is a leaf, when the core signal rise up from the threshold a request is submitted to trigger processor (blue arrows). GTS AGAVA represent all the other detectors in PreSPEC setup, therefore for every MBS event it sends a request to trigger processor (green arrows). It validates the γ-rays event coincidences and sends back the decision (red arrows) [57].

decision inside GTS system takes 10 μs. However in PreSPEC the count rate is so high that it is not possible to use such type of trigger hierarchy. Therefore the read out of the system is controlled by the trigger from TRLO firmware.
NARVAL system foresees for every detector three different ”actors”. Each actor apply an action to the data: the ”producer” collect the signal from the carriers, the ”preprocessing” apply energy calibrations and time allignements, the ”PSA” apply a grid-search analysis to assign the position coordinates to every interactions. Other three actors operate after these first three. The ”Event Builder” builds the event according to timestamps, the ”Merger” merges PreSPEC and AGATA data, while the ”Tracking” apply tracking algorithms to AGATA data to disentangle the γs.
The time required by MBS to process data is at least 90 μs. The easiest way to reduce the dead-time is to select only good event to be written. Scintillator in last focal plane of FRS provides the trigger request for the incoming ion from FRS, the plastic scintillator in front of the secondary target and the plastic scintillator in front of the wall provide the trigger request for LYCCA: without tracking of the ion no doppler correction is possible and the data are useless. As regards γ triggers, copies of AGATA detector core preampli-

fier signals are sent to analog CFDs and a logic OR is used for a γ trigger request, a logic OR of HECTOR+ signals, after a coincidence with plastic scintillator in last focal plane, is used as further γ trigger request.
The calibration of the detector system, the beam and the gain drift monitoring required dedicated triggers. Three different triggers were setted to collect in-beam data. One trigger (labelled with number 10) required just one signal in scintillator in last focal plane: this trigger was properly scaled down and it was used as normalization trigger. It is indeed the most bias free trigger. Another trigger (number 9) required coincidence with FRS, LYCCA and AGATA, while the last one (number 8) required FRS,LYCCA and HECTOR+. The hierarchy between triggers were defined by the number of the trigger. Inside MBS event a tag from AGAVA was written in addition to GTS-timestamp. MBS event was written for both the tags. In this way GTS system did not discard events with γ rays detected only by HECTOR+. Verifications were performed using an MBS process, the Time Sorter, to prove the consistency between MBS and NARVAL (see Fig. 3.24). This proof demonstrated the possibility to sort event-by-event the data collected with MBS and NARVAL.

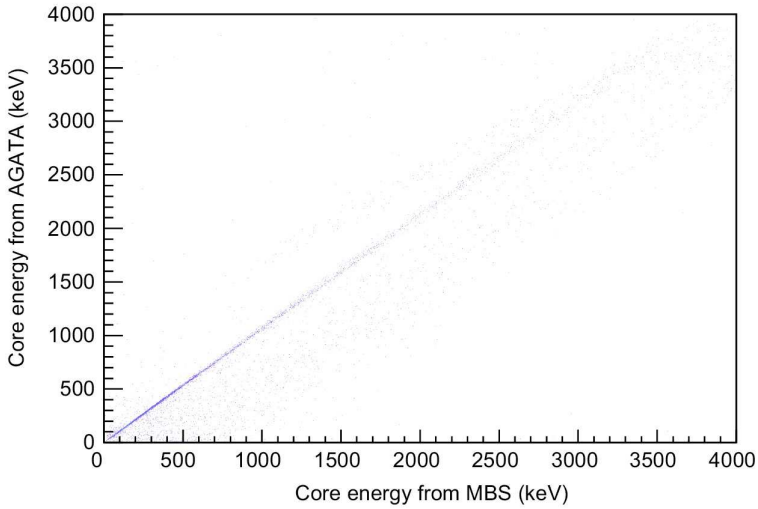

Figure 3.24: comparison between the core energy spectrum for one crystal of AGATA acquired with NARVAL system and MBS system [57].

3.2 DALI2-HECTOR+ setup in Riken

One of the experiments here discussed was performed in RIKEN laboratories with DALI-2 setup. RIKEN laboratories have created a very important facility for radioactive ion beams. This facility is called RIBF (Radioactive Ion Beam Facility); it can provide primary beams up to 440 MeV/nucleon (350 MeV/nucleon for heavy ion beams) and the goal is to reach 1pμA of intensity. These performances are obtained using a variable-frequency-heavy-ion linac (RILAC) as injector in a sequence of four ring cyclotrons. The cyclotrons: RRC (ring cyclotron),fRC (fixed frequency ring cyclotron), IRC (intermediate ring cyclotron) and SRC (superconducting ring cyclotron) deliver the beam in an isotope separator where a primary target is used to produce the radioactive beams. This separator is called Big RIPS and it allows to produce and select exotic ion beams. In the DALI-2 setup, the isotope beam of interest is delivered on a secoondary target where the reactions under investigation take place. This target is rounded by an array of NaI scintillator γ-ray detectors (DALI2). These detectors allow to study γ ray emission induced by the reactions on the target. The reaction products coming out from the secondary target are identified with a magnetic spectrometer: ZDS (Zero Degree Spectrometer). Here a brief description of the setup will be presented, using [55] and [5] as main references.

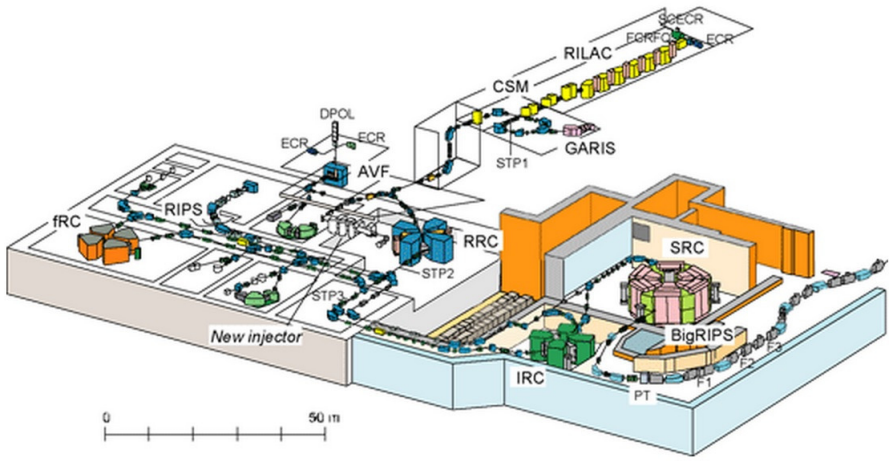

Figure 3.25: Scheme of the RIBF facility at RIKEN

3.2.1 Big Radioactive IsotoPe Separator

BigRIPS is a magnetic separator used to produce and select Rare Isotopes Beams. The main characteristics of this separator consist on the large ion-optical acceptance, the two

stage structure and the high precision particle identification. The advantage of a large acceptance mode of operation consists in the possibility to use ^{238}U fission reaction mechanism, beside the usual fragmentation reaction. This allows to enlarge the neutron rich exotic area accessible with the beams. The first stage of BigRIPS is dedicated to production and separation of rare isotope beams, while the second one is used for analysis and identification of the beams provided. The beamline of BigRIPS is 78.2 m long: two dipoles and four superconducting tiplet quadrupoles are placed in the fisrt stage while ten superconducting tiplet quadrupoles and four dipoles are present in the second stage. The dipoles are operating at room temperature and the bending angle is 30 degrees. Except the two triplets at the border between the two stages, every tripet quadrupole (STQ) is equipped with a superconducting sextupole to correct second order chromatic and geometrical aberrations. The large acceptance is determined by large aperture quadrupoles: $\pm$ 40 mrad of angular acceptance horizontally and $\pm$ 50 mrad vertically with a momentum acceptance of $\pm 3\%$. The two stages are designed as a mirror-symmetric achromatic system: achromatic conditions are fullfilled at the three focal planes on the beamline (denoted with F2, F3, F7). The separation of the fragments is achieved by magnetic rigidity analysis and the energy loss in achromatic degraders with wedge shapes inserted at dispersive focal planes (namely denoted with F1 and F5).
As introduced before, while the first stage is used for production and separation of RI beams, the second one is focused on the analysis of the beam. The identification is obtained with the same technique used in FRS: Time of Flight and positions at focal planes are measured to estimate the A/Q value of the ions, while a ionization chamber is used to evaluate the charge of the ions, that corresponds to Z value, except in the case of charge states.

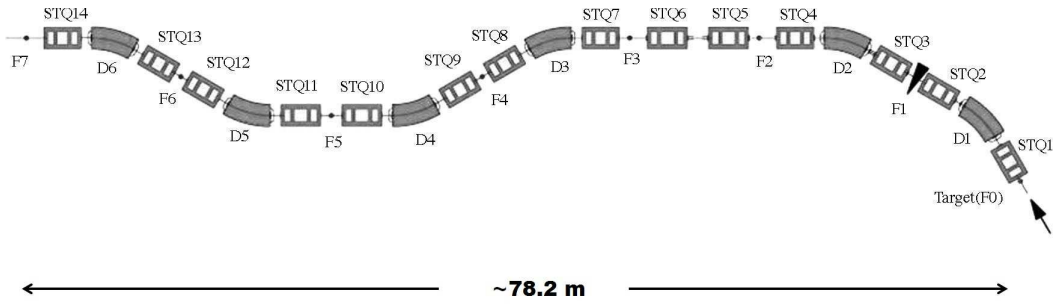

Figure 3.26: Scheme of the BigRIPS setup

Time of Flight measurement

Time of Flight is obtained with two platic scintillators placed along the beam line at F3 and F7 focal plane (Fig. 3.27). The dimension of the active area is: 120mm x 100mm. The timing resolution is lower than 100 ps, but the performances of these detectors are affetcted by radiation damage: for this reason every 48 hours of beamtime the scintillators has to be changed.

Figure 3.27: Picture of one of the two scintillator used for F3-F7 Time of Flight

Position measurement at focal plane

Every focal plane is equipped with position-sensitive parallel plate avalanche counters (PPAC) in order to estimate the position of the ions. These detectors provide a two dimensional measurement of the position of the ions. As shown in Fig. 3.28 on both dimensions the signal produced by the incoming particle is splitted and sent to two read-outs through a delay line. The estimation of the time differences of the read-outs can be used to extrapolate the interaction position. Position resolution is depending from the charge of the ions incoming. For Nickel isotopes it is expected to be 0.2-0.3 mm. This kind of detectors are affected by electrical discharge, the usage of Ag electrodes reduces this phenomena. Another chritical aspect is the rate acceptables for this detectors: for Z values of the order of ten the maximum rate is 1 Mcps.

Charge measurement

As in FRS the charge of the ions is measured with a MUlti-Sampling Ionization Chamber (MUSIC). As shown in Fig. 3.29 6 channels for read-out are used. The resolution obtained is ΔZ=0.21 . This value get worse when the count rate increase: in particular around 100 kpcs the recombination of electrons and ions worsens the resolution.

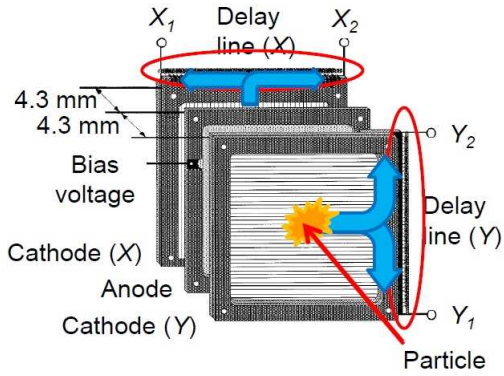

Figure 3.28: Scheme of the operating mode of PPACs [52]

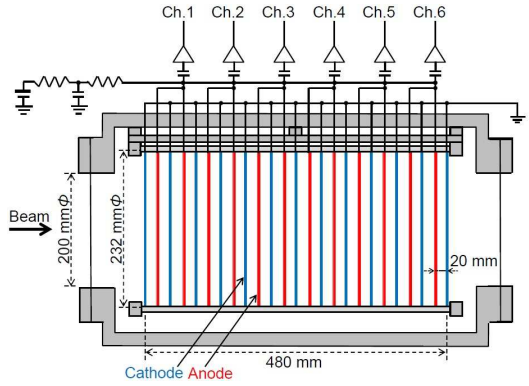

Figure 3.29: Scheme of the MUSIC used in BigRIPS [52]

3.2.2 Zero Degree Spectrometer

The Zero Degree Spectrometer is a magnetic spectrometer to analyze reaction products in experimental setups where the RI beam is delivered on a secondary target placed at the stage labelled as F8. It consists in a two-bend achromatic system with anti-mirror symmetry. It is composed by two dipoles and six triplet quadrupoles with the same design of the ones used on BigRIPS beamline. The final focus stage (F11) is fully achromatic in the standard operating way of ZDS. The transport from F7 to F8 is achieved using two triplet quadrupoles as dispersive telescope to match BigRIPS setup with Zero Degree Spectrometer setting.

If the radioactive beam is delivered at F11 stage, the ZDS is tuned to maximize the transmission efficiency.

ZDS can be used in different operating ways, for example it can be used in achromatic large acceptance way or in high resolution dispersive setup. The mode is chosen de-

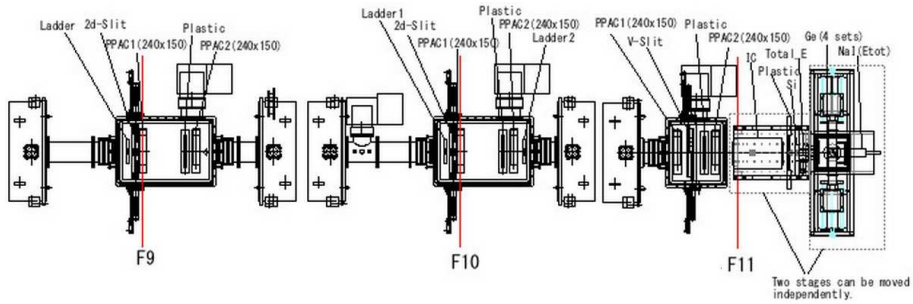

Figure 3.30: Technical drawning of Zero Degree Spectrometer

pending on the experiment requirements. During the experiment here discussed the ZDS was setted with large acceptance setting.
The identification method is the same used for BigRIPS, and also the detector types involved. On F11 a Total Kinetic Energy counter is used: it is a $LaBr_3$:Ce detector 3"x3" in which the ions are implanted. The aim is refinining the identification, to identify and exclude charge states.

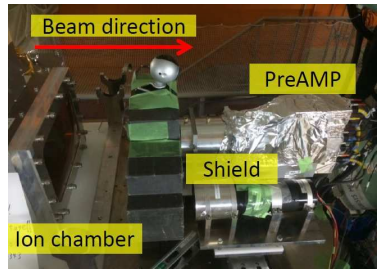

Figure 3.31: Picture of the TKE counter at F11 [53]

3.2.3 DALI2 and HECTOR+

The experiment about coulomb excitation of ^{70}Ni was performed with a particular setup: the array DALI2 coupled with eight large volume $LaBr_3$:Ce detectors (HECTOR+). DALI2 is an array composed by 186 NaI(Tl) scintillators for γ detection. It is an evolution of a previous array: DALI (Detector Array for Low Intensity radiation) realized in RIKEN for the old facility which provided only light exotic beams at $v/c \sim 0.3$. It consisted of 64 NaI(Tl) crystals 6 x 6 x 12 cm^3 surrounding the target and two sets of plastic scintillators, one placed at the top and the other at the bottom of the array. NaI(T) detectors were used to investigate γ-rays emitted by the target while the plastic scintillators were used

to avoid cosmic background [54]. Three types of NaI(Tl) detectors compose DALI2: 45 x 80 x 160 mm^3 and 40 x 80 x 160 mm^3 parallelepiped crystals were produced by SAINT-GOBAIN and SCIONIX while the other type (60 x 60 x 120 mm^3) was produced by BICRON. HAMAMATSU PMTs (model n^o R580) are coupled to these crystals, the former two types use 38 mm diameter PMTs while the last one 50 mm. Alluminium housing 1 mm thick is used for all the detectors, in addition the PMTs are surrounded by μ-metal. Fig. 3.32 shows the geometry of the DALI2 array. The detectors are placed on 12 layers,

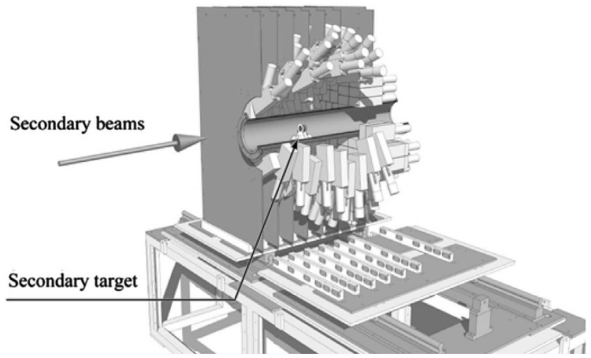

Figure 3.32: Schematic picture of DALI2 geaometry [5]

each of them holds up 6-14 detectors. The distance from the target and the positions of the crystals change layer by layer. The minimum distance from the target is 30 cm, corrisponding to detectors at 90^o, while the angular width of single crystals is around 6^o, (estimated for detectors at 60^o). Fig.3.33 shows the detectors position on different layers. The aim is to increase efficiency, taking into account the doppler boost for the typical beam velocity delivered by the facility ($\beta \sim 0.6$). The choice of NaI(Tl) detectors was the result of a compromise between intrinsic energy resolution, detection efficiency and costs. These detectors can provide 9% of energy resolution at 662 keV (^{137}Cs standard source). As regarding the electronics, the signal is shaped with 3 μs of time costant before being delivered to a peak-sensing analog-to-digital converter (CAEN V785 ADC). Time information is obtained by a time-to-digital converter (CAEN V1190 TDC) after a shaping of the signal with 100 ns of time costant and the processing made by a CFD. The large dimension of the array allows to cover an angular range from 15^o to 160^o: this means an angular coverage of almost 90%. This aspect is relevant for determination of the multipolarity of the radiation emitted from the target, this wide angular range allows to fix the angular momentum that characterizes the γ-rays detected. Fig. 3.34 shows the contributions to the energy resolution in the centre of mass frame at different angles, in

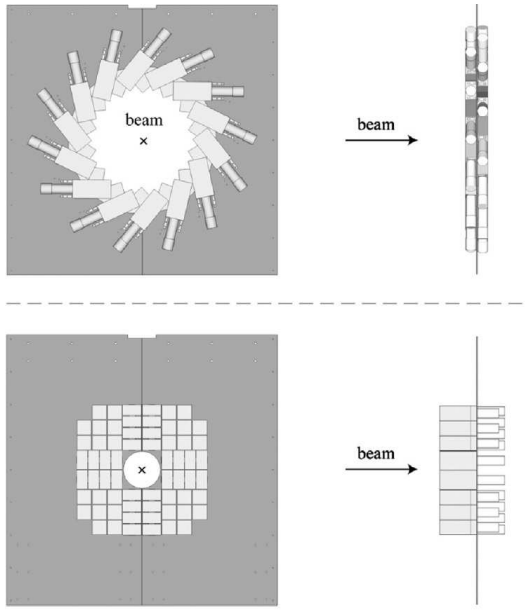

Figure 3.33: Top panel: geometry of 10^{th} and 11^{th} layers. Bottom panel: geometry of last layer (forward angles) [5]

the case of 1 MeV γ-rays emitted in flight at v/c of 0.6. It possible to see that the energy resolution remains around 10%. The performance for efficiency in this experimental condition is expected around 20% for 1 MeV γ-ray. The high granularity of this array allow to implement algorithms to increase efficiency and peak to total ratio. In particular add-back analysis is based on the hypotesis that the signals from neighbouring detectors are due to Compton scattering of one γ-ray. This means that summing these energies allows to reconstruct the energy of the incoming γ-ray. The angle for doppler correction is obtained by the angle of the detector with the highest energy release, because it is assumed to be the first one in which the γ ray interacts. This clustering algorithm allows to suppress Compton background, the key point is the estimation that the events in which two different γs interact in the same detectors cluster are fewer than the 20% of the all statistics. On the other hand, the operation of energy summing requires careful consideration related to the nonlinear response of the detectors. In the experiment discussed in this thesis DALI2 was coupled with LaBr detectors of HECTOR$^+$ array (described in 3.1.4). The organization in layers of DALI2 allows great flexibility: the forward layer was dismounted and it was replaced with a layer holding the eight LaBr detectors as shown in Fig. 3.35. The detectors were oriented at 30^o with a distance from the target of $\sim$ 34 cm.

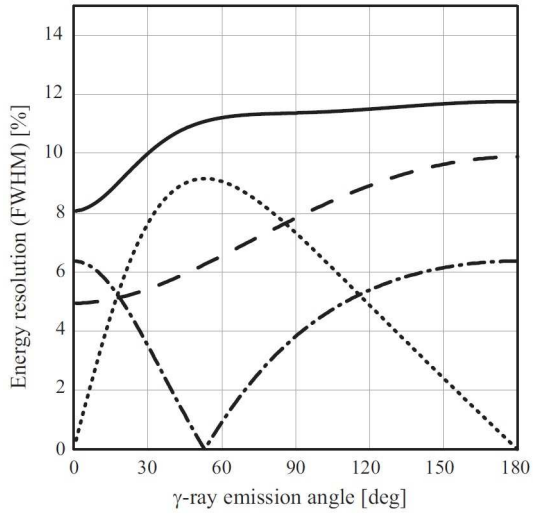

Figure 3.34: Expected energy resolution for 1 MeV γ-ray in center of mass frame at different angles (in laboratory). Here a β=0.6 is considered and the distance from the target is the nominal one of DALI (at least 30 cm). The diagram represents also all the contributions. Dashed curve, the intrinsic resolution; dotted curve, the finite opening angle of detectors; dash-dotted curve the spread in velocity of the source [5]

An additional LaBr detector (3" x 6") from RIKEN laboratories, was placed at 90^o.

3.2.4 The Data AcQuisition system

The RIBF Data AcQuisition is a distributed network system, based on the idea that the modularity of the DAQ reflects the interchangeability of the detector apparata in different setups. In fact, except for Big-RIPS, all the other detector systems can change from one experiment to the other. As shown in Fig.3.36, the DAQ is divided in blocks: every detector system has its own block and it can work as if it were in a stand-alone system. Every block has its own Event Builder, called Slave Event Builder. The system is equipped with CAMAC and VME data modules connected in parallel to the front-end computers. The data processing is ruled by a software package called "babirl DAQ": the Master Event builder receives data from the Slave Event Builders and constructs the whole event data. This arrangement of the DAQ system allows to reduce the dead time under 100 μs. The data are stored on a RAID system and are written in RIBF Data Format (RIDF). During the experiment here discussed, the master trigger required a coincidence of F7 plastic scintillator with F11 plastic scintillator and with a logic OR between: LaBr and DALI detectors. Three different triggers were used in the data analysis: F7 plastic

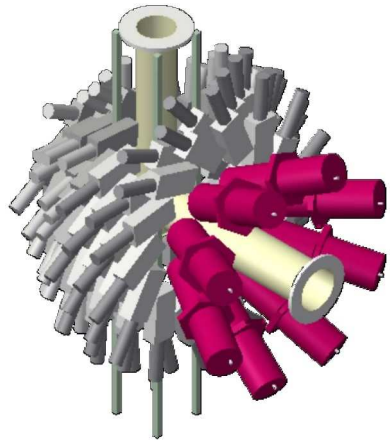

Figure 3.35: Diagram of the geometry of DALI2 coupled with LaBr detectors (HECTOR$^+$

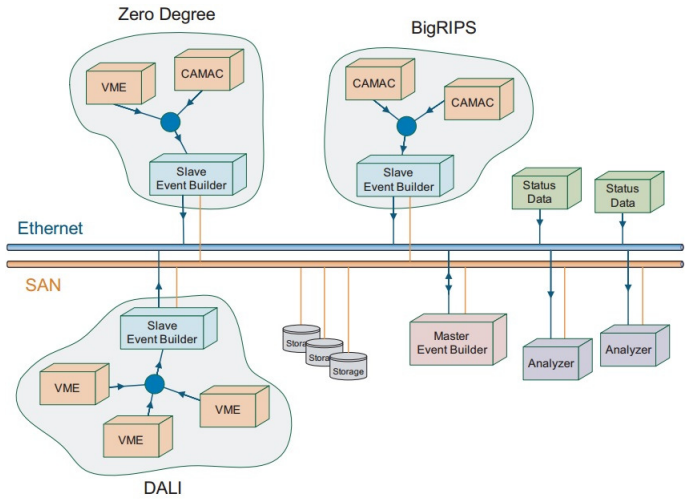

Figure 3.36: Scheme of RIBF DAQ. The boxes represents computers [56]

scintillator in stand alone mode (properly scaled down), F7 and F11 scintillators in coincidence with DALI and F7 and F11 scintillators in coincidence with HECTOR+. The time required for DAQ start was 1.2 μs and the acquisition was closed $\sim$500 ns after.
During this experiment new modules for analysis and conversion of the signal of LaBr were used. These modules, called QTC (Charge to Time Converter), are based on the observation that there is a relation between the height of the electric pulse and the width. These modules exploit the leading and trailing edge time of the signal to reconstruct the energy release. The timing information is provided by TDC V1190 modules. Even if in the present data analysis their informations were not used, they showed good perfor-

mances and they will be used also in future experiments.

CHAPTER 4

Data Analysis

The aim of this thesis is the investigation through Coulomb excitation of rare isotope nuclei. As shown in the previous chapter this has required a complex experimental setup for producing, identifying and selecting ions of interest and their reactions. An accurate data analysis needed to be developed in order to select "good" events and produce gamma ray spectra from the signals of the different detectors. In this chapter the processing and the conditions applied to the data is described for data from both the laboratories (GSI and RIKEN). In particular, the procedure to identify the ions of interest, the selection of coulomb excitation events and the gates and conditions applied to reduce background in gamma ray energy spectra will be explained. In conclusion of this chapter the final gated gamma ray energy spectra will be shown.

4.1 PreSPEC-AGATA data analysis: Identification and selection of the ions

4.1.1 Calibration of the detectors for identification

As explained in the previous chapter, identification of the ions incoming on the secondary target is performed with the FRS system. A lot of detectors are needed: TPCs, scintillators, ionization chambers. The signal of every detector has to be calibrated and tuned to have the correct identification.
As regarding A/Q estimation, both positions at focal planes and Time of Flight are needed. TPCs can provide high resolution position information, while the scintillators are characterized by a lower resolution.
TPCs signal can be calibrated using a fiber mask as position and spacing of the mask are known, it is possible to obtain a precise calibration (Fig. 4.1 shows an example).

The scintillator position signal can be calibrated using TPCs as reference.

Time of Flight calibration requires the primary beam: knowing the thickness of all the

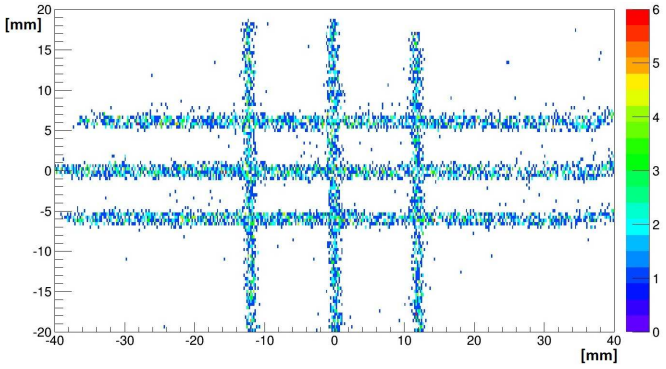

Figure 4.1: In the panel exemplum of the pattern used to calibrate TPCs position

materials on the beam line, it is possible, using the LISE calculator [72], to calculate the expected ToF and to compare it with the signal processed with TACs and TDCs.

A correct estimation of the ToF and therefore of the β value is very important for the MUSIC chambers. In fact, as shown previously, the estimation of the charge of the ions is dependant from both the ΔE measured by the ionization chamber, and from the velocity of the beam.

4.1.2 Commissioning with isomers

A commisioning run was focused to check that the FRS setup and the particle identification correctly worked. A ^{66}Cu ion beam was produced, selected and implanted in a plastic degrader at the seconary target stage.

This ion is produced in one isomeric state at E*=1154 keV with an half-life of 600 ns. Time of flight of ions to complete all the FRS beam line is of the order of some hundreds of nanoseconds: this means that most of the ions in the isomeric state decays after the implantation (Fig. 4.2 shows the scheme of the decay).

It is possible to select ions with FRS identification and using the AGATA array to check that the gamma ray spectrum shows the decay of this state.

The Z vs A/Q matrix (the FRS identification plot) obtained with FRS (Fig. 4.3) permits to clearly identify the incoming ions. The left panel of Fig. 4.4 represents the gamma ray spectrum obtained gating on ^{66}Cu ions while the right panel of the same figure shows

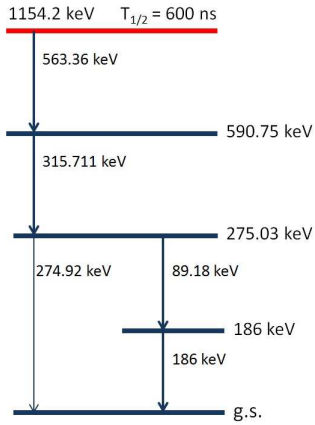

Figure 4.2: Gamma decay of isomer state of^{66}Cu

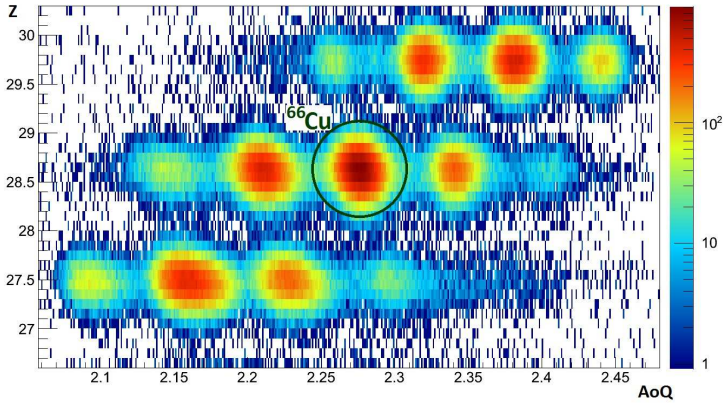

Figure 4.3: Identification plot of ions obtained with FRS: AoQ values are on the x-axes and Z values are on the on y-axes

the gamma ray spectrum related to ^{65}Cu (the neighbour bump in the ID matrix). It is clear that the peaks related to the isomer decay appears only selecting ^{66}Cu.

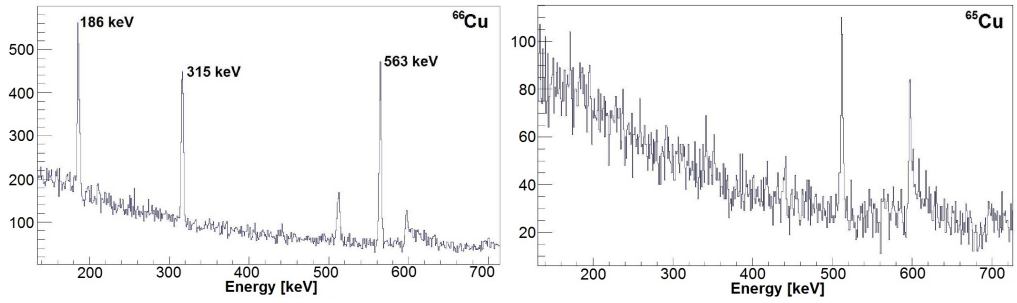

Figure 4.4: Left panel, gamma ray spectrum obtained gating on ^{66}Cu: it is possible to see the characteristic peaks related to isomeric decay of ^{66}Cu. The 86 keV transition is not shown because at this low energy the atomic background in the spectrum is too high. Right panel, gamma ray spectrum obtained gating on ^{65}Cu: none of the peaks of ^{66}Cu are present here (the two peaks in the figure are the 511 keV peak and the γ ray emission due to neutron capture from Ge nuclei in the detectors), showing the good identification and selection with FRS

4.1.3 Identification performance during Iron beamtime

In 2012 setup we measured ^{64}Fe from the fragmentation of a primary beam of ^{86}Kr at 730 AMeV on a $4g/cm^2$ thick ^{9}Be target with an intensity of $8 \cdot 10^9$ pps.
In 2014 the secondary ^{62}Fe beam was obtained with primary beam of ^{86}Kr at 700 AMeV on a $2.5g/cm^2$ ^{9}Be target and an intensity of $8 \cdot 10^8$ pps.
The setup for ^{62}Fe was affected by instabilities in SIS synchrotron: the intensity and the energy of the beam were not constant in time, as shown in Fig.4.5. This aspect required a fine tuning, run by run, for data analysis.
The setup for ^{64}Fe, was characterized by an high intensity secondary beam at S2 stage:

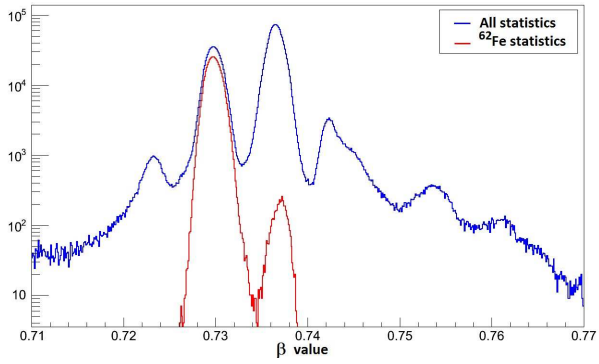

Figure 4.5: The profile of the β value distribution measured with FRS: in blue all the statistics acquired, in red only statistics related to ^{62}Fe

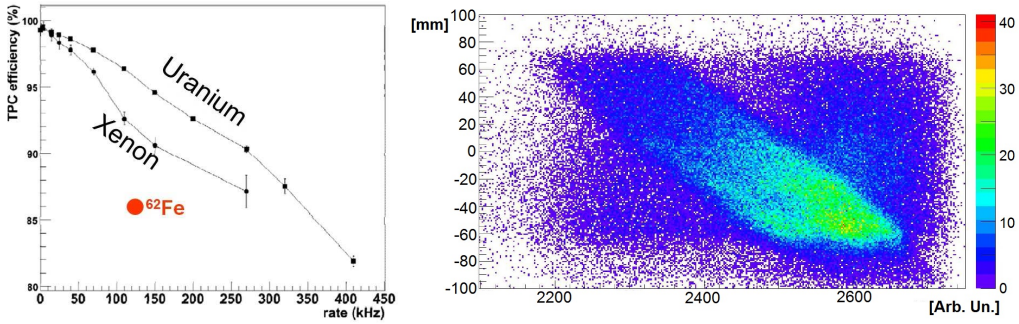

Figure 4.6: On left panel efficiency of TPC with different ions at varying the rate. On right panel, S2 standard scintillator position signal is plotted respect the position obtained with TPC, it is possible to see that the uncorrelated events are too many to obtain a good calibration

($\sim 5 \cdot 10^5$ Hz). This choice was based on the necessity to accumulate as much as possible statistics, considering that Finger detector can sustain such an high intensity. However high count rate affected TPC efficiency and standard S2 scintillator resolution.
The TPC efficiency to detect light ions is lower than that for heavy ions, in addition the detection efficiency decreases with the count rate as shown in the left panel of Fig. 4.6). The figure shows the performances of TPC for Uranium and Xenon beams compared with the efficiency that we got for ^{62}Fe at 10^5 Hz.
In 2012, for ^{64}Fe, the rate was five time larger than the one for ^{62}Fe. This had as a consequence a decrease of TPC detection efficiency of approximately 60%.
Also standard scintillator performance was affected by the rate. The right panel of Fig.4.6 shows the correlation between the S2 scintillator position signal and the position in TPCs. In standard experimental conditions this correlation would show a clean diagonal curve without any event outside to allow the calibration of the scintillator position signal. It is evident that in our case it is not possible to perform any precise calibration.
Another aspect that worsed the performances of the scintillators in the ^{64}Fe setup was the fact that an high intensity Pb beam was used in the experiment performed just before the ^{64}Fe one. This beam infact damaged the scintillators materials.
The offline analysis showed that the "Finger" detector was not operating correctly in 2012. It was changed for the measurement in 2014, but the instabilities of the new detector made it not working as expected, also during the ^{62}Fe runs. Therefore, no information from the finger detector was used and it was excluded from the analysis.
These experimental difficulties, reduced significantly the identification efficiency.
Both the measurements of ^{62,64}Fe were not performed in optimal conditions: in both

	2012	**2014**
Primary beam Intensity	$\sim 8 \cdot 10^9$ pps	$\sim 8 \cdot 10^8$ pps
S2 count rate	$\sim 5 \cdot 10^5$ Hz	$\sim 1.2 \cdot 10^5$ Hz
TPC detectors efficiency	60%	85%

Table 4.1: Intensity of the primary beam, count rate at S2 stage and TPC detector system efficiency in 2012 and 2014 setup.

cases the Finger scintillator could not to be used. In 2012 the TPC detectors were not operating in an optimal way and in 2014 the intensity and the energy of the primary beam were respectively smaller than expected and fluctuating.

4.1.4 Identification for Iron beams

The PreSPEC setup is designed to identify the components of the cocktail beam optimized for ^{64}Fe and ^{62}Fe. Figure 4.7 shows Z vs A/Q matrix for ^{64}Fe (top panel) and ^{62}Fe (bottom panel). The top panel shows higher background if compared with the matrix in the bottom panel. This is due to lower performances of ToF and ion tracking detectors described in the section 4.1.1 because of high rate and TPC degrader performances.
Charge states are not expected to be relevant for relativistic beams with low Z value [72], [73]. Through the evaluation of the energy loss in the degrader, an estimation of the charge state contribution to Iron statistics showed no events from charge states of heavier nuclei as expected.

In conclusion the FRS setting allowed to indentify and select the ions impinging on the secondary target with an efficiency of 85% for ^{62}Fe and 60% for ^{64}Fe (as reported in table 4.1). This selection in the data analysis was obtained with gates on the Z vs A/Q matrix: the red circles in Fig.4.7 represent the gates applied for the analysis.
The data analysis described in the next sections was performed after applying these gates on the beam incoming on the secondary target.

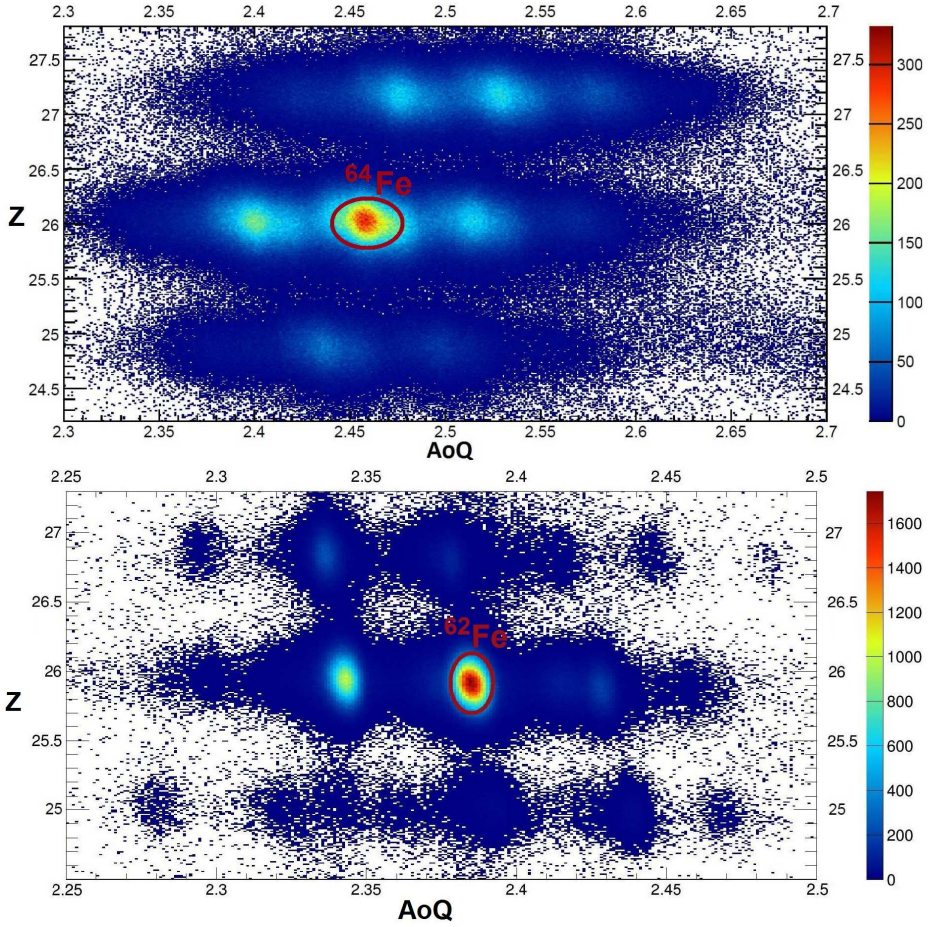

Figure 4.7: Upper panel: identification plot (A/Q value on x axes and Z value on y axes) obtained with FRS for ^{64}Fe with 2012 setup; the red circle represent the gate applied to select the ^{64}Fe events. Lower panel: identification plot (A/Q value on x axes and Z value on y axes) obtained with FRS for ^{62}Fe with the 2014 setup; the red circle represent the gate applied to select the ^{62}Fe events.

4.2 PreSPEC-AGATA data analysis: identification and selection of reaction products

4.2.1 calibration and identification

LYCCA calorimeter was used to identify and select the reaction products after the interaction of the secondary beam in the secondary target. All striped DSSSD detectors and CsI scintillator detectors were aligned (Fig. 4.8 and Fig. 4.9) before the calibration.

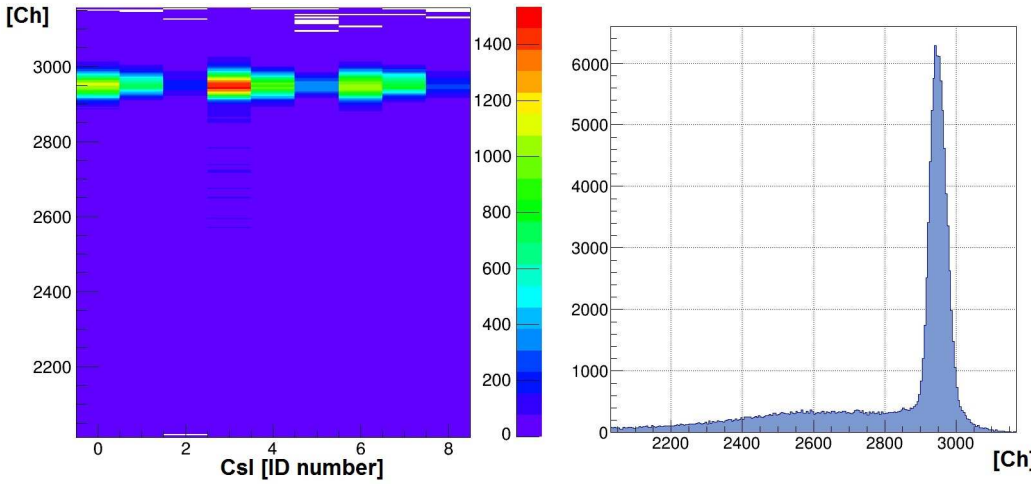

Figure 4.8: Exemplum of alignement of a cluster of 9 CsI detectors: on the left panel the raw aligned spectra for each detector is shown, on the right panel the superposition of all the aligned spectra are shown. The difference in statistics depends on the position of every detector with respect to the center of the beam line

The PMT signals for the ToF evaluation were aligned in time and corrected with respect to the position of interaction. In large scintillator membrane the signal of the PMT is affected by the time needed by the scintillation photons to travel from the interaction point of the beam to the PMT surface. It is important to correct this dependence with the hit position to achieve the best timing resolution (Fig.4.10).

	offset	**slope**
PMT 00	-519.36	0.008
PMT 01	-518.674	0.012
PMT 02	-517.64	0.008
PMT 03	-518.247	0.01
PMT 04	-516.729	0.0076
PMT 05	-516.458	0.009
PMT 06	-516.217	0.009
PMT 07	-515.637	0.007
PMT 08	-514.463	0.008
PMT 09	-514.422	0.008
PMT 10	-515.323	0.008
PMT 11	-515.647	0.009
PMT 12	-515.426	0.008
PMT 13	-515.9	0.007
PMT 14	-517.178	0.0076
PMT 15	-519.2	0.009
PMT 16	-515.894	0.008
PMT 17	-514.988	0.009
PMT 18	-514.887	0.007
PMT 19	-514.026	0.005
PMT 20	-513.975	0.009
PMT 21	-513.612	0.0097
PMT 22	-512.932	0.006
PMT 23	-513.632	0.008
PMT 24	-512.309	0.007
PMT 25	-512.096	0.007
PMT 26	-513.228	0.0116
PMT 27	-513.149	0.008
PMT 28	-512.821	0.008
PMT 29	-513.018	0.004
PMT 30	-514.394	0.007
PMT 31	0	0

Table 4.2: Exemplum of parameters to correct position dependece of PMT time signal

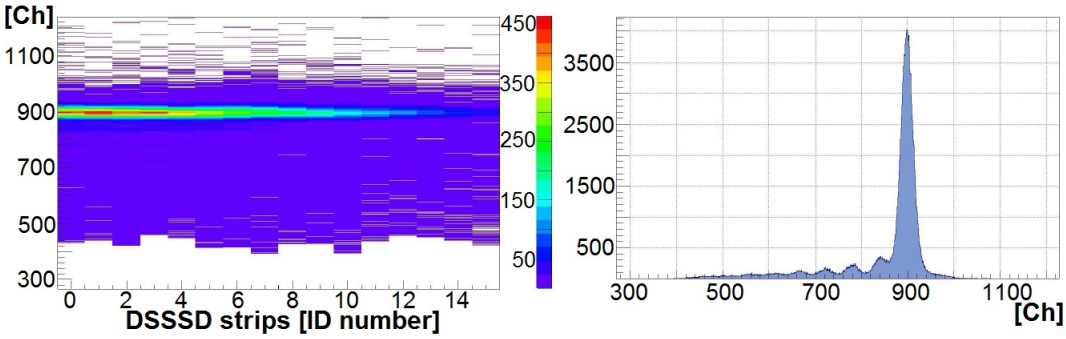

Figure 4.9: Exemplum of alignement of the strips af a DSSSD panel: on the left panel the raw aligned spectra for each strip, on the right panel the superposition of all the aligned spectra is shown.The difference in statistics depends on the position of every detector with respect to the beam line

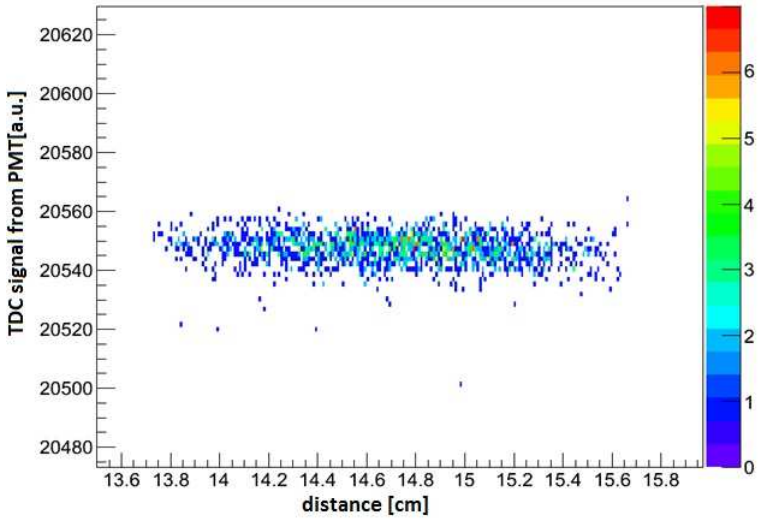

Figure 4.10: Exemplum of a corrected PMT signal.On y-axes the time corrected and on x-axes the distance in the plastic scintillator between the interaction point and PMT surface

The alignement and the calibration of the Wall detectors allowed to identify the reaction products with the E-ΔE matrix. In particular this allowed to select events in which the reaction product is the same as the incoming ion. This issue is extremely important in the data analysis as we needed to select projectiles which were excited and decayed without particle emission. Fig. 4.11 shows clearly the quasi-elastic bump, the red circle shows the gate applied for the selection of the projectile excitation events.

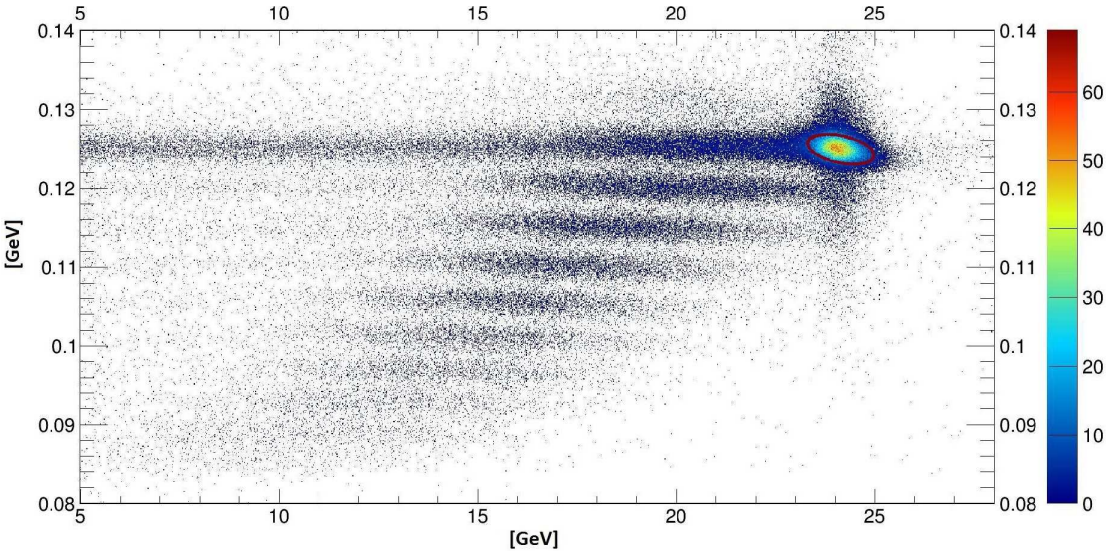

Figure 4.11: ΔE-E matrix: ΔE measured with DSSSD panels in the Wall, and E measured with CsI modules. It is possible to see clearly the quasi-elastic bump, related to events in which the outcoming ion is the same of incoming.

4.2.2 Test of consistency between FRS and LYCCA frames

The ToF evaluation with LYCCA scintillators is an important observable for a good estimation of the projectiles β values on the target. In fact the doppler correction for in-flight emitted γ rays requires a carefull estimation for both trajectory and velocity of the projectile.
Tests of consistency between FRS and LYCCA evaluation of ToF and ion tracks were performed.
The β value measured in FRS was compared with the β value measured in LYCCA (left panel of fig.4.12). As expected the fastest ions in FRS corresponds to the fastest ions in LYCCA, at least in average. The figure 4.12 shows this relation together with a considerable spread of the two distributions: this is probably due to the thickness of the materials that the beam has to pass through. Also the consistency in tracking ions is relevant for coulomb excitation events selection, because this selection is based on the scattering angle estimation. In fact, the scattering angle is related to the minimum impact parameter: if the minimum impact parameter is sufficiently large the probability of an excitation of the projectile due to the nuclear interaction with the target can be considered not significant with respect to the coulomb excitation (for more details see 4.2.3).

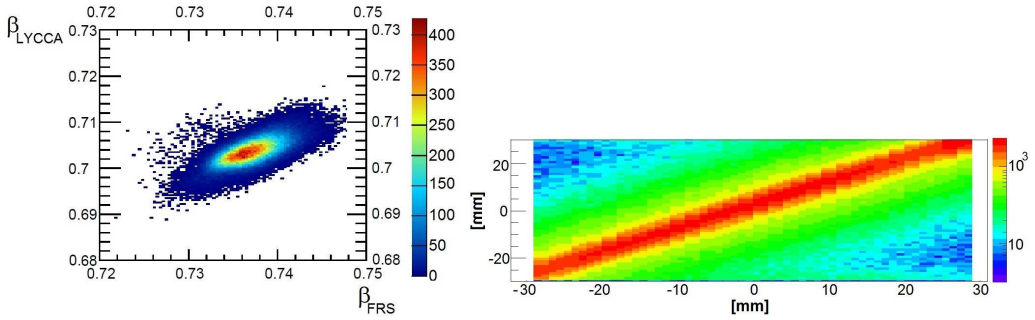

Figure 4.12: Left panel: comparison between estimation of the β value obtained with FRS and LYCCA. The width of the β value distribution in LYCCA is related to the thickness of the targets. Right panel: comparison between the position detected with DSSSD target and the position on DSSSD target obtained by TPCs interpolation.

In order to perform the angle evaluation, TPCs in S4 stage were used to estimate the trajectory of the ions incoming on the target, while DSSSD panels were used to track the ions outcoming from the target (Fig. 4.13 shows the patterns of the beam on the DSSSD target and Wall).

For this reason the position estimation with TPCs and the one obtained with DSSSDs before the target was compared to check the alignement of the two systems. This test showed that only a very small discrepancy of a few millimeters between TPCs and DSSSD. On the basis of this discrepancy it was possible to have an indication of the accuracy of the evaluation of the scattering angle. We obtained a maximum uncertainity in the determination of the scattering angle of less than 2 mrad.

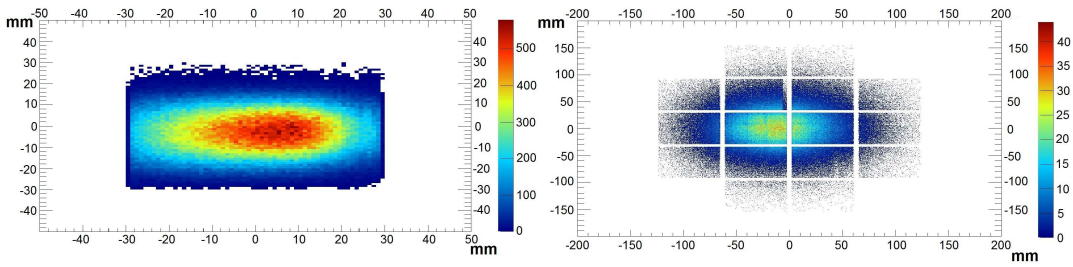

Figure 4.13: Left panel shows the beam pattern measured with the target DSSSD; right panel shows the beam pattern measured with Wall DSSSD.

4.2.3 Coulomb excitation selection

The next step of the data analysis, namely the γ ray spectra investigation (see section 4.3), was performed after the selection of scattering angle in order to select Coulomb excitation events.

The selection of the Coulomb excitation, in the target-projectile collision, is based on the consideration that if the minimum distance of approach is larger than the nuclear interaction range, the excitation of the projectile (or the target) occurs via electromagnetic interaction and not via nuclear interaction.

The minimum approach distance and the minimum impact parameter are connected by the relation:

$$b = \left(D^2 - \frac{2aD}{\gamma} \right)^{\frac{1}{2}} \tag{4.1}$$

where a is:

$$a = \frac{Z_T Z_P e^2}{m_0 c^2 \beta^2} \tag{4.2}$$

where m_0 is the reduced mass. It is possible to see from relation 4.1 that at relativistic energies $b_{min} \rightarrow D$, therefore in the next discussion they will be considered the same quantity.

The minimum distance between the target and the projectile to consider the excitation as a result of coulomb interaction, is commonly considered the sum of the nuclear radii of the target and the projectile.

Here, following the approach discussed in [84], this minimum distance is computed using the following relation:

$$R_{int} = C_p + C_t + 4.49 - \frac{C_p + C_t}{6.35}(fm) \tag{4.3}$$

where C_p and C_t are two parameters respectively related to projectile and target nucleus, that are obtained from:

$$C = R(1 - 1/R^2) \tag{4.4}$$

In this relation the projectile radius has to be used for C_p and target radius for C_t. The nuclear radii are obtained using the relation:

$$R = 1.28A^{1/3} - 0.76 + 0.8A^{-1/3} \tag{4.5}$$

As a result of this discussion, the coulomb excitation selection is based on the selection of the minimum distance approach. This distance is related to the scattering angle by

the relation explained in [83] and here reported:

$$\theta_{lab} = \frac{2.88 \times Z_t Z_p \times [931.5 + E_{lab}]}{A_p \times [E_{lab}^2 + 1863 \times E_{lab}]} \times \frac{1}{D}[rad] \tag{4.6}$$

where E_{lab} is the laboratory beam energy expressed in AMeV. The scattering angle selection is therefore the key point for selecting coulomb excitation events. In particular in the experiment here discussed the minimum distance for coulomb excitation events correspond to a maximum scattering angle of ~ 11 mrad (the so called, grazing angle).
As explained in the previous section, the experimental uncertainity on the scattering angle is of the order of 2 mrad: this has as a consequence that a gate on 11 mrad does not exclude events with larger scattering angle and therefore with smaller minimum distance approach between projectile and target.
For this reason a more strict condition has to be applied to the scattering angle. In the analysis a gate of 8 mrad was chosen. This value corresponds to a distribution of minimum distance peaked around 17.5 fm, but it ensures that a percentage lower than 10% of the total events are characterized by a minimum distance approach lower than the nuclear interaction range.
This choice of a selection of small scattering angle had as a consequence that only the ions hitting the two central DSSSD panels, where the statistics was mainly distributed, were considered. The very few statistics in the panels around could have increased more the background, including spurious ion trajectories, than the events we were interested in.
This section of the data analysis demonstrated that the PreSPEC setup was correctly tuned for coulomb excitation investigation at relativistic energies.
In conclusion, the analysis of the LYCCA array detectors allowed to define the gates on E-ΔE matrix to select the same projectile ^{62,64}Fe(see Fig. 4.11). In addition we use LYCCA to select the scattering angles lower than 8 mrad (see Fig. 4.14): this angle choice corresponds to consider coulomb scattering events with a minimum impact parameter of 17 fm(A more detailed discussion of the choice of this value will be presented in Chapter 5).
The next step of the data analysis: the γ ray spectra investigation, was performed after applying these two gates.

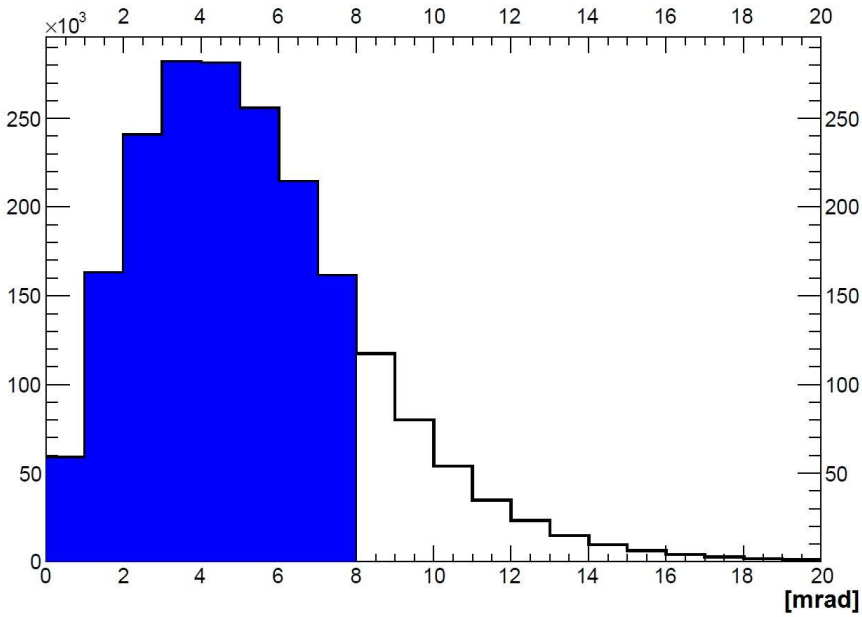

Figure 4.14: Angular scattering distribution in mrad of ions detected with forward Wall DSSSD panel. In blue the accepted angles.

4.3 PreSPEC-AGATA data analysis: Gamma ray detection

4.3.1 AGATA

Calibrations and settings

The AGATA data were "replayed" using Femul emulator and prespec code (for more details see App. C). The former was used, as a first step, to apply calibrations, alignements and PSA filter. The latter to merge AGATA data with MBS data that represent the data from all the other detector systems. The last step of AGATA data processing consisted in the application of the tracking algorithm. MGT libraries were used, after a fine tuning of the parameters and the threshold of the figure of merit.

Before the experimental campaign an high precise measurement of detector position was performed by J. Strachan et al. with a laser system. These positions were used as references for AGATA detectors. This required a geometrical transformation of the positions of AGATA crystal as implemeted in analysis codes available. In Fig. 4.15 the position of detectors as implemented in the code are represented in comparison with the measured positions (black crosses). A rotation of 7.5 degrees was needed to make crystal

positions in the code equal to the ones measured.

The γ-ray energy calibrations were performed using ^{60}Co and PuC sources. In the two

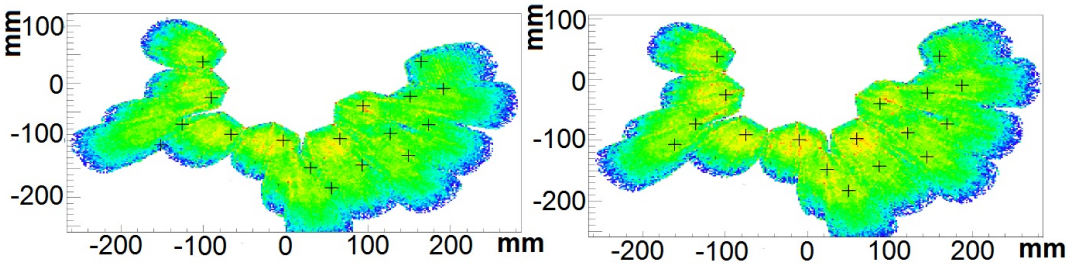

Figure 4.15: Left panel: the comparison between the position of crystal measured before the campaign(black crosses), and the position of crystal in the analysis code. Right panel: the same comparison after the rotation to correct the positions in the code

panels of Fig.4.16 the energy spectra from these two γ-ray sources are shown. The energy range required in the measurement spanned from 1 MeV till 15 MeV as not only PDR gamma decay need to be measured, but also the gamma decay from the first 2^+ of the exotic ions: the latter is important for the normalization needed to extract the strength of the PDR. References [51], [50] verified the linearity of AGATA on all the energy range of interest.

Energy resolution for the AGATA crystal was checked with calibration source: a value of FWHM < 3 keV was obtained for peaks at the energy of 1 MeV. Two crystals (12C and 14A) showed a worse energy resolution due to a larger contribution of noise in fact the increase in $\frac{\Delta E}{E}$ was not proportional to the energy but it remained approximately constant. For this reason these detectors were not excluded in the data analysis: in fact the doppler broadening expected was much higher than the HPGe detector intrinsic energy resolution.

The ion-γ time (here denoted as particle-γ time) was obtained as:

$$T_{P-G} = T_\gamma - T_{part} \tag{4.7}$$

Both time for gammas and ions were referred to the trigger of the acquisition. This signal was produced by the FPGA responsible of the coincidence and triggering of the system. Therefore particle-gamma time can be rewitten as [74]:

$$T_{P-G} = (T_\gamma - T_{trigger})_{Timestop} - (T_{part} - T_{trigger})_{Timestart} \tag{4.8}$$

T_{part} is obtained by the scintillator on the last FRS focal plane (SC41), while T_γ is ob-

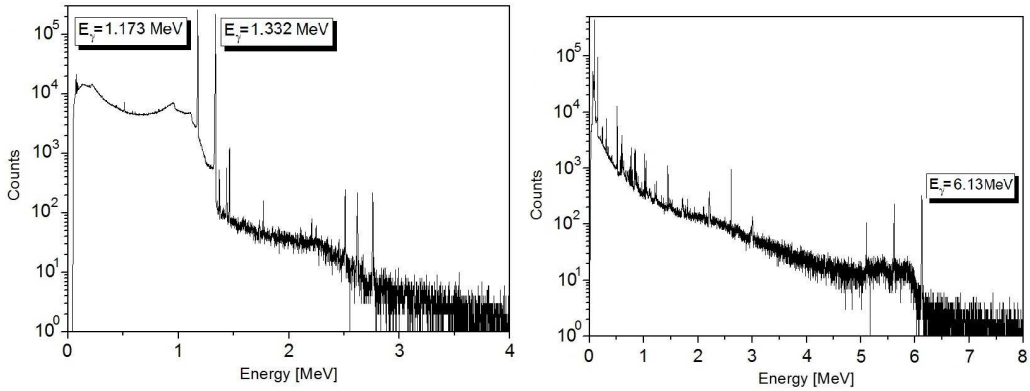

Figure 4.16: On left panel ^{60}Co source energy spectrum for calibration. On right panel PuC source energy spectrum for calibration: peaks at low energy are related to backround.

tained by the leading edge of the signal of HPGe detectors. For this reason the Energy-Time matrix of these detectors is characterized by a significant Time-Walk (left panel of Fig.4.17). It is possible to apply Time-Walk correction, in order to avoid this phenomenon (right panel of Fig.4.17).

In Fig.4.18 the time spectrum of one crystal was shown after the Time Walk correction and alignement to zero value. The time resolution of each crystal was estimated in the range from 16 to 30 ns. The timing resolution of all AGATA detector system was measured as 24 ns.

Time resolution, at fixed γ-ray energy, was measured after and before the Time Walk correction: a no significant difference in the two cases was obtained. For this reason, in the subsequent analysis, timing conditions were applied using proper cuts on Energy-Time matrix. This allowed to avoide the possibility of introducing some bias induced by the Time-Walk correction or by the alignement of timing of the crystals.

The doppler correction at high β values requires a precise determination of the angle between the projectile direction and the γ-ray emitted. As described in previous section ion tracks are recostructed using stripped silicon detectors (DSSSD), this provide a precision of the order of 1 mm. Gamma ray tracking algorithms provide the direction of γs detected by AGATA. The tracks are reconstructed using position determination obtained with PSA. The resolution in measuring the position is of the order of 5 mm. These consideration shows that the setup allows to get an high precise determination of the angle for doppler correction. It is important to have also the relative position of γ-detectors and ion tracking panels.

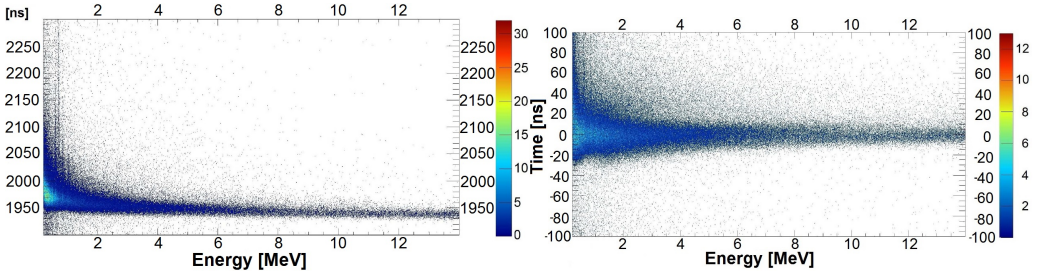

Figure 4.17: On left panel the Time-Energy Matrix, on y-axis time in ns and on x-axis energy in keV.On right panel the Time-Energy Matrix after the Time Walk correction and alignement

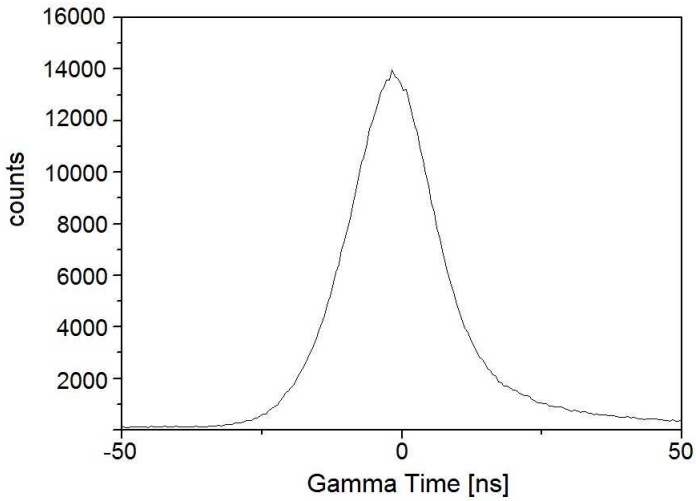

Figure 4.18: Time spectrum for an AGATA crystal after Time Walk correction and alignement. FWHM obtained : 17.8 ns

The relative position of the target with respect to the γ detectors was checked and fixed during the analysis of these data. It was found in fact that an offset of a few millimeters was needed.

The measurement and the simulation of the AGATA efficiency are described in App. B. A good agreement between the measurement and the simulation was obtained. The efficiency at 1 MeV of $\sim$3%, obtained by the source calibration runs, is in good agreement with the value published in the thechnical reports (3.25% at 1 MeV) [75].

Gates and filters

In order to obtain the spectrum of the gamma ray emitted in the interaction with the target, the conditions, explained below, on time and gamma ray tracking algorithms

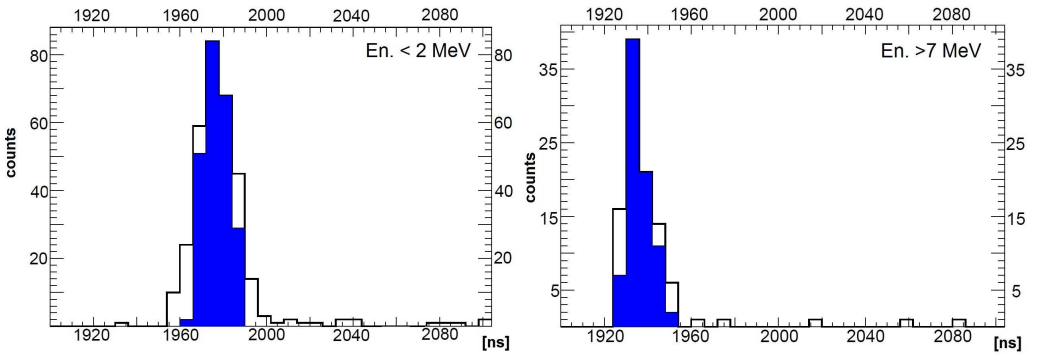

Figure 4.19: Left panel, time projection of Energy-Time gate at energy 0.5-2 MeV (ns on x-axis). Right panel, time projection of Energy-Time gate at energy 7-25 MeV (ns on x-axis)

were applied.
The gates on Energy vs Time matrix were applied for all the crystals to select prompt gammas from the target. In the two panels of Fig.4.19 the time spectra in two different energy range and the gates applied are represented. As displayed in the figure, the width of time gates is of the order of 20 ns; this is consistent with the FWHM of time peak dispalyed in Fig. 4.18.

Low energy gamma ray spectra were affected by a significant background contribution, coming probably from the target frame and from the materials around the target or along the beam line. For this reason, the gamma ray spectra in the region of 0.5 - 2 MeV were obtained applying MGT libraries for gamma ray tracking with a very restrictive condition on the figure of merit (see discussion in 3.1.3). In fact a Figure of Merit of 0.1 was required to accept the gamma ray reconstruction. In case of γ rays with E_γ >2 MeV the background resulted to be less intense and therefore less restrictive conditions on gamma recontruction were required. In addition a different tracking algorithm was used. The algorithm here applied reconstructed the energy of the gamma rays summing all the interaction points around the position of the most energetic release. This choice is due to an higher efficiency of gamma ray tracking in the range of 6 - 15 MeV [51] (25% or more than MGT tracking algorithm).

4.3.2 HECTOR$^+$

HECTOR$^+$ data, as anticipated before, were embedded in MBS system. In the data analysis, only the $LaBr_3$ spectra were considered and will be displayed as BaF_2 scintillators being at the backward angles, collected very low statistics,which indicates very low high

energy background from the target for our region of interes. The energy calibration was performed using the same calibration sources of the AGATA array. In Fig. 4.20 an exemplum of the spectrum measured with PuC source is plotted.

The intrinsic time resolution of LaBr detectors is 500 ps but once mounted in the experi-

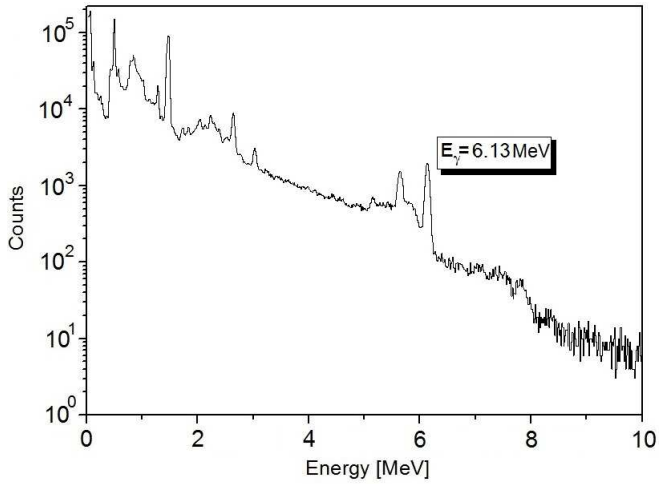

Figure 4.20: Energy calibration spectrum with PuC source.

ment it was estimated in the order of around 2 ns due to long cables of up to 35m needed to insert these detectors in the setup. In Fig.4.21 the time-energy matrix is displayed. It is possible to see a delayed structure around channel 820, approximately 20 ns later than the prompt peak which is at channel 800. This is a signature of a delayed background contribution: probably coming from the γ flash generated by the hit of the beam in LYCCA detectors.

The prompt peak at high energy is also more broadened than at low energy one, as it can be seen in Fig. 4.22, where the time spectra in the low and high energy range are plotted. The timing resolution at higher energy seems worsen but on the other hand the spectrum is more clean. In these two spectra the gates applied to obtain the γ ray spectra are shown: 2 ns and 3 ns time window gates were applied respectively in the low (Energy $<$ 4 MeV) and high energy range (Energy $>$ 4 MeV).

As explained in chapter 3, $LaBr_3$:Ce detectors are affected by the internal radiation. In the case of this large volume detectors, a rate of 1kHz is expected for the 1461 keV peak. Considering that at this energy the time window is 2 ns and statistics and triggers registered in these experiments, 13 counts per crystal are expected for the 2012 setup while only 8 counts for the 2014 setup. Therefore the background induced by internal

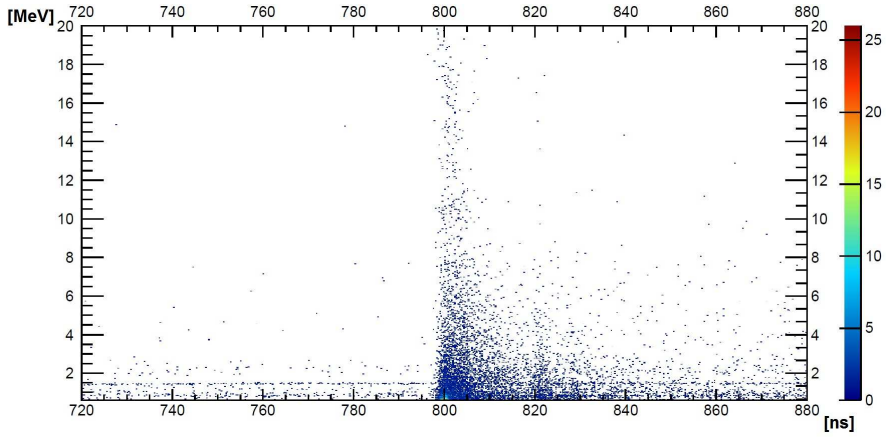

Figure 4.21: Time-Energy matrix for a LaBr detector. Energy in keVs on y axes and time in ns on x axes.

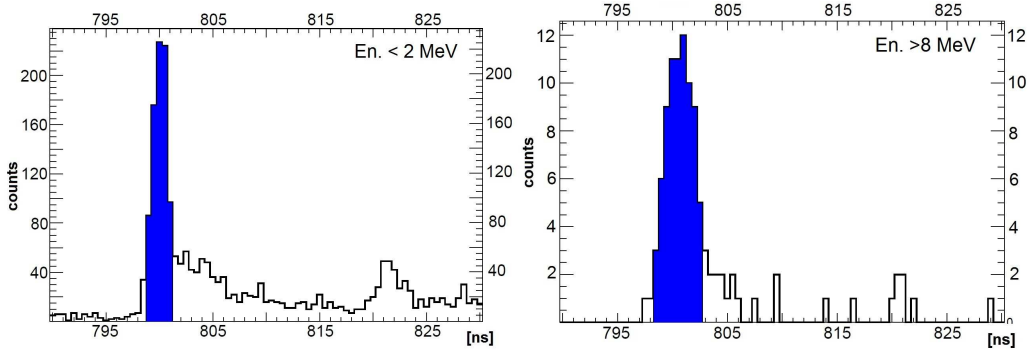

Figure 4.22: Left panel, time projection of Energy-Time gate at energy 0.5-2 MeV (ns on x-axis). Right panel, time projection of Energy-Time gate at energy 8-30 MeV (ns on x-axis)

radiation is negligible.

In conclusion this section showed that AGATA γ ray energy spectra were obtained after applying a time gate of the order of 20 ns, while the time window for LaBr was of the order of 2-3 ns. The limit of the Figure of Merit of tracking algorithms was fixed at 0.1 for the low energy range, because of the high level of the background. No conditions on multiplicity were applied: it was observed that the measurement was characterized by low multiplicity, infact after the gates, explained here and in the previous sections, the number of events with multiplicity higher than 2 was not significant, as shown in fig. 4.23.

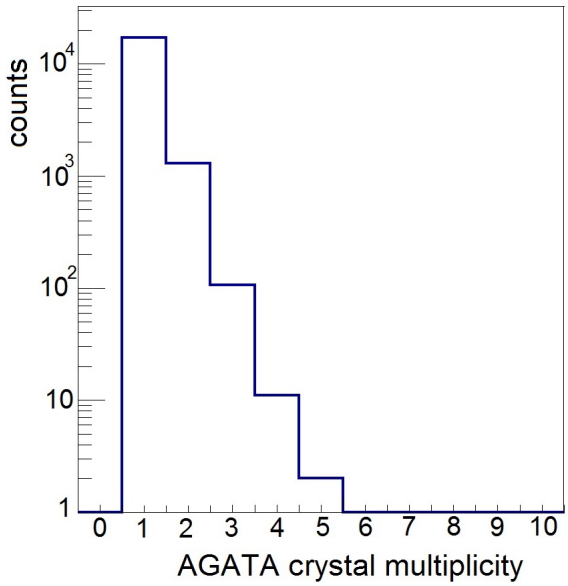

Figure 4.23: Multiplicity of AGATA crystals with the gates described in this and previous sections

4.4 PreSPEC-AGATA data analysis: Final Gamma ray spectra

The final AGATA and HECTOR energy spectra were obtained after applying all the gates listed in the previous sections. In particular AGATA and $LaBr_3$:Ce spectra were constructed using the following gates:

- Incident secondary beam of ^{64}Fe (or ^{62}Fe)
- After the secondary target outcoming beam of ^{64}Fe (or ^{62}Fe)
- Gate on scattering angle of the beam for Coulomb excitation selection
  For AGATA:
- Time gate of $\sim$20 ns on time γ-particle where S4 scintillator is the start and AGATA crystals the stop
- Tracking with MGT libraries using FoM < 0.1 (E_γ <2 MeV)
- Tracking with a bubble algorithm for E_γ >2 MeV
- doppler correction using event by event calculation of β
  For $LaBr_3$:Ce :
- Time gate of 3 ns for E_γ <4 MeV

- Time gate of 4 ns for E_γ >4 MeV
- doppler correction using event by event calculation of β

Fig. 4.24 and Fig.4.25 show the AGATA spectra in low and high energy range respectively. The low energy spectra show a peak at the energy of the first 2^+ state decay

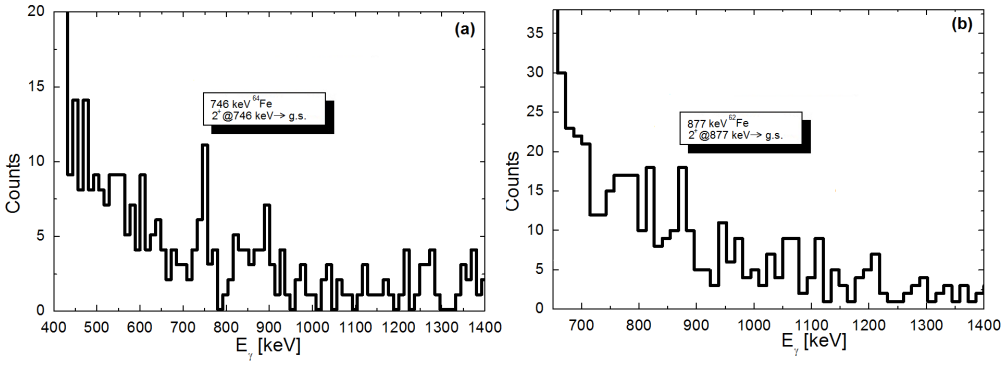

Figure 4.24: Panel a): the low energy spectrum measured with AGATA for ^{64}Fe coulomb excitation events.Panel b): the low energy spectrum measured with AGATA for ^{62}Fe coulomb excitation events.

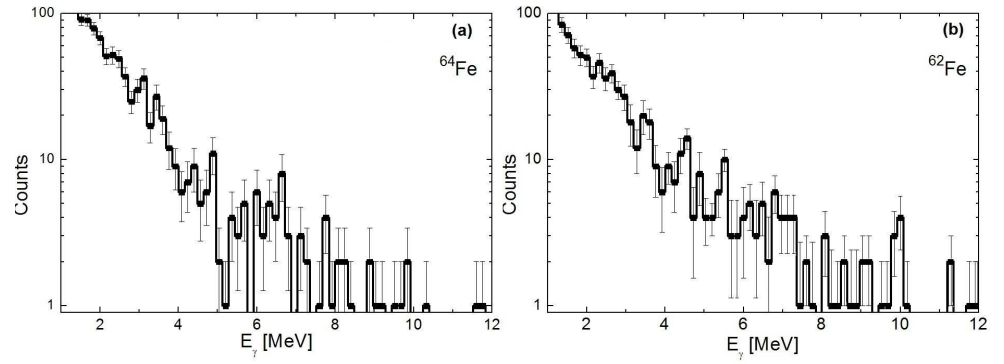

Figure 4.25: Panel a) the high energy spectrum measured with AGATA for ^{64}Fe coulomb excitation events. Panel b): the high energy spectrum measured with AGATA for ^{62}Fe coulomb excitation events.

for both projectiles. ^{64}Fe level scheme [76], shows a 2^+ state at 746 keV while the level scheme for ^{62}Fe [77], has a 2^+ state at 877 keV. This is an important point for the E1 measurement. Thanks to the fact that the B(E2) strength of the first 2^+ state decay for both of the ions is known, the statistics in the peaks related to this decay will provide the

normalization for the E1 cross section, essential to deduce B(E1) values for high energy measured strength.

High energy spectra produced by ^{64}Fe and ^{62}Fe show some structures in the energy range of 6-8 MeV. A simple argument to prove that these structures are neither statis-

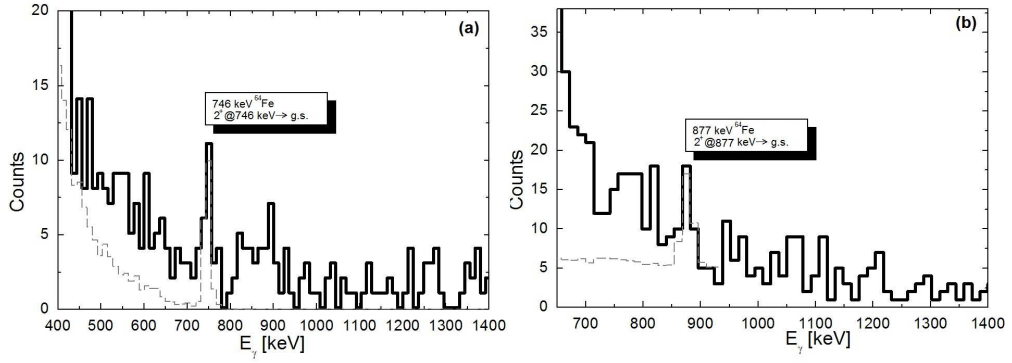

Figure 4.26: Panel a): the low energy spectrum (black) measured with AGATA for ^{64}Fe compared with a simulation (grey) of in-flight emission of 746 keV gammas. Panel b): the low energy spectrum (black) measured with AGATA for ^{62}Fe compared with a simulation GEANT montecarlo (grey) of in-flight emission of 877 keV gammas.

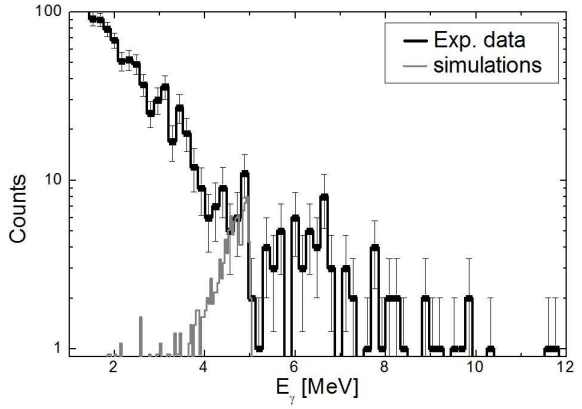

Figure 4.27: The high energy spectrum (black) measured with AGATA compared with a simulation (grey) of in-flight emission of 5 MeV gammas.

tical fluctuations of background nor generated by artifacts of the data analysis, is the comparison with simulations. A GEANT4 simulation (for more details see App. B), was performed to obtain the expected spectra of AGATA for this measurement. The emission from the projectile of γ-ray at energy 746 keV, 877 keV and 5 MeV was simulated. In Fig.

4.26 and 4.27 the comparison between the simulation and the experimental spectra is shown: the width and the line shape of the structures of interest at low and high energy are consistent with the expected ones from the simulations.
In the next chapter there will be a more detailed discussion about the statistics in the energy spectra, in particular in the range of 6 - 8 MeV.
The HECTOR$^+$ spectra have a too low statistics to allow the observation of the low energy 2^+ peak transition. In Fig. 4.28 the spectra for the two ions are plotted: only forward angle detectors are considered. This choice is due to the fact that the background contribution from target excitations is smaller at forward angle due to the lorentian relativistic boost. The reason of this difference in statistics respect to AGATA spectra is mainly connected to the smaller solid angles covered by $LaBr_3$ detectors with respect the AGATA array and the angular position of the detectors. In addition the worse energy resolution and the higher doppler broadening respect to AGATA crystals require higher statistics to make peak structures at high energy prevail on the background.

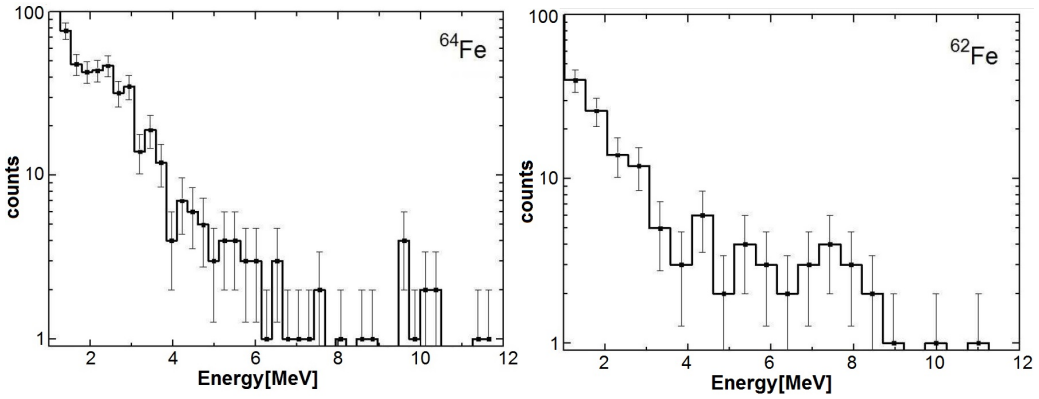

Figure 4.28: Left panel, the high energy spectra measured with LaBr at 68^o for ^{64}Fe coulomb excitation (LaBr at 22^o were missing in the setup); right panel, the high energy spectra measured with LaBr at 22^o for ^{62}Fe coulomb excitation.

4.5 DALI2-HECTOR+ data analysis: identification and selection of the ions

In Riken laboratory the identification and the selection of the radioactive ion beam is performed using the Big-Rips magnetic separator. As explained in the previous chapter, this identification is obtained by the estimation of the magnetic rigidity of the beam and the measurement of energy loss in the ion chambers. The Big-Rips team provides the calibration coefficients for all the detectors on the beam-line. These coefficients are determined for every experiment in order to take into account drifts in the gain of the detectors or changes in the settings. This allows to get high accurate Z vs A/Q plots. In Fig. 4.29 the Z vs AoQ plot for ^{70}Ni is shown, these are the equivalent of fig 4.7 obtained for GSI data the ions are very well separated, as a consequence the selection of ^{70}Ni events includes very low background as compared with GSI data.
The red circle in Fig. 4.29 shows the gate applied on this matrix to select the ions impinging on the secondary target: all the following data analysis was performed after applying this condition.

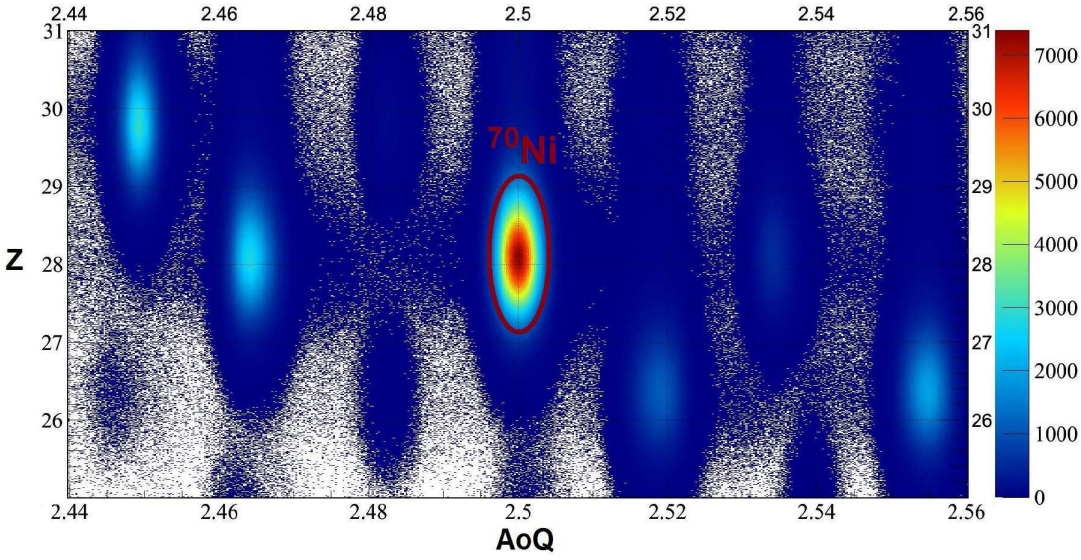

Figure 4.29: Identification plot obtained with Big-Rips magnetic separator: A/Q on x axes and Z on y axes. The ^{70}Ni bump is well separated and the most intense one. The red circle represents the gate on the matrix to select ^{70}Ni beam.

4.6 DALI2-HECTOR+ data analysis: Coulomb excitation events selection

The Zero Degree Spectrometer was used to select outcoming ions after the secondary target. As in Big-Rips, the identification is obtained measuring the magnetic rigidity of the ions. An accurate calibration of the detectors on the beam line is therefore needed: this was performed by the ZDS team at the beginning of the experiment. In fig.4.30 the Z vs A/Q plot is shown. As for the ions incoming on the secondary target, the bumps related to the ions are well separated, this means that also the selection is very clean, as represented in Fig.4.30 where the red circle represents the gate applied for outcoming ^{70}Ni, this is the equivalent of Fig. 4.11 for GSI data.
The scattering angle is measured using the PPACs before and after the target (detectors placed at F8 focal plane). The angular sensitivity is lower than in PreSPEC experiments: here the uncertainity is of the order of 5 mrad. In addition, the lower beam energy in comparison with GSI experiment, makes the angular straggling in the target more important. The consequence is that, in this case, it is not possible to select pure coulomb excitation events. For this reason the interpretation of γ ray spectra measured will consider both coulomb and nuclear interaction.
Fig. 4.31 shows the selection applied on the scattering angle, the gate accepts scattering angles smaller than 28 mrad that corresponds to an impact parameter of 13 fm.
In conclusion, Fig.4.30 and Fig.4.31 shows the gates applied to select mainly coulomb excitation events for ^{70}Ni, even if, as explained before excitations via nuclear interaction were not excluded; the data analysis of γ ray spectra was performed after having applied these gates.

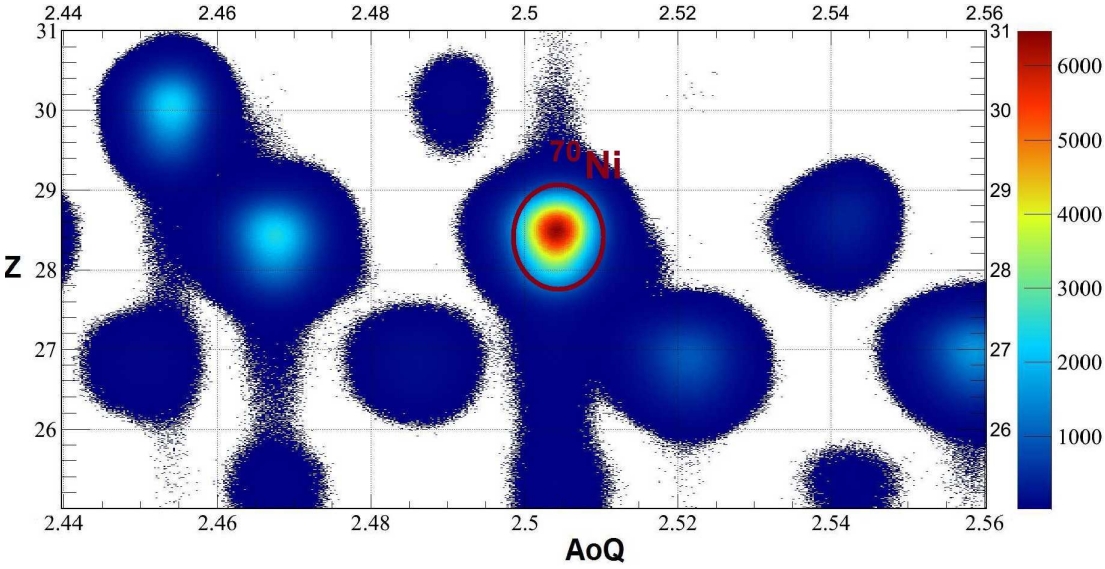

Figure 4.30: Identification plot obtained with the Zero Degree Spectrometer: A/Q on x axes and Z on y axes. The ^{70}Ni bump is well separated and the most intense one. The red circle represents the gate on ^{70}Ni.

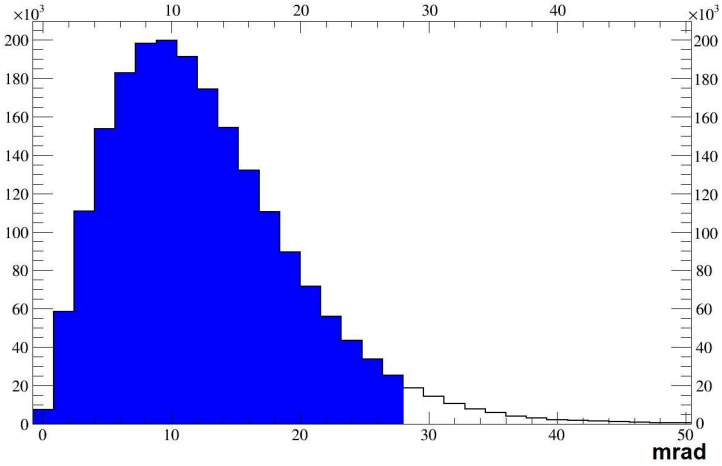

Figure 4.31: Scattering angle distribution. The filled area indicates the angles selected

4.7 DALI2-HECTOR+ data analysis: Gamma ray detection conditions

As explained in the previous chapter, the γ detection was performed with NaI and $LaBr_3$:Ce scintillator detectors. The energy calibration was performed using ^{60}Co,^{90}Y,^{137}Cs and Cm-C sources. It was important to have good calibration in both the high and low

energy range: as in GSI experiments, it is important to measure both first 2^+ state decay and the high γ-ray energy transitions. In order to avoid possible gain drifts in NaI scintillators during the measurements, the calibration runs were performed before and after the production runs. In Fig. 4.32 the matrix with all NaI scintillator calibrated spectra is shown, while in Fig. 4.33 a superimposition of LaBr spectra with calibration source is plotted. The particle-γ time was obtained by the difference between the time signal of

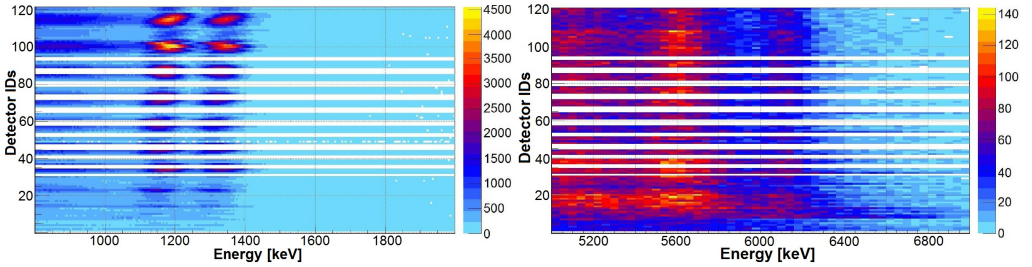

Figure 4.32: Left panel: matrix built with DALI2 detector energy spectra acquired with ^{60}Co source. Right panel: matrix built with DALI2 detector energy spectra acquired with Cm-C source.

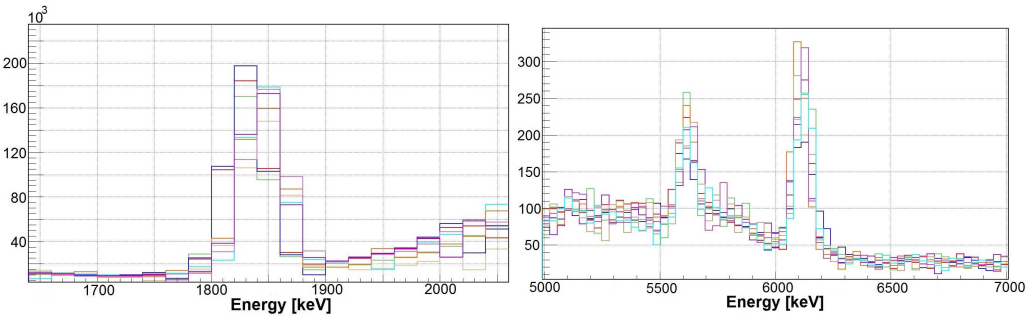

Figure 4.33: Left panel: LaBr energy spectra acquired with ^{88}Y source. Right panel: LaBr energy spectra acquired with Cm-C source.

DALI2 or $LaBr_3$:Ce scintillators and F8 plastic scintillator. The timing corresponding to γ signals was produced using a CFD (see Fig. 4.34). As shown in fig.4.35, the time gate applied for $LaBr_3$:Ce was of 4 ns while the time gate for NaI was of 5 ns. The $LaBr_3$ time resolution above 2 MeV was, as can be seen in figure 4.34 right panel, around 2ns.
Nevertheless a 4ns gate has been used in order to take also the low energy part inside the trigger.
Recently a preliminary review of the data reduction code of RIKEN is under development, but will not be fully debugged before mid 2016, where additional corrections on positions and ppacs pin down the timing resolution of the system, which means that the

overall time resolution of the LaBr scintillators are around 1.5ns.

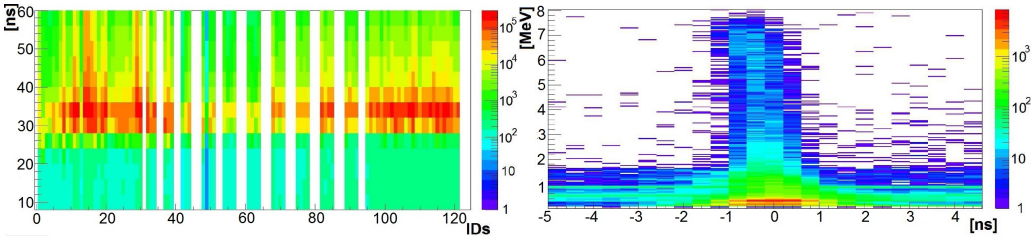

Figure 4.34: Left panel: DALI matrix with the timing spectra of all detectors. Right panel: exemplum of energy-time matrix for LaBr detectors.

As regarding the internal radioactivity, in this setup and with these time gates the expected counts related to the 1461 keV peak are of the order of 800 counts per crystal.

In order to obtain, as much as possible clean γ ray spectra, the time gates explained

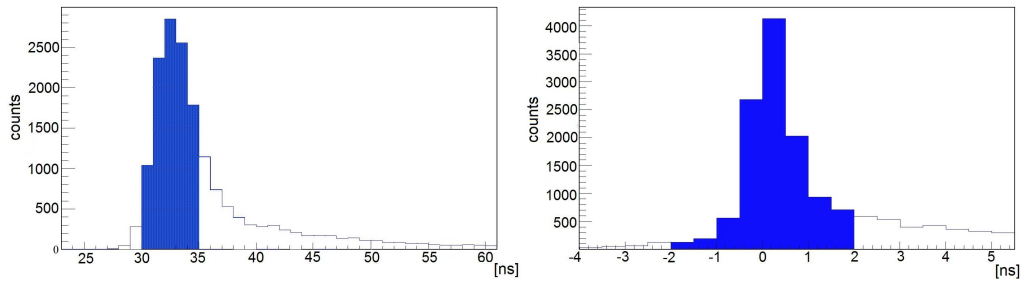

Figure 4.35: Left panel: NaI time spectrum, the filled area display the time gate applied. Right panel: $LaBr_3$ time spectrum, the filled area display the time gate applied

above and shown in Fig.4.35 were applied. In addition the energy spectrum measured out of the gate on the prompt peak was subtracted to the prompt energy spectrum , after an appropriate normalization. In this way not time correlated events were removed.
As in GSI experiment, the multiplicity of γ detected was low, for this reason no multiplicity gate was applied.

4.8 DALI2-HECTOR+ data analysis: Final spectra

Final γ ray spectra were obtained with a gate on impinging ion (^{70}NI) on the secondary target (see section 4.5), the gates on outgoing ^{70}Ni (see section 4.6) and on γ prompt time (described in section 4.7).
Fig. 4.36 shows the $LaBr_3$ spectrum at low energy: the peak corresponding to the energy

of the first 2^+ state decay [78] prevails clearly on the background.
Fig. 4.37 shows the energy spectra measured with DALI2 array at different angles: it is possible to see how the 2^+ state peak is not visible in backward detectors. This is due to the fact that the Lorentz boost makes the projectile γ emission focused at forward angles, as a consequence at backward angles the γ emission from the projectile is less intense. For this reason the spectrum of backward detectors mainly measure target γ emission or time correlated background.

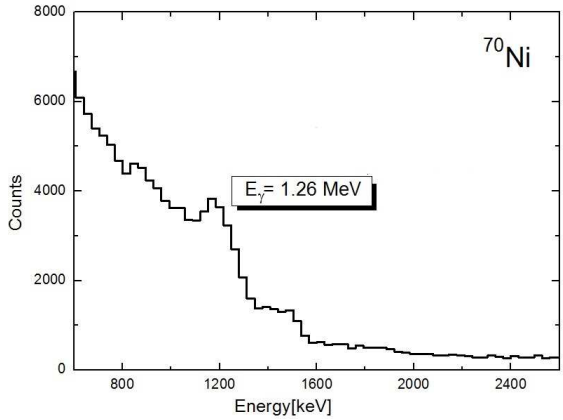

Figure 4.36: ^{70}Ni energy spectrum measured with LaBr detectors

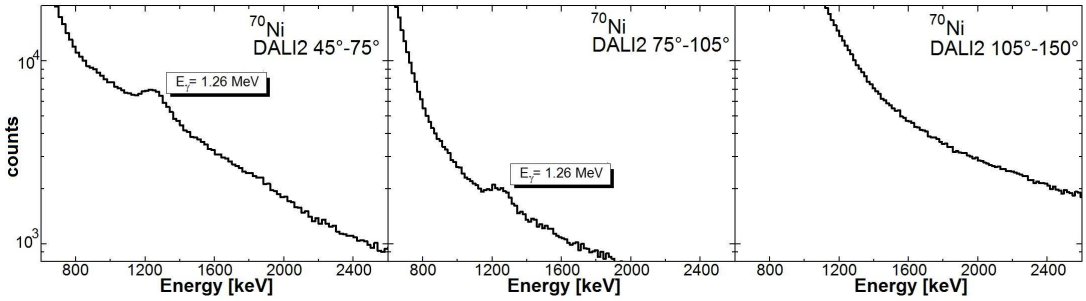

Figure 4.37: ^{70}Ni energy spectrum measured with DALI2 detectors: the left panel shows the energy spectrum measured by forward layer detectors (45^o-75^o); the central panel shows the spectrum measured by central layer detectors (75^o-105^o); the right panel the one measured by backward layer detectors (105^o-150^o)

Fig. 4.38 shows the high energy spectra measured with $LaBr_3$ detectors. The plot evidence an unresolved structure just below the particle threshold ($E_\gamma \sim 7.5$ MeV) and some structures above the threshold. In fig.4.39 the same structure below the particle threshold is visible in the spectrum of forward layers, backward layers spectrum does not show the same structures because of the less intense projectile emission.

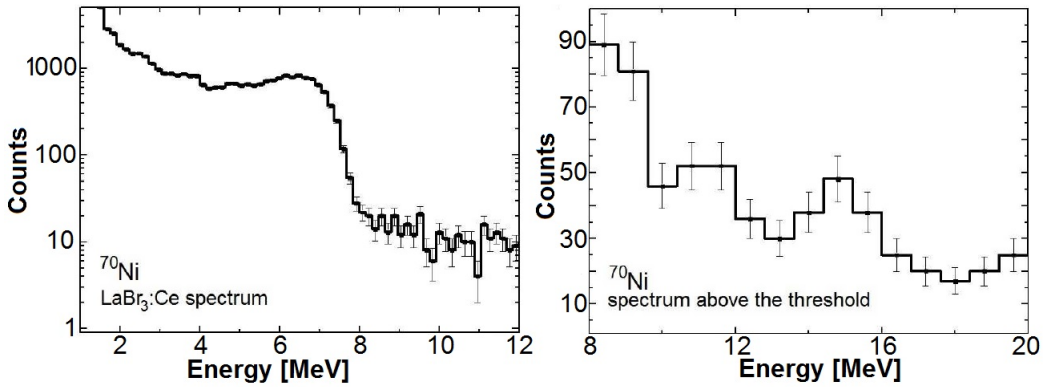

Figure 4.38: ^{70}Ni energy spectrum measured with $LaBr_3$:Ce detectors: the left panel shows the unresolved structure below the one particle separation energy (5-7 MeV); the right panel shows the structure above the threshold.

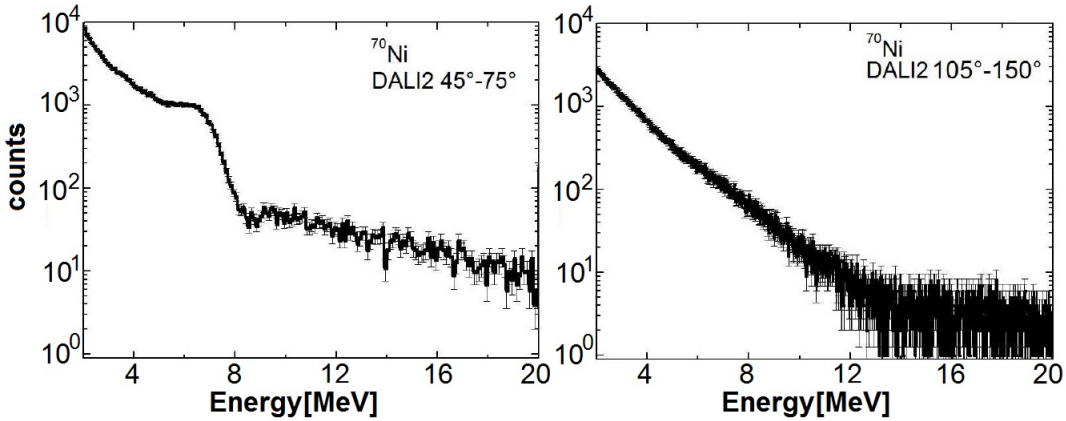

Figure 4.39: ^{70}Ni energy spectrum measured with DALI2 detectors: the left panel shows the spectrum in the high energy range measured by forward layer detectors (45^o-75^o);the right panel shows the spectrum in the high energy range measured by backward layer detectors (105^o-150^o)

CHAPTER 5

Discussion of experimental results

In this last chapter the experimental spectra obtained at the end of the previous chapter will be analyzed and discussed. In particular, the estimation of B(E1) values of γ-ray transition at energies just below one particle separation energy, will be discussed.

5.1 Beam correlated background evaluation

In GSI data analysis, two different approaches were combined to have an evaluation of background contribution in AGATA spectra in 6-12 MeV energy range (in the projectile frame). In one case we used $LaBr_3$ scintillators, in the other case AGATA spectrum itself was used.

Background evaluation with $LaBr_3$ scintillators

One of the advantages of PreSPEC setup described in the previous chapter, is the angular positions of high efficient scintillators. Energy spectra measured with backward detectors are mainly affected by beam correlated background contributions. As large volume scintillators have an efficiency higher than an AGATA crystal for high energy γ rays, it is possible to evaluate the background induced by the beam for γ energy between 10-20 MeV (in the laboratory frame), corresponding to 6-12 MeV in the projectile frame.
The estimation of background was done comparing the energy spectrum of the scintillators backward and forward angles. This analysis showed a flat and very weak contribution of the background in the energy region of interest (6-12 MeV in the projectile frame). The fig. 5.1 shows the shape of the $LaBr_3$ spectrum (after doppler correction) used to get the evaluation of the background. As already stated, it is very weak (few counts only). In the energy window 7-12 MeV it is flat and for energy larger than 12 MeV is negligible.

It was not possible to use the beam correlated background extracted from scintillators

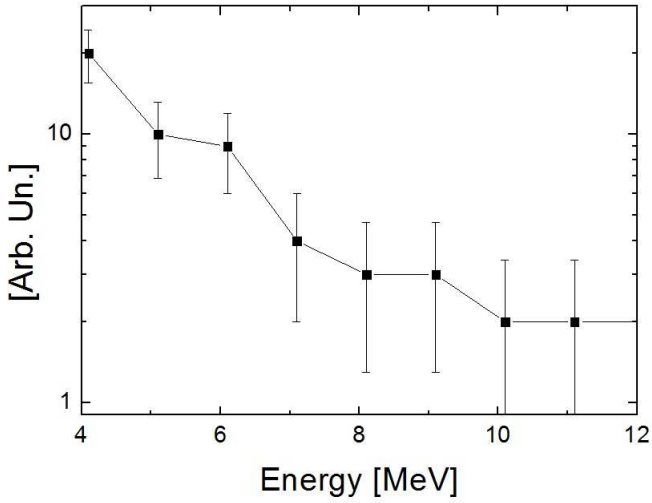

Figure 5.1: Shape of the energy spectrum from $LaBr_3$ scintillators after the application of the typical doppler correction in AGATA, to evaluate background contribution in energy region of interest

directly in AGATA spectra. In fact these detectors have different response function. Therefore the scintillator spectra were "transformed" in AGATA spectra using the response function obtained by simulations (for more details see App. B).
The statistics collected in the peak related to the de-excitation of the first 3^- level of lead target was used to normalize the response of the two detector systems: AGATA and $LaBr_3$:Ce array. The two panels of Fig. 5.2 show the energy spectrum measured with AGATA and with a $LaBr_3$ scintillator. The different energy resolution is evident, in terms of counts the statistics in the peak in the two spectra are comparable. This comparison had as a result a normalization factor of 1.5 between $LaBr_3$ and AGATA detectors.

Background evaluation with AGATA

The second approach used to get an evaluation of background is based on the hypothesis that counts at E_γ >15 MeV comes from background only. Therefore the evaluation of the beam correlated background in the energy range 6-12 MeV was obtained scaling for the array efficiency. Fig. 5.3 shows the beam correlated background level obtained with this approach. As in the case of the background evaluation performed using the scintillators, the background is structureless and very weak in the energy region of the one particle

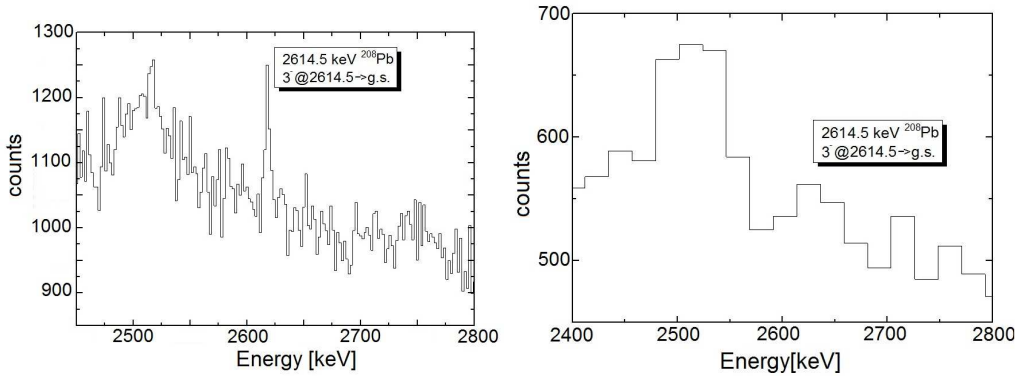

Figure 5.2: Left panel: exemplum of AGATA spectrum for 3^- level decay of ^{208}Pb. Right panel: exemplum of LaBr spectrum for 3^- level decay of ^{208}Pb.

separation energy (6-12 MeV).

The approach using the scintillators provided an higher background level than the one

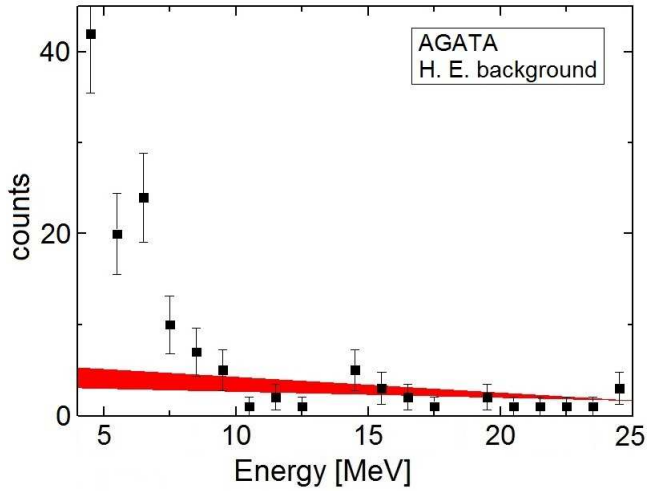

Figure 5.3: Energy spectrum measured with AGATA: the binning is equal to 1 MeV. The red line represents the background obtained with the statistics around 20 MeV. The thickness is related to the propagation of the statistical error in the high energy region.

obtained using AGATA statistics, almost twice bigger. The low level of the background makes the difference of result of these two approach not relevant. In the next step of the analysis the squared average of the backgroound level obtained with these two methods will be considered and subtracted to the AGATA spectrum.

5.2 Normalization of the cross section

The estimation of an absolute cross section represents the precise knowledge of dead-time, algorithm dependant efficiency, background sources, pile up events and so on.
For this reason it is a typical approach to rely on a known transition measured within the same experiment with exactly the same conditions.
The key point in this approach is the normalization factor between the reference known transition (in this case the decay from 2^+ state) and the unknown one (in this case the decay of the PDR).
As shown in the spectra 4.24, the setup allowed to measure the first 2^+ state decay for ^{62}Fe and ^{64}Fe.
In particular the statistics measured for these transitions was compared with the statistics expected considering the B(E2) values reported in literature (table 5.1): in the following paragraph a description of the approach used for this estimation is presented.
The B(E2) values used in this data analysis and adopted by NNDC database, are consistent with the measured values for ^{62}Fe ([81], [82]). The value adopted for ^{64}Fe is consistent with the experimental value measured via coulomb excitation in [81]. Another value is avaible in literature about B(E2) for this nucleus [82], but it is out of the systematics of neighbouring nuclei and we have decided not to consider it.
The cross section for 2^+ state excitation was computed using the relation [79]:

	Energy	**B(E2)**
^{64}Fe	746 keV	1780 e^{2}mb^2
^{62}Fe	877 keV	1028 e^{2}mb^2

Table 5.1: Energy and B(E2) values for the first 2^+ state peak for both the ions [80]

$$\sigma_{E2} = \frac{8\pi^2}{75}\frac{Z_T^2\alpha}{(\hbar c)^3}E_x^2 B(E2)\left(\frac{c}{v}\right)^4 \times \left[\frac{2}{\gamma^2}K_1^2 + \xi\left(1+\frac{1}{\gamma^2}\right)^2 K_0K_1 - \frac{v^4\xi^2}{2c^4}(K_1^2 - K_0^2)\right] \tag{5.1}$$

where K are modified bessel functions of the parameter $\xi = \frac{\omega_{fi}R}{\gamma v}$, with $E = \hbar\omega_{fi}$ is the excitation energy and R is the minimum distance, corresponding at minimum impact parameter in relativistic regime (in this data analysis R= 17.5 fm).
Using the well known experimental definition of cross-section and the gamma detection efficiency estimated with the simulations described in B, the number of gammas emitted

from the 2^+ state decay and detected by AGATA was estimated.

$$N_{expected} = \epsilon N_p N_T \sigma \tag{5.2}$$

where ϵ is the absolute detector efficiency, N_p the number of the projectiles and N_T the number of nuclei in the target. This value need to be corrected considering the angular distribution for the E2 emission due to the doppler boost. In fig. 5.4 a comparison between the spherical emission, the E1 and E2 emission after Lorentz boost is displayed. DWEIKO [93] code was used to get this evaluation.

The result of this procedure was compared with the statistics collected in the measured

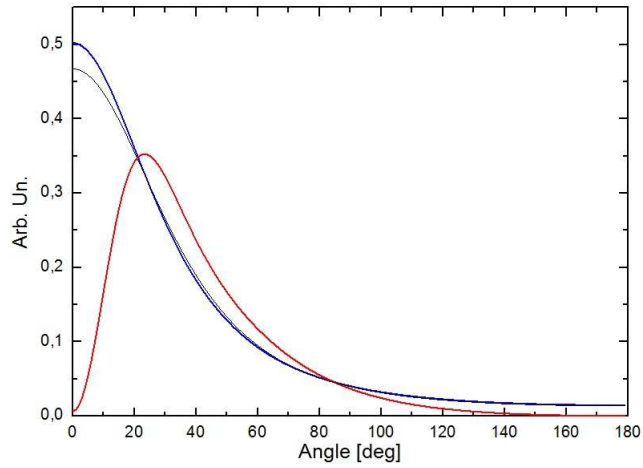

Figure 5.4: The angular distributions after Lorentz boost. Black line shows the angular distribution for spherical emission, the blue one for dipole emission and red one for quadrupole emission.

photopeak. The ratio provided the following normalization factors:

$N_{sc} = \frac{N_{measured}}{N_{expected}} = 0.5 \pm 0.1$ for ^{64}Fe

$N_{sc} = \frac{N_{measured}}{N_{expected}} = 0.55 \pm 0.1$ for ^{62}Fe

The factors summarize the effect of dead-time, background systematic errors, geometrical setup, non idealities. The two values are very similar, in fact the 2014 setup was tuned to be similar to the one used in 2012.

The error on this value was obtained considering the poisson error on the statistics collected for this transition and the uncertainty on the expected value, due to the experimental errors on the parameters used for this calculation.

5.3 Gamma yield contribution from GDR decay in pygmy energy region

We discuss here the γ yield contribution of GDR in the energy range of 6-10 MeV in order to compare it with the spectrum measured with AGATA. In next sections it will be shown that the experimental spectra have an amount of statistics higher than the one expected for the background and for the GDR γ decay. It is important to remember that the experimental conditions applied in the GSI data analysis described in the previous chapter select almost pure coulomb excitation events for ^{64,62}Fe.

As discussed in 4.2.3, the selection on scattering angle reduced the statistics related to nuclear excitation to a percentage lower than 10% of the amount of statistics considered in the last steps of the data analysis: therefore the contribution of nuclear excitation mechanism can be considered included in the error bars.

As explained in chapter 2, the coulomb interation at relativistic beam energy is dominated by dipole excitation. The energy spectrum of the virtual photons related to dipole interaction can be obtained by the relation:

$$N_{E1}(E_\gamma) = \frac{2Z^2\alpha}{\pi}(\frac{c}{v})^2 \left[\xi K_0 K_1 - \frac{v^2\xi^2}{2c^2}(K_1^2 - K_0^2)\right] \tag{5.3}$$

where $\xi = \frac{\omega D}{\gamma v}$.

This is an approximation of the relations described in 2.2.

The experimental conditions of the measurement here discussed (D=17.5 fm and $\beta \sim$ 0.71) provides an adiabatic cutoff in the range of 10-12 MeV. However the exponential tail of the distribution reaches the energies expected for GDR.

The electromagnetic excitation cross section can be obtained by the relation:

$$\sigma_C = \sum_{\pi\lambda} \sigma_C^{\pi\lambda} = \sum_{\pi\lambda} \int \frac{dE_\gamma}{E_\gamma} N_{\pi\lambda}(E_\gamma)\sigma_\gamma^{\pi\lambda}(E_\gamma) \tag{5.4}$$

where $\sigma_\gamma^{\pi\lambda}$ is the photoabsorption cross section for a parity π and angular momentum λ. In the case of GDR, it can be written as:

$$\sigma_{exc} = \int \frac{dE_\gamma}{E_\gamma} N_{E1}(E_\gamma)\sigma_{GDR}(E_\gamma) \tag{5.5}$$

where $\sigma_{GDR}(E_\gamma)$ is the GDR photoabsorption cross section. In the case of the Iron isotopes here discussed, no experimental values are available for the GDR photoabsorption cross section. For this reason the parameters from RIPL-3 database were used [87]. RIPL database expects a splitting of GDR as showed in the table below, it was supposed an

Z	A	El	Eta	E1[MeV]	W1[MeV]	E2[MeV]	W2[MeV]
26	64	Fe	1.161	16.80	4.96	19.27	8.42
26	62	Fe	1.161	16.95	4.78	19.45	7.89

Table 5.2: GDR parameters predicted by RIPL database. E1 and W1 are the centroid and the width of the first peak while E2 and W2 are thecentroid and the width of the second peak

equal amount of the strength for the two components. The strength related to GDR was estimated using the TRK sum rule, exposed in Chap. 1.
Therefore 5.5 can be used to obtain the excitation cross section for GDR.
The relation:

$$N_{exc} = N_p N_T \sigma_{exc} \tag{5.6}$$

shows that knowing the number of projectiles (N_P), the number of target nuclei (N_T) and the excitation cross section, it is possible to obtain the number of excitations expected in a measurement.
Fig. 5.5 shows the excitation cross section spectrum for ^{64}Fe analysis, the thick band is due to the variation of the excitation probability in relation to the spread in the minimum impact parameter.

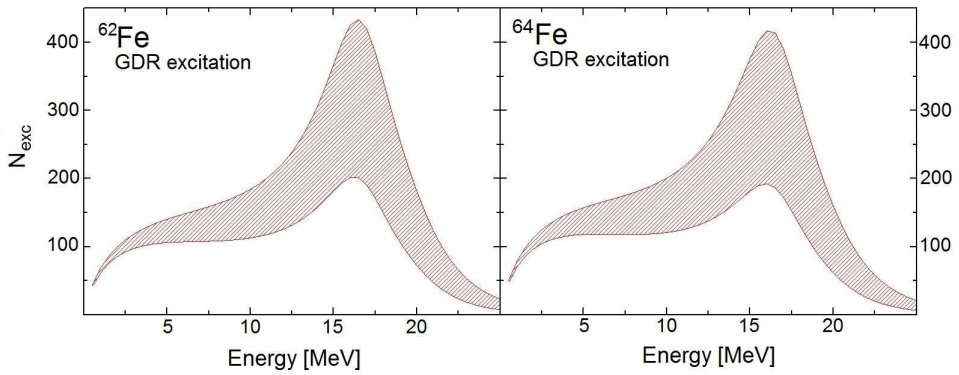

Figure 5.5: Energy excitation spectrum used as input of the GEMINI code for ^{62}Fe analysis (left panel) and ^{64}Fe analysis (right panel).The thick band is due to the variation of the excitation probability in relation to the spread in the minimum impact parameter.

The γ yield of GDR decay was evaluated using GEMINI code [86] , [85]. This code computes the statistical decay of an excitated Compound Nucleus, taking into account all the possible mechanisms of de-excitation. This code is more extensively explained in

App A.
The excitation spectrum showed in 5.5 was used as input for the code. The output of GEMINI for γ emission decay mechanism is shown in Fig. 5.6.
In order to compare this γ spectrum with the experimental one, it was folded with the AGATA response function.
In fig.5.6 the spectra in C.M. system obtained as output of GEMINI for ^{62}Fe and ^{64}Fe analysis are shown. In fig.5.7 the same spectra of Fig.5.6 but folded with AGATA response function are shown.
Using the same technique, also target excitation yield was evaluated. In this case the

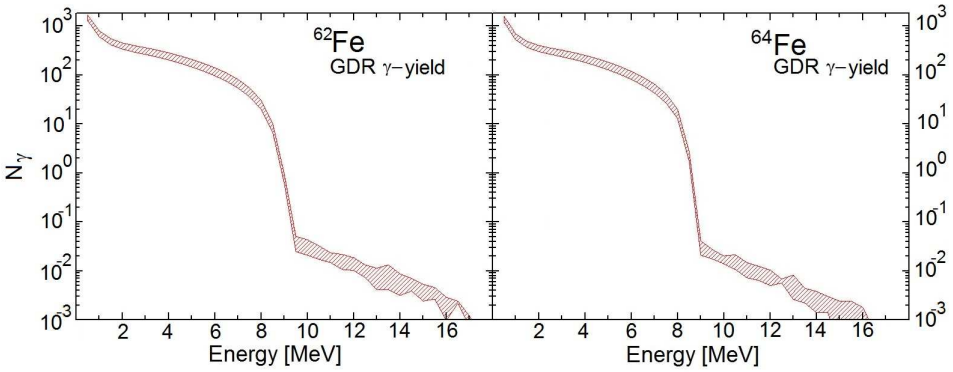

Figure 5.6: GEMINI output γ spectrum for ^{62}Fe (left panel) and for ^{64}Fe (right panel).

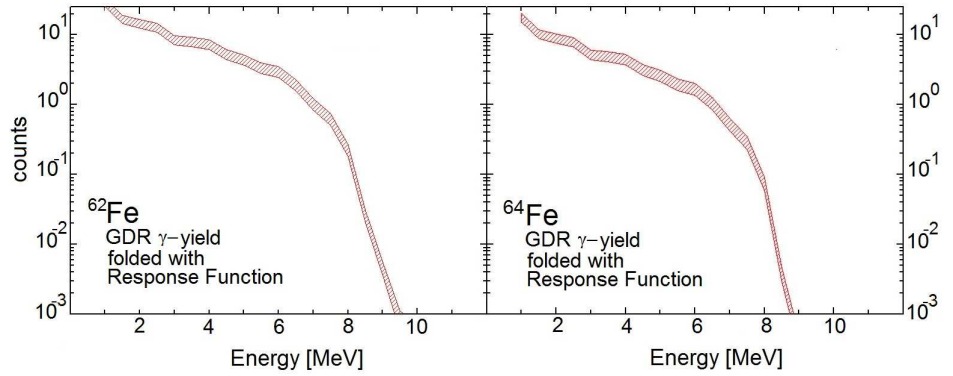

Figure 5.7: γ yield for ^{62}Fe analysis of the experimental spectrum(left panel) and for ^{64}Fe analysis of the experimental spectrum(right panel).

RIPL database provided experimental values for the GDR parameters (see table 5.3). Also here the emission spectrum was folded with AGATA response function, in addition

Z	A	El	E1[MeV]	CS1[mb]	W1[MeV]
82	208	Pb	13.63	643.7	3.93
79	197	Au	13.73	501.1	4.74

Table 5.3: Experimental parameters for GDR in ^{208}Pb [88] and in ^{197}Au [89].

(even if wrong) the doppler shift relative to the projectile was applied in order to compare the spectrum with the experimental one: in this case infact the emmission source is at rest respect the detectors.
The γ yield from GDR decay of the projectile was summed to the one of the target to obtain the yield on the all energy spectrum, see Fig. 5.8.

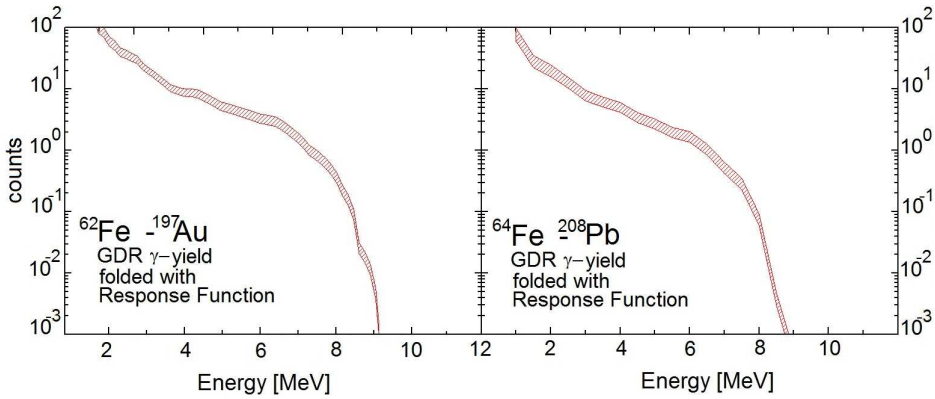

Figure 5.8: γ yield from GDR decay of the projectile and the target for ^{62}Fe analysis (left panel) and for ^{64}Fe analysis (right panel)

5.4 Spectra subtracted and multipolarity investigation

Fig. 5.9 shows the experimental spectra for both Iron isotopes compared with the γ yield (red line) coming from GDR decay and background. The thickness of the red line represents the uncertainity due to statistical and experimental error bars. These reported spectra clearly show an amount of statistics higher than background namely related to the tail of the GDR.

The subtracted spectra in fig. 5.10 show the structures remaining after the subtraction of the background and GDR γ yield. These structures were considered as the decay of E1 excitations. The reaction mechanism used in these experiments, explained in chapter 2, selects practically only dipole excitation.

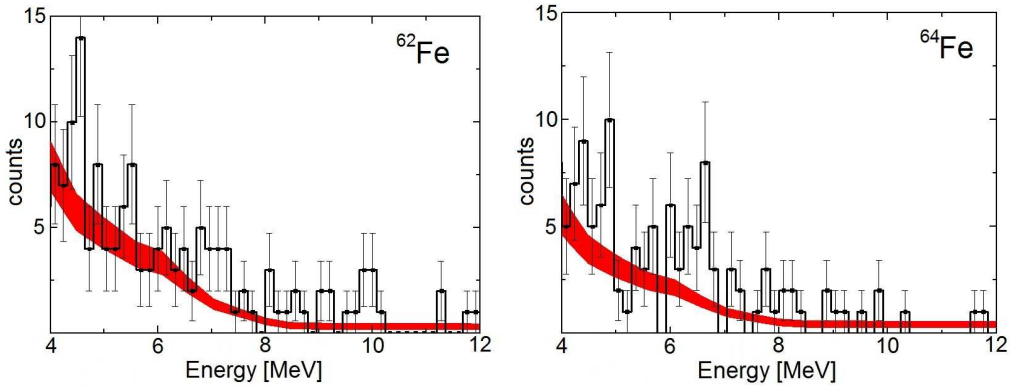

Figure 5.9: AGATA energy spectrum compared with the γ yield from GDR decay and background for ^{62}Fe analysis(left panel) and for ^{64}Fe analysis(right panel).

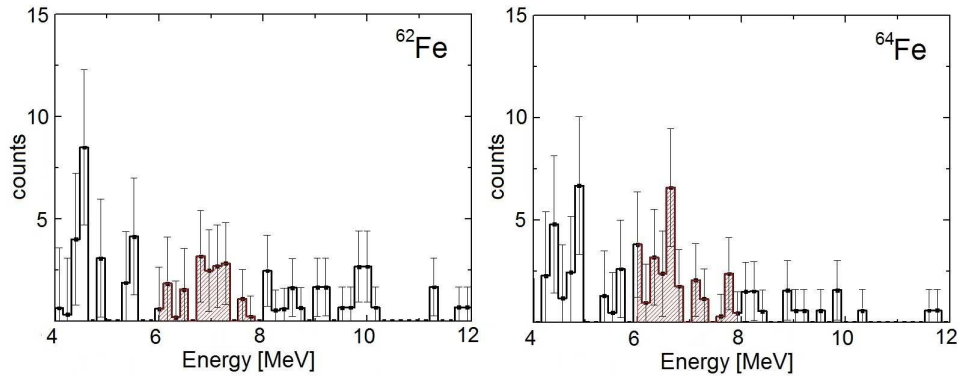

Figure 5.10: AGATA energy spectrum after the subtraction of the γ yield from GDR decay and background for ^{62}Fe analysis(left panel) and for ^{64}Fe analysis(right panel). In both figures the energy range that will be considered for the estimation of B(E1) values is underlined by a red shadow.

In fig.5.11 the cross sections related to E1 and E2 excitations in 6-10 MeV energy range are shown at different beam energies, the B(E1) and B(E2) values used for this calculation are taken from [90], [91] . It is clear that the cross section related to E1 transitions is predominant respect to the one related to E2 transitions.

Though the statistics was very low, an angular investigation was performed. For this reason, an incremental angular distribution was considered. This means that at every angle, all the statistics from 0 rad till the value considered was summed.

Fig.5.12 shows the ratio of the incremental angular distribution between the first 2^+ decay peak and the statistics in 5-8 MeV range. The experimental points are compared with

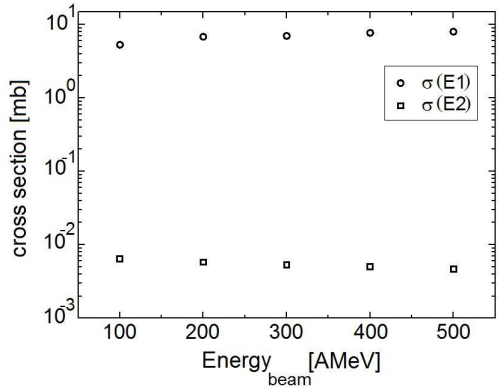

Figure 5.11: Circle points represent the cross section for an E1 transition in the experimental setting here used, while squared points represent the cross section for an E2 transition.

the expected trend obtained folding the E1 and E2 distribution plotted in fig. 5.4 and the AGATA response function. As comparison, the same cumulative angular distribution is plotted for the ratio of the 2^+ state decays of the two ions.
It is possible to see that the distributions in the two conditions have a different trend. If we consider just these two diagrams by their own this is not a sufficient proof to assign the multipolarity of the high energy statistics. Anyway they clearly show that the cumulative angular distribution is different in the two cases, this is a strong indication that the high energy statistics cannot be assign completely to E2 transition. Nevertheless, these diagrams coupled with the previous consideration about the cross section, provide a very clear indication that the structures in the subtracted spectra are related to E1 transitions.

In conclusion, it was shown that an amount of statistics between 6 and 8 MeV remains in the spectra after the background subtraction (Fig. 5.10). This spectrum was obtained after the selection of an incoming and outcoming ^{62,64}Fe beam, in addition coulomb excitation mechanism was selected. The coulomb excitation at relativistic beam energy selects dipole excitation: infact the comparison of the angular distribution of this high energy statistics with the angular distribution of the first 2^+ state decay, showed that the multipolarity is different from E2.

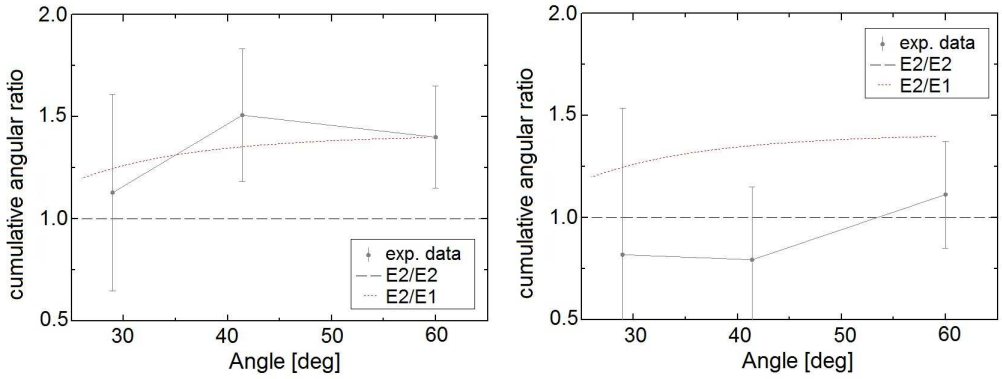

Figure 5.12: Left panel: ratio between the cumulative angular distribution associated to the 2^+ decay events and the one in the range 5-8 MeV, compared with the expected trend for the E2/E1 and E2/E2 ratio. The expected trend were obtained considering the experimental setup. Right panel: cumulative angular distribution for the ratio between the cumulative angular distribution associated to the 2^+ decay events in ^{64}Fe and in ^{62}Fe, compared with the expected trend for the E2/E1 and E2/E2 ratio.

5.5 E1 investigation in ^{70}Ni isotope

A procedure similar to the one used to investigate the E1 strength in GSI was applied for ^{70}Ni.

The cross-section normalization factor was not obtained by the 2^+ decay level because there is a significant disagreement in the values already in literature between measurements and theory for ^{70}Ni and between the different thoretical results in ^{72}Ni [95]. For this reason and considering the high statistics here collected, the absolute peak strength determinated in this work will be used in the following data analysis to get an estimation of its B(E2) value.

The cross-section normalization factor was therefore obtained in another experiment (about pygmy in Oxigen ions) with the same setup [94]. The value used in this analysis was equal to 0.9.

As introduced in the previous chapter, the uncertainty on the precise scattering angle measurement makes the contribution of nuclar excitation events relevant in this data analysis.

According to Reference [96], the nuclear contribution in this measurement is rather small, namely 20% of the events.

In the following discussion the statistics selected with the gates described in the previ-

Z	A	El	Eta	E1[MeV]	W1[MeV]	E2[MeV]	W2[MeV]
28	70	Ni	1.	18.02	6.73	18.02	6.73

Table 5.4: GDR parameters predicted by RIPL database. E1 and W1 are the centroid and the width of the first peak while E2 and W2 are thecentroid and the width of the second peak

ous chapter 4 is considered as if it were only related to the coulomb excitation.
In ^{70}Ni data analysis GDR excitation and decay were obtained in the same way described in 5.3. In the left panel of fig. 5.13 the obtained excitation probability is plotted.
This spectrum was used as input in GEMINI++ code. The expected γ decay spectrum is displayed in right panel of fig. 5.13 (also in this case the RIPL-3 parameters were used). As in the data analysis of Iron isotopes the GEMINI output was folded with the detector Response Function.
In this case it was obtained with the SUNFLOWER simulation code (see appendix B), and the efficiency obtained was compared with the one published in literature [58], [97], showing a good agreement.

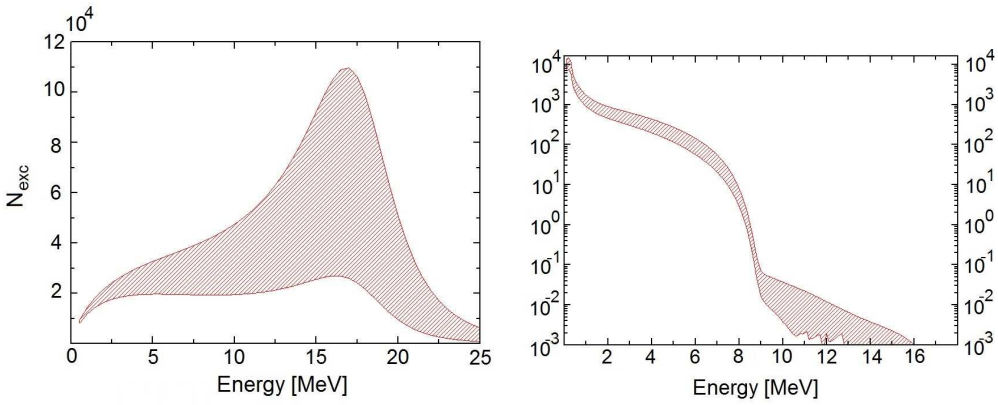

Figure 5.13: Left panel: the excitation spetrum obtained considering a lorentzian shape GDR with RIPL-3 parameters [87]. Right panel: the GDR γ decay obtained with GEMINI++ after the folding with the response function.

The left panel of Fig. 5.14 shows a comparison between the experimental spectrum and the tail of the GDR γ yield, while right panel shows the subracted spectrum. It is possible to see that an unresolved structure is present between 5 MeV and the one particle threshold energy.

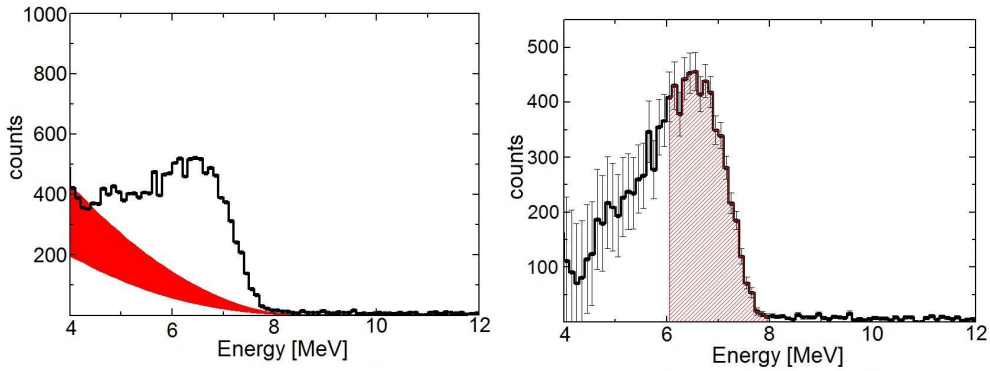

Figure 5.14: Left panel: the comparison between the GDR γ-yield (red band) and the experimental spectrum. Right panel: the subtracted experimental spectrum.

The multipolarity of this high energy γ transitions was investigated using both $LaBr_3$:Ce detectors and DALI2 array. The ratio between the statistics collected for the 2^+ level decay and this high energy yield was evaluated at different angles and compared with the one expected using the DWEIKO code as in the Iron case [93]. Here, thanks to the higher statistics, the emission at different angles was evaluated and it is of E1 nature.
The fig. 5.15 shows this comparison: the experimental points reproduce quite well the expected trend.

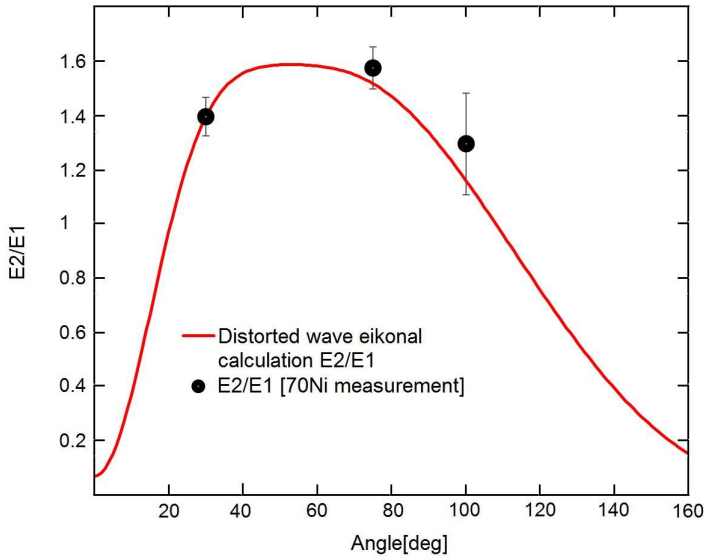

Figure 5.15: Comparison between the expected trend of the E2/E1 ratio (red line) and the ratio between the statistics from 2^+ level decay and the high energy γ-ray transitions (filled points).

5.6 Final results

The B(E1) values related to the transitions in the energy range of 6-8 MeV were deduced using the ^{62,64}Fe spectra shown in Fig.5.10 and the ^{70}Ni spectrum shown in fig.5.14.
The strength was deduced exploiting relation 5.7:

$$\sigma_{E1} = \frac{32\pi^2}{9}\frac{Z_T^2\alpha}{\hbar c}B(E1)\left(\frac{c}{v}\right)^2\left[\xi K_0K_1 - \frac{v^2\xi^2}{2c^2}\left(K_1^2 - K_0^2\right)^2\right] \tag{5.7}$$

where K are modified bessel functions of the parameter $\xi = \frac{\omega_{fi}b}{\gamma v}$, $E = \hbar\omega_{fi}$ is the excitation energy and b is the minimum distance, corresponding at minimum impact parameter at relativistic energies.
The converted B(E1) spectra, obtained using the scaling factors discussed in previous sections and the 5.7 relation, are shown in Fig. 5.16 5.17 in the energy range 6 - 8 MeV.
We considered the summed B(E1) values in the range of 6-8 MeV for all the three nuclei

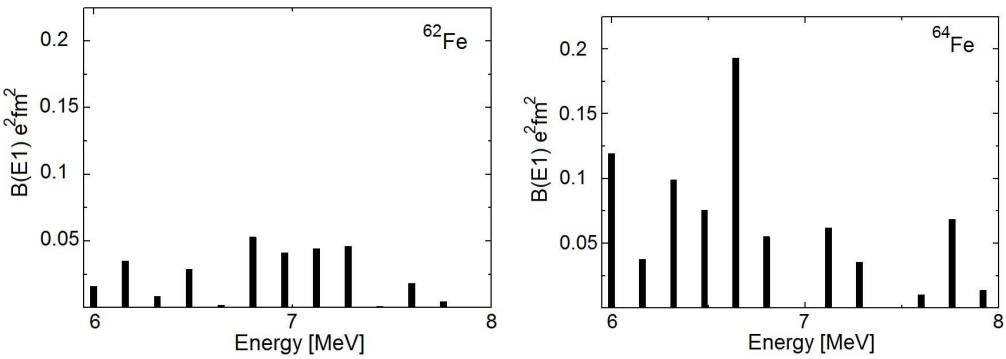

Figure 5.16: Left panel: B(E1) value spectrum in the range 6-8 MeV for ^{62}Fe. Right Panel: B(E1) value spectrum in the range 6-8 MeV for ^{64}Fe

and compared them with the same values already measured for other nuclei (as shown in fig. 5.18). The summed B(E1) values we obtained are here reported:
B_{6-8MeV}(E1)=0.3 $\pm$ 0.1 e^{2}fm^2 for ^{62}Fe
B_{6-8MeV}(E1)=0.77 $\pm$ 0.27 e^{2}fm^2 for ^{64}Fe
B_{6-8MeV}(E1)=1.05 $\pm$ 0.28 e^{2}fm^2 for ^{70}Ni
The plot in Fig. 5.18 shows that the values measured in this thesis are in the same range of the other nuclei already measured and reported in literature [28]. In addition the trend of the summed B(E1) as the N/Z ratio increases is confirmed, for the first time in literature, also in the case of exotic unstable nuclei.
In addition the Iron values were compared with the experimental results published

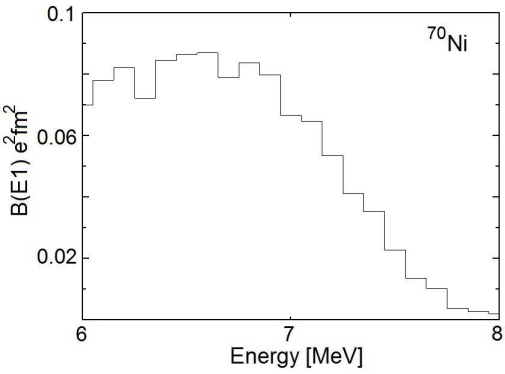

Figure 5.17: B(E1) value spectrum in the range 6-8 MeV for ^{70}Ni

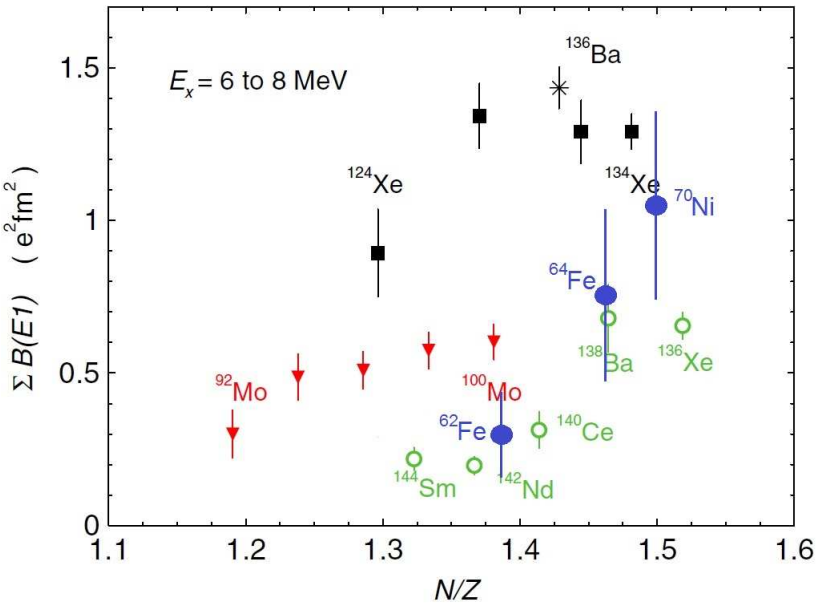

Figure 5.18: Summed B(E1) values in the range 6-8 MeV for nuclei already investigated in literature [28] and the results here obtained

in [92] for stable Iron (^{56}Fe). In this paper the total B(E1) in the energy region around the one particle separation energy was investigated. Here a B(E1) value integrated on the range 5-10 MeV was reported. The upper limit of this E1 strength amounted at 0.127 e^2fm^2. This value seems to indicate that the increase of the neutron number in Iron nuclei induces an enhancement of the dipole strength around the one particle separation energy.

As regarding the Nickel value, the error bar is quite large in spite of the high statistics.

This is not only due to the experimental uncertainties but also to the nuclear interaction contribution that may account up to 20% of the yield [96]. Even if the isoscalar excitation is not predominant, it should be taken into account: as a consequence there are large error bars.

The E1 response of the isotopes, here investigated, was also compared with the total E1 strength.The relation 5.8 explained in [7], was used to evaluate the total isovector electric dipole EWSR.

$$\Sigma_n(E_n - E_0)B(E1, 0 \rightarrow n) = 14.8\frac{NZ}{A}e^2fm^2MeV \tag{5.8}$$

Using the result of this relation, the percentage of the ESWR satisfied by the states here discussed was evaluated. Here the results are listed:

^{62}Fe : 0.9% $\pm$ 0.3 %

^{64}Fe : 2.3% $\pm$ 0.78 %

^{70}Ni : 2.7% $\pm$ 0.73 %

Though the error bars are quite large, due to the low statistics collected in two short beam time, the percentage of the EWSR related to these states is not negligible and the trend is clearly visible.

Conclusions and outlook

In this work the E1 response of ^{62,64}Fe and ^{70}Ni around the one particle separation energy was investigated. Coulomb excitation at relativistic beam energy was exploited to access the E1 strength in these neutron rich exotic nuclei. As introduced in this thesis, the E1 response of nuclei around one particle separation energy attracted a lot of interest due to its relation with nuclear structure and astrophysics aspects. The accumulations of E1 strength in this energy region are commonly called Pygmy Dipole Resonance, in comparison with Giant Dipole Resonance that exhausts the major part of the isovector dipole EWSR [7]. Theoretical interpretation of this nuclear feature is still under debate, but it was shown in literature that its strength is connected with the simmetry energy term of nuclear Equation of State and the neutron skin thickness [2]. In addition it was shown that this strength is relevant also for astrophysical aspects like neutron star structure and neutron capture reactions rate in exotic environment like supernovae [3].
In spite of the large amount of data available for stable nuclei, data about exotic nuclei are still scarce. The relativistic coulomb excitation technique applied for the measurements here discussed, and explained in detail in this PhD thesis, allows together with powerfull accellerators and modern detector systems to investigate also nuclei far from the valley of stability. The subject of this work is the investigation of E1 strength in neutron rich exotic nuclei using the state of the art detector arrays (AGATA,HECTOR$^+$ and DALI2). In fact thanks to the connection of these structures with the neutron number and in particular with the neutrons in outern shells, an enhancement of this feature is expected for very neutron rich nuclei.
The experiments here discussed were performed in GSI and Riken laboratory. ^{62,64}Fe

were investigated during the PreSPEC-AGATA campaign in GSI, the experiment started in the 2012 and it was concluded in the 2014; as regarding ^{70}Ni, it was measured in Riken during the DALI2 campaign in the autumn 2014. In both cases the radioactive beams were brought to collide with high Z value thick target to induce Coulomb excitation. The setup allowed to identify incident ions, the products of the reaction, to select the coulomb excitation reaction channel and to measure the γ decay of the de-excitation of the PDR in coincidence with the identified ion of the beam.

The γ-ray energy spectra showed an amount of statistics above the tail of Giant Dipole Resonance around the one particle separation energy. As the measured transitions are below the one particle separation energy, the good energy resolution of AGATA array could be exploited.

The increase of statistics was evaluated in the energy range 6-8 MeV for all the three isotopes. Fig. 5.19 and 5.20 show the final measured spectra.

We considered the summed B(E1) values in the range of 6-8 MeV for all the three nu-

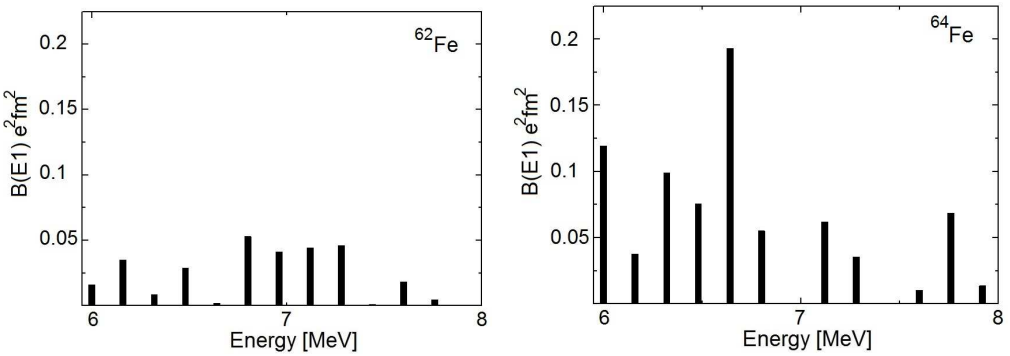

Figure 5.19: Left panel: B(E1) value spectrum in the range 6-8 MeV for ^{62}Fe. Right Panel: B(E1) value spectrum in the range 6-8 MeV for ^{64}Fe

clei and compared them with the same values already measured [28] for other nuclei (as shown in fig. 5.21).

B_{6-8MeV}(E1)=0.77 $\pm$ 0.27 e^{2}fm^2 for ^{64}Fe

B_{6-8MeV}(E1)=0.3 $\pm$ 0.1 e^{2}fm^2 for ^{62}Fe

B_{6-8MeV}(E1)=1 $\pm$ 0.23 e^{2}fm^2 for ^{70}Ni

It is important to underline that the value here obtained are in the same range of the ones already published. In addition, these results confirm the increase of the B(E1) strength with the N/Z ratio, observed for the stable nuclei. This trend is particularly evident in the Iron isotopes: the two neutrons in ^{64}Fe seems to be responsable of a strong increasing

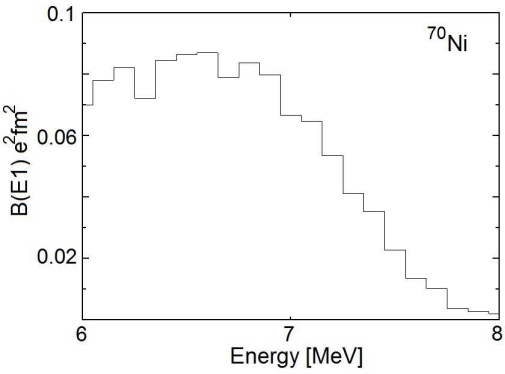

Figure 5.20: B(E1) value spectrum in the range 6-8 MeV for ^{70}Ni

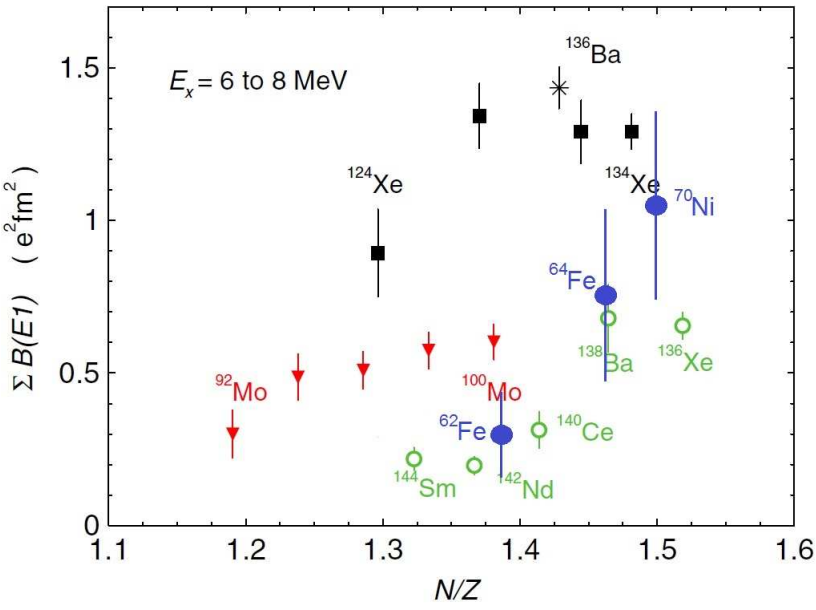

Figure 5.21: Summed B(E1) values in the range 6-8 MeV for nuclei already investigated in literature [28] and the results here obtained

of the dipole strength. This confirmation is very important because, for the first time in literature, it was verified in exotic nuclei far from the stability.

These results, in particular the ones about Iron isotopes, will be soon submitted for publication. The data about ^{70}Ni will be further analyzed also to investigate the strength above the neutron threshold. The coming upgrades of the experimental facilities will allow to produce exotic nuclei with higher and higher intensity and therefore explore more extreme neutron rich nuclei. The informations about the isovector character of

these states in the pygmy region, published in this thesis and the ones that will be provided in the next publications on the basis of this and a further anlysis, will provide indications and references to new experiments for a more detailed investigation of this structures and also in more exotic nuclei.

APPENDIX A

Statistical decay in the GEMINI++ code

In this Appendix, the GEMINI++ code will be discussed. The code was used in the data analysis to have an evaluation of the γ yield of GDR decay. GEMINI++ is a statistical-model code written to predict complex fragment emission in fusion reactions. In particular, for a given excitation energy of the Compound Nucleus, the code follows the decay using a Monte Carlo approach. This code is useful to have an estimation of the γ yield from statistical decay; in addition it can be exploited to investigate how this yield change as the varying of the gates on reaction products.

A.1 The code

GEMINI++ is a C++ code developed to investigate fusion-evaporation reactions. It was written and developed by R. Charity [86], while GDR γ decay was implemented by M. Ciemala [85]. The Hauser-Feshbach theory is the thoretical basis of the code. It is exploited to estimate fusion reaction cross sections and also to evaluate the particle emission in the evaporation stage. The code can be used to simulate a fusion evaporation reaction or just to investigate the statistical decay of an excitated compound nucleus. In this appendix the latter way of using the code is discussed because it was applied in the data analysis here presented. The decay of the Compound Nucleus is treated with a Monte Carlo routine. The input required by the code consists in the excitation energy, the spin and the diffusness parameter. The decay is processed as a series of sequential binary decay. This iterative routine stops when the energy still avaible is too low to continue the decay cascade or the competitive γ decay prevails. The code considers only E1, E2, M1 and M2 γ decay. As regarding dipole transitions, the Giant Dipole Resonance is already implemented in the code.

A.2 The statistical model

As already said in the previous section, GEMINI++ is based on the Hauser-Feshbach theory. According to this formalism, the partial decay width of a Compound Nucleus with a spin J_{CN} and excitation energy E*, for the evaporation of a particle *i* is equal to:

$$\Gamma_i(E*, J_{CN}) = \frac{1}{2\pi\rho_{CN}(E*, J_{CN})} \int d\epsilon \sum_{J_d=0}^{\infty} \sum_{J=|J_{CN}-J_d|}^{J_{CN}+J_d} \times \sum_{l=|J-S_i|}^{J+S_i} T_l(\epsilon)\rho_d(E* - B_i - \epsilon, J_d) \tag{A.2.1}$$

where T is the particle trasmission coefficient, ρ is the level density, while B and ϵ are particle binding energy and its kinetic energy. The evaporation channels here included are: n,p,d,t,^{3}He,α,^{6}He, $^{6-8}$Li fragments. The γ decay is treated separately. In this calculation [98] the separation energy, nuclear masses and shell corrections are obtained from the tabulations of Moller et al. [99]. Concerning transmission coefficients, the evaporation formalism is based on the condition of the detailed balance: this means that the barrier penetration is expected to be the same of the inverse reaction (absorption process). The real optical-model potentials are used here [98], with the incoming-wave boundary-condition model (IWBC), to calculate transmission coefficients. The compound nucleus thermal shape fluctuations and the fluctuations in the diffusness of the nuclear surface originate a distribution of the Coulomb barriers. For this reason GEMINI [98] considers an average of the transmission coefficients evaluated varying the radius for the nuclear potential around the value obtained from the global optical-model fits.

A.2.1 The level density

The level density used in the code is obtained by the Fermi Gas formula, including several corrections. It can be written as:

$$\rho(E*) = K_{coll}(E*)\rho_{FG}(E*) \tag{A.2.2}$$

where $K_{coll}(E*)$ is a factor that include the enhancement of the level density above the single particle value, this is caused by the rise of rotational and vibrational bands due to collective motions. The $\rho_{FG}(E*)$ is the Fermi Gas formula.

$$\rho_{FG}(E*, J) = \frac{(2J+1)}{24\sqrt{2}a^{1/4}U^{5/4}\sigma^3} exp(S) \tag{A.2.3}$$

where $S = 2\sqrt{aU}$, a is the level density parameter (obtained from single particle level density), U is the internal energy while $\sigma^2 = I_{rig}T$ with I_{rig} the moment of inertia and

T nuclear temperature. The a parameter is affected by shell effects; this was treated by Ignatyuk et al. [100], and it was included in the parameter as follows:

$$a(U) = \widetilde{a}(U)\left[1 + h(U)\frac{\delta W}{U}\right] \tag{A.2.4}$$

where $h(U) = 1 - exp(\eta_1 U)$ with $1/\eta_1$ = 18.5 MeV. The $\widetilde{a}(U)$ has dependances from internal energy and mass of the nucleus, GEMINI uses the following relation to take into account these dependances:

$$\widetilde{a}(U) = \frac{A}{k_\infty - (k_\infty - k_0)exp\left(-\frac{\mathbf{k}}{k_\infty - k_0}\frac{U}{A}\right)} \tag{A.2.5}$$

where $\mathbf{k}$ is a function of mass: $\mathbf{k}(A) = 0.00517exp(0.0345A)$. k_0 and k_∞ are parameters setted as $k_0 = 7.3$ and $k_\infty = 12MeV$. In this way for U=0 the dependence of $\widetilde{a}$ by the nuclear mass is A/7.3, reproducing the fit of the experimental data as shown in fig. A.1.

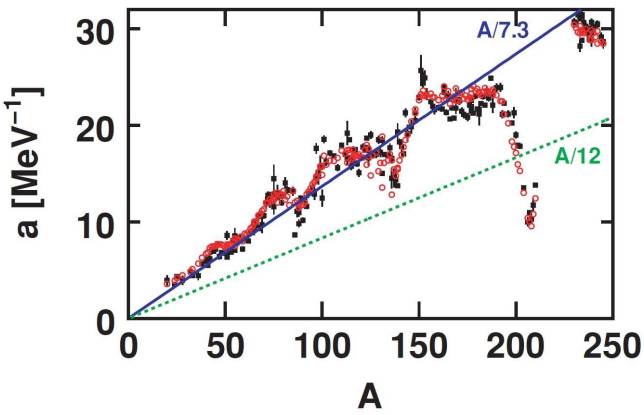

Figure A.1: Mass dependance of level density parameter at temperature T=0. The filled points are experimental results from neutron resonance measurements, the empty points are results from calculations using Ignatyuk approach

A.2.2 The γ decay

GEMINI evaluates the γ decay probability using the standard definition of multipole decay width (Blatt and Weisskopf 1958):

$$\Gamma_\gamma)(E_\gamma) = \frac{\rho_2}{\rho_1}\sum_l \xi_l f_l(E_\gamma)dE_\gamma \tag{A.2.6}$$

with $f_l(E_\gamma) = E_\gamma^{(2l+1)}$ and ξ_l is the strength function. As regards the Giant Dipole Resonance, it is implemented by using a lorentzian type resonance shape. In particular three lorentzian compenents can be treated by the code. It is defined by the relation:

$$\sigma = 2.09 \times 10^{-5} \frac{Z(A-Z)}{A} \sum_{k=1}^{3} \frac{S_k E_\gamma^2 \Gamma_{GDR,k}}{\left(E_\gamma^2 - E_{GDR,k}^2\right)^2 + E_\gamma^2 \Gamma_{GDR,k}^2} \tag{A.2.7}$$

where $E_{GDR,k}$ are GDR component energies, $\Gamma_{GDR,k}$ the corresponding widths and S_k the intensities. The GDR decay width is then defined as:

$$\Gamma_\gamma^{E1} = \sigma E_\gamma^2 \frac{\rho(E* - E_\gamma)}{\rho(E*)} \tag{A.2.8}$$

where ρ is the level density evaluated after and before the γ emission. The parameters of GDR can be inserted as input or they can be computed by the code using the systematics and refined with χ^2 minimization. Also M1 and M2 $gamma$ decay are considered in the code. The decay width is obtained by:

$$\Gamma_\gamma^{Ml} = W_{ul} F_t D_0 A^{2(l-1)/3} E_\gamma^{2(l+1)} \frac{\rho(E* - E_\gamma)}{\rho(E*)} \tag{A.2.9}$$

where W_{u1} = 2.1$\times 10^{-8}$ and W_{u2}= 1.5$\times 10^{-14}$, D_0 = 1 MeV and F_t is a correction factor for the Weisskopf formula.

APPENDIX B

The setup simulation code

In this appendix the AGATA simulation code is presented [40]. It was used in the data analysis to build the Response Function. It is a Monte Carlo code developed in C++ programming language: it is diveded in several steps to simulate the reaction of the experiment, the background, the γ detection and reconstruction. It was developed and tuned for PreSPEC setup in GSI loboratory.
In addition the HECTOR-DALI simulation code is presented. The core of the code is the same of the one used for AGATA and developed for Riken setup.

B.1 The AGATA code structure

The AGATA simulation program is a C++ object oriented code. It accepts as input the parameters of the beam, the target and the γ decay scheme of the excited nuclei.
The geometry of AGATA array has to be implemented through configuration files.
The code simulates the reactions in the target, the background and the γ interaction mechanism. The simulations are performed with the Monte Carlo approach. The code uses GEANT4 libraries for the radiation-matter interaction. The results are organized in ROOT files.
The simulation is divided in three steps: the Event-Generator, where the reactions that emit γs are computed; the Event-Builder, where the γ detection of the experimental setup is simulated; the Event-Reconstructor, where the analysis and γ-ray tracking are performed.
This structure is the same of the simulator code for the DALI setup in RIKEN. The codes are very similar and both of them were used during the data analysis: one for GSI experiments, one for RIKEN measurement.

B.1.1 Event Generator

The event generator is the first step of the simulation. Here the interaction between the beam and the projectile is considered. The input parameter files require information on:

- BEAM: the mass, the charge, the kinetik energy of projectiles are required. In addition also the beam spot position on the target, the width and the angle between the beam direction and the target are needed.

- TARGET: the mass, the charge and the thickness of the target are needed. In addition a table of the loss of energy per unit of length at kinetik energy varying is required. This table has to be specific for the beam-target coupling.

- γ DECAY-SCHEME: the γ decay scheme with the energy of the levels and the probability of the transitions has to be inserted as input. These informations about the nuclues of interest are listed in a separate parameter file.

The event generation step define also the total number of events that will be simulated. In addition the atomic backround is computed at this stage.

B.1.2 Event Builder

The Event Builder stage consists essentially in the old AGATA simulation code developed by E. Farnea et al. for the AGATA campaign in Legnaro INFN laboratory [38].
The geometry of the AGATA clusters are implemented (both the triple and the double clusters) [40]. The code require also the geometry of the target and the frame.
Monte Carlo routines are used to simulate energy release of γ-s and every interaction point is characterized by a position, the amount of energy released, the timing information, the detector and the segment in which it occurs.
The interaction mechanisms here considered are: Compton scattering, photoelectric absorption, pair production, Rayleigh scattering.

B.1.3 Event Reconstructor

The last step of the simulation is the reconstruction of the events. Here the doppler correction is performed on the basis of the informations coming from the previous steps. In addition also γ filters can be applied: the MGT-γ ray tracking can be performed, or also other γ-ray tracking algorithms.

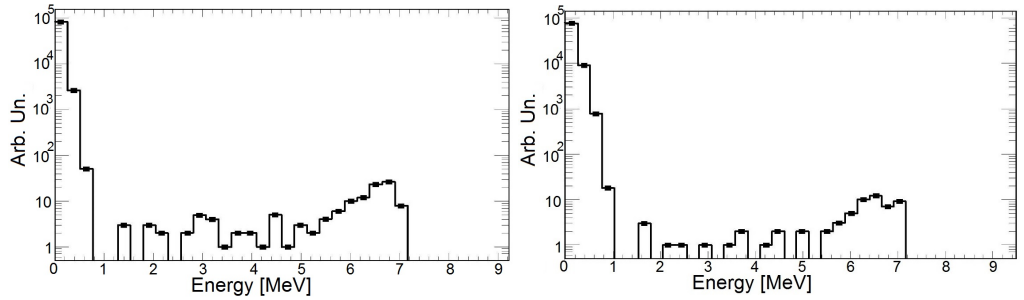

Figure B.1: Left panel: AGATA simulated spectrum a 7 MeV γ ray emitted by a source in flight moving with the same β of the experiment. Right panel: AGATA simulated spectrum a 7 MeV γ ray emitted by a source at rest.

B.2 Simulations for ^{64,62}Fe experiment

The AGATA simulation code was used to obtain the Response Function of AGATA array for the measurement. In particular the response function for both the in-flight and target emission was computed. All the energy range from 0.5 to 18 MeV was scanned. The efficiency obtained with the simulation was compared with both the one obtained from the ^{60}Co calibration run before the production runs and the one tabulated in technical reports [75]. This was an important tuning to make the simulated setup as much as possible similar to the laboratory setup. In addition it was verified that the simulated efficiency, as a function of the energy, follows the expected exponential trend.
In fig. B.1 a comparison for the spectrum obtained considering a γ-ray at 7 MeV of energy emitted in-flight and at rest is shown. The spectrum obtained for the emission at rest is characterized by an higher energy resolution, due to the absence of the doppler broadening. On the other hand the doppler boost enhance the absolute efficiency of the apparatus in the case of the in-flight emission.

The response function was used to evaluate the influence of the γ yield from GDR decay in the AGATA spectra. In Fig. B.2 an example of the transformation applied by the Response Function is shown. In addition the AGATA simulations were used to evaluate the efficiency in the energy range investigated in this thesis.

B.3 The HECTOR-DALI code

The simulation code developed for AGATA was adapted for the Riken setup by P. Doornenbal et al. [101]. The structure of the three steps: Event Generator, Event Builder and

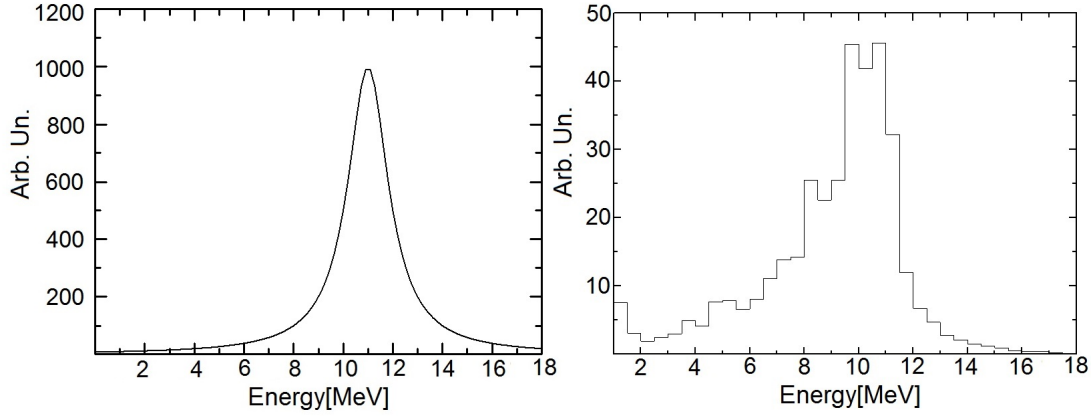

Figure B.2: Left panel: a lorentzian shape peak at 11 MeV, used as input of the AGATA Response Function. Right panel; energy spectrum output of the Response Function

Event Reconstructor was maintained. The code allowed to simulate both DALI, already implemented, and HECTOR setup, implemented for the 2014 campaign. The code, as in the case of AGATA, was used to compute the response function for the two apparata. The efficiency from the response function for the $LaBr_3$:Ce detectors was compared with [58] to check that the code provide a good estimation of the efficiency. In fig. B.3 the efficiency of the HECTOR array for γs emitted in flight is plotted as function of the energy.

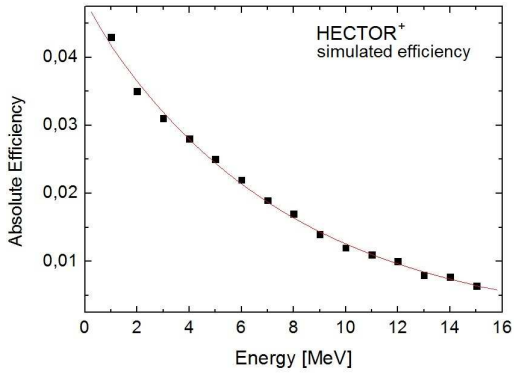

Figure B.3: Simulated absolute detection efficiency for γs emitted in-flight. It was obtained with the HECTOR response function in Riken (an interval of 1 MeV was considered).

APPENDIX C

Femul and prespec data analysis codes

In this appendix a short description of the codes used for sorting the raw data collected in the experiments in GSI is presented.
The informations here reported are based on the tutorials and presentations at the data analysis workshops held by the developers of these codes. This is not a full explanation or a manual for the users of the codes. The aim is providing an overview of the logic at the basis of the tools used for this complex data analysis.

C.1 Femul

Femul [102] is an emulator of the NARVAL system [70] used for the AGATA data handling. It was born with the aim of helping the debugging of NARVAL system but it is now one of the most used approach to sort AGATA data offline. It can be considered a full emulation of the NARVAL framework with the exception that it is a simple process running on a specific server, while NARVAL involves more computers.
As introduced in chapter 3 the algorithm follows a rigid data-flow where every step is called ”actor”. The configuration for the crystals and the data flow is defined in the so-called ”topology” files. Every actor has specific configuration files.
The data flow can be divided in two parts: a local process, where the data of every detector are separately processed and a global process where the data from every crystal are merged between them and with the ancillary detectors, in the end the tracking algorithms are applied.
In this data analysis, only the local part of the data flow was processed: the merging of the data and the event bulinding were performed using the prespc code. The tracking algorithm was tuned to have the best performances, for this reason it was necessary to

change the settings of this library respect to the one provided by the prespec package.
The AGATA raw data are written in separated files for every crystal. For this reason from the very beginning the first part of the Femul data flow runs the data from every detector in an indipendent way from the others.
The first actor is the *Crystal Producer*: it reads the data and prepares them in a frame to be processed by the next actors. In particular it acts as a local event builder: the data from every mezzanine is organized as a part of the data from the same crystal.
The next actor is the *Preprocessing Filter*: it applies calibrations and a first filtering of the signal. Cross talk corrections are applied at this stage, in addition the net-charge segments are identified.
The most significant actor in this local process is the *PSA Filter*: it applies a GRID search algorithm to extract the position of the interaction in the segments. The algorithm is a simple comparison between the digitized and recorded signal and a set of signal samples called AGATA signal basis. This set of samples is obtained by accurate measurements and calculations of the electric field in the detector. The algorithm simply compares the samples with the signal recorded and chooses the one that best fit the data. In Fig. C.1 an example of a superposition of the signal measured and the sample chosen by the algorthm is shown. The selection of the samples allows to obtain the position of the interactions. In fact every samp,e is associated to a specific γ interaction position.
A last actor was inserted at the beginning of the GSI experimental campaign of AGATA: the *Post-PSA Filter*. It applies neutron damage corrections and further calibrations that re-correct the one applied at preprocessing level. In this analysis this step was not considered because the prespec code requires AGATA data as output of PSA filter.
The AGATA data are written in ADF files (AGATA Data Format) and they can be used as input of other analysis codes like prespec or Go4 [104].
The global part of the data-flow is composed by *Event Builder - Event Merger* actors and the tracking filter. In this part of the data flow the data from different crystals are used to build an "event" considering the timestamp, the same logic is used by the *Event Merger* to build the global event using the AGATA event and the data from ancillary detectors.
The last actor is the *Tracking Filter*: it applies tracking algorithm using MGT libraries. This class of procedures applies the γ-ray tracking selections on the basis of the considerations explained in chapter 3. The code clusterizes the γ interactions, provided by PSA, and it finds the best combination of them minimizing the χ^2. It is an important aspect choosing the threshold of acceptance of this figure of merit on the basis of the background level that affected the measurement.

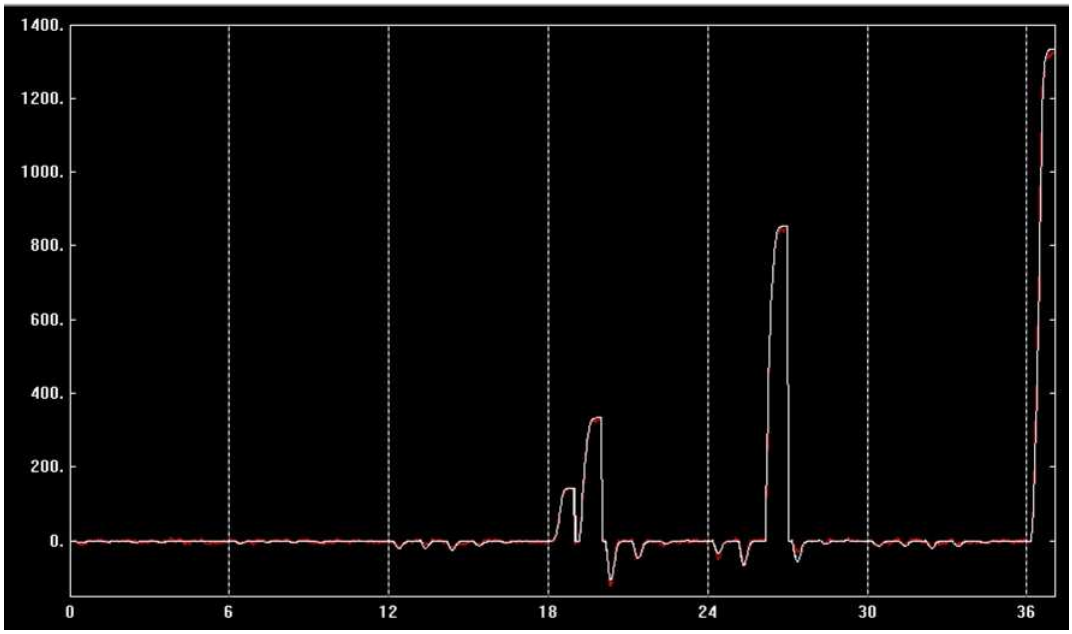

Figure C.1: Superposition of the signal recorded (red line) and the sample chosen by the algorithm (white line). The last signal is from the central core contact.

In spite of previous actors, the output of this last one is a ROOT file where all the informations extracted by the raw data are organized in a Tree.

C.2 prespec

The prespec code [103] was developed for the online-acquisition and the data analysis for the AGATA experimental campaign in GSI with the PreSPEC setup. It is a C++ code that can be considered an upgrade of the previous version of the offline Go4 data analysis code. It was released in 2014 for the last part of the experimental campaign. In this first release the data of AGATA and MBS are merged and processed.
The code accepts data merged online in lmd format, where lmd is the List Mode Data format in which MBS data are usually recorded. Another working available mode accepts as input the AGATA data from PSA Filter and the lmd files from MBS.
Prespec code, like Femul, merges the data from the two systems: NARVAL and MBS. On the basis of the timestamp the coincidence is checked and the merging performed: for this reason a particular care is required that the input file are in the correct time-order, otherwise the coincidence could be lost and the events are not built.

After the merging, the analysis can start.
The first step of the data flow is performed by the so-called ”crates”. Every detector system has its own crates that call the correct unpackers for reading and preparing the data for the next analysis stage. In the code the every unpacker is identified as a particular ”module” of a defined ”crate”.
The next step of the analysis is performed the ”processors”. Every processor calls as input the data from the unpacker or from another processor. The processors apply calibrations and filters on the data. Every detector system has a set of processor.
This overview of the prespec code shows that also in this case, as in Femul, the data flow is quite rigid: the direction of the processing cannot follow loops or conditional calls of the processors.
The data analysis code is built in a way that it keeps all the libraries with the codes in a folder. The user can organize the data analysis of the raw data defining for every detector apparatus a set of configuration files that provides: calibration parameters, gates for filtering, the set and the order of the procedures to call to unpack, calibrate and filter the data.
The output of this code is a ROOT file where the processed data are organized in a Tree. The user can choose how to build this tree selecting the processors of the detector systems of interest.

Bibliography

[1] A. Klimkiewicz, et al., Phys. Rev. C76, 051603 (2007).

[2] A. Carbone et al., Phys. Rev. C **81**, 041301 (2010).

[3] J. Piekarewicz, JOP: Conf. Series **420**, 012143 (2013).

[4] N. Pietralla et al. EPJ Web of Conferences **66**,02083 (2014).

[5] S. Takeuchi et al. Nucl. Instrum. and Meth. in Phys. Res. A **763**,596-603(2014).

[6] O. Wieland et. al. Phis. Rev. Lett.**102** (2009) 092502.

[7] M. N. Harakeh and A. van der Woude, Giant Resonances (2001) Oxford Science Publications.

[8] A. Zigles et al., JOP: Conf. Series **580**(2015)012052.

[9] D. Savran et al., Progr. Part., Nucl., Phys. **70**(2013) 210-45.

[10] G.A. Bartholomew, Annu. Rev. Nucl. Sci. **11**(1961) 259.

[11] R.Mohan, M. Danos, L.C. Biedenharn, Phys. Rev. C **3** (1971) 1740.

[12] D. Gambacurta et al., Phys. Rev. C **84**, 034301 (2011).

[13] T. Tsoneva & H. Lenske, Phys. Rev. C **77**, 024321 (2008).

[14] T. Hartmann et al., Phys. Rev. Lett. **93**, 192501 (2004).

[15] V.Baran et al., Phys. Rev. C **85**, 051601 (2012).

[16] J. Liang at al., Phys. Rev. C **75**, 054320 (2007).

[17] E. Litvinova et al., Phys. Rev. C **78**, 014312 (2008).

[18] S. Pascu et al., Phys. Rev. C **85**, 064315 (2012).

[19] N. Paar et al., Phys. Rev. C **67**, 034312 (2003).

[20] E. Litvinova et al., Phys. Rev. C **79**, 054312 (2009).

[21] E. Litvinova Private Communication plotted in D. Savran et al., Progr. Part., Nucl., Phys. **70**(2013) 210-45.

[22] J. Piekarewicz, Phys. Rev. C **73**, 044325 (2006).

[23] S. Goriely, Phys. Lett. B **436** (1998) 10-18.

[24] N. Tsoneva et al., Phys. Rev. C **91**,044318(2015).

[25] J. Piekarewicz et al., Phys. Rev. C **85**,041302(2012).

[26] B. L. Berman & S.C. Fultz, Rev. Mod. Phys. **47**(1975) 713.

[27] P. Adrich et al., Phis. Rev. Lett. **95** (2005) 132501.

[28] R. Massarczyk et al. Phis. Rev. Lett. **112** (2014) 072501.

[29] D. M. Rossi et al. Phis. Rev. Lett.**111** (2013) 242503.

[30] E. Litvinova, P. Ring, V. Tselyaev, Rhys. Rev. C.**88** (2013) 044320.

[31] F.C.L. Crespi et al. Phys. Rev. Lett **113** (2014) 012501.

[32] V.O. Nesterenko et al. EPJ Web of Conferences **93** (2015) 01020.

[33] Carlos Bertulani CNS-EFES Summer School 2009.

[34] K. Alder and A. Winther, "Electromagnetic Excitation" (Amsterdam: North Holland) 1975.

[35] T. Glasmacher, Nucl. Phys. A 693, textbf90 (2001).

[36] J. D. Jackson "Classical Electrodinamics" (New York: Wiley), 1975.

[37] C. Bertulani, A. Bawens, Nucl, Phys, A **442**(1985) 739-752.

[38] E. Farnea et al. Nucl. Instrum. and Meth. in Phys. Res. A **621**,331(2010).

[39] L. Pellegri On the nature of Pygmy Dipole Resonance in ^{124}Sn via inelastic scattering of 17O,PhD thesis, University of Milan(2014).

[40] Simulations for the campaign of AGATA at GSI, AGATA Mechanics Working Group Meeting(2009).

[41] F. Recchia et al. Nucl. Instrum. and Meth. in Phys. Res. A **604**,555(2009).

[42] A. Olariu et al. NIn IEEE Transactions on Nuclear Science, 53, 1028-1031 (2006).

[43] T. Kröll & D. Bazzacco Nucl. Instrum. and Meth. in Phys. Res. A **565**,691(2006).

[44] F.C.L. Crespi et al. et al. Nucl. Instrum. and Meth. in Phys. Res. A **570**,459(2007).

[45] T. Kröll & D. Bazzacco Nucl. Instrum. and Meth. in Phys. Res. A **463**,227(2001).

[46] J. van der Marel & B. Cederwall Nucl. Instrum. and Meth. in Phys. Res. A **437**,538(1999).

[47] G.J. Schmid et al. Nucl. Instrum. and Meth. in Phys. Res. A **430**,69(1999).

[48] A. Lopez-Martens et al. Nucl. Instrum. and Meth. in Phys. Res. A **533**,454(2004).

[49] D. Bazzacco Nucl. Phys. A **746**,248(2004).

[50] F.C.L. Crespi et al. et al. Nucl. Instrum. and Meth. in Phys. Res. A **705**,47(2013).

[51] R. Avigo Caratterizzazione dei rivelatori HPGe segmentati con raggi gamma ad alta energia,Master thesis, University of Milan(2011).

[52] Y.Sato Overview and developments on BigRIPS detectors, BigRIPS Analysis Workshop (2014).

[53] H.Wang Total kinetic energy detector, BigRIPS Analysis Workshop (2014).

[54] T. Nishio RIKEN Accel. Prog. Rep. **29** (1996) .

[55] T. Kubo et al. Prog. Theor. Exp. Phys. **2012**, 03C003.

[56] H. Baba et al. Nucl. Sci. Symp. Conf. Rec., 2008. NSS'08. IEEE (pages 1384 - 1386).

[57] D. Ralet et al. Nucl. Instrum. Meth. in Phys. Res. A **786** (2015) 32-39.

[58] A. Giaz et al. Nucl. Instrum. Meth. in Phys. Res. A **729** (2013) 910-921.

[59] P. Golubev et al. Nucl. Instrum. Meth. in Phys. Res. A **723** (2013) 55-66.

[60] H. Geissel et al. Nucl. Instrum. Meth. in Phys. Res. B **70** (1992) 286-297.

[61] F.Ameil et al. GSI SCIENTIFIC REPORT 2011.

[62] A. Wendt Ph.D. Thesis 2013 Koln.

[63] D. Rudolph et al., LYCCA-TDR V1.2 (2008)

[64] S. Akkoyun et al., Nucl. Instr. Methods A **668**, 26 (2012).

[65] A.I. Morales PhD thesis (2010).

[66] P. Boutachkov EGAN presentation(2012).

[67] TPC Technical Manual.

[68] R. Hoischen et al., Nucl. Instrum. and Meth. in Phys. Res. A **654** (2011) 354-360.

[69] N.Kurz, presentation EE, GSI, Zagreb.

[70] X. Grave et al. 14th IEEE-NPSS (2005).

[71] Saint Gobain, Performance Summary: BrilLanCe^{TM} Scintillators.

[72] O. B. Tarasov and D. Bazin, Nucl. Instrum. Meth. in Phys. Res. B **266** (2008) 4657-4664.

[73] C. Scheidengerger et al., Nucl. Instrum. Meth. in Phys. Res. B **142** (1998) 441-462.

[74] D. Ralet PhD thesis (2015) Darmstadt.

[75] N. Lalovic et al., Nucl. Instrum. Meth. in Phys. Res. A - In PRESS.

[76] Balraj Singh Nuclear Data Sheets 108, 197 (2007).

[77] A. L. Nichols, Balraj Singh, Jagdish K. Tuli Nuclear Data Sheets 113, 973 (2012).

[78] J.K. Tuli Nuclear Data Sheets 103, 389 (2004).

[79] C.A. Bertulani et al., Phys. Lett. B 650(2007)233-238.

[80] B. Pritychenko Nuclear Data Sheets 98, 798 (2012).

[81] W. Rother et al. Phys.Rev.Lett. 106, 022502 (2011).

[82] J.Ljungvall et al. Phys.Rev. C 81, 061301 (2010).

[83] H.J. Wollersheim ACTA PHYS. POL. B Vol. 42(2011).

[84] H.J. Wollersheim et al. Nucl. Instrum. Meth. in Phys. Res. A **537** (2005) 637-657.

[85] M. Ciemala et al. ACTA PHYS. POL. B Vol. 44(2013).

[86] R. J. Charity hys.Rev. C 82, 014610 (2010).

[87] R. Capote et al. Nuclear Data Sheets - 110, 12, 2009, 3107-3214.

[88] L.M. Young,Ph.D. Thesis, University of Illinois(1972), unpublished.

[89] B. L. Berman et al. Bull. Am. Phys. Soc. 31, 855(1986).

[90] L. Pellegri et al., Phys. Lett. B 738(2014) 519-523.

[91] L. Pellegri et al., Phys. Rev. C **92**, 014330 (2015).

[92] F. Bauwens et al., Phys. Rev. C **62**, 024302 (2000).

[93] people.nscl.msu.edu/ brown/reaction-codes/bertulani/Dweiko.pdf.

[94] N. Nakatsuka, H. Baba private comunication.

[95] T. Marchi et al. EPJ Web Conf. **63**, 01021 (2013).

[96] K. Li et al., Phys. Rev. C **92**, 014608 (2015).

[97] Riken/RIBF Annual Report 2015.

[98] R. J. Charity INDC(NDS)-0530 Distr. SC (2008).

[99] R. Moller et al. Atomic Data Nucl. Data Tables **59**, 185 (1995).

[100] A. V. Ignatyuk et al., Yad. Fiz. **21** 485(1975).

[101] www.nishina.riken.jp/collaboration/SUNFLOWER/misc/download/simulation.html.

[102] D. Bazzacco Advance Gamma Tracking Array AGATA presentation at 2011 EGAN school, Liverpool.

[103] M. Reese Ancillary Software Development at GSI AGATA week 2013, GANIL.

[104] Adamczewski et al. Go4 v2 Analysis Framework Computing in High Energy and Nuclear Physics, 2003,La Jolla,California.

Acknowledgments